The Pennsylvania State University

The Graduate School

Department of Materials Science and Engineering

MICROSTRUCTURE-PROCESSING-PROPERTY RELATIONS

IN CHEMICAL SOLUTION DEPOSITED BARIUM TITANATE FILMS

A Thesis in

Materials Science and Engineering

by

Tanawadee Dechakupt

Submitted in Partial Fulfillment
of the Requirements
for the Degree of

Doctor of Philosophy

December 2007

The thesis of Tanawadee Dechakupt was reviewed and approved* by the following:

Susan Trolier-McKinstry
Professor of Ceramic Science and Engineering
Thesis Advisor
Chair of Committee

Clive A. Randall
Professor of Materials Science and Engineering

Venkatraman Gopalan
Associate Professor of Materials Science and Engineering

Amar Bhalla
Professor of Solid State Science and Electrical Engineering

James P. Runt
Professor of Polymer Science
Chair of Intercollege Graduate Degree Program in Materials Science and Engineering

*Signatures are on file in the Graduate School

ABSTRACT

This thesis explored the microstructure-processing-property relationships in chemical solution deposited $BaTiO_3$ films on Ni foils as model thin film capacitors. Different techniques, including X-ray diffraction, transmission electron microscopy and spectroscopic ellipsometry were combined to provide better understanding of microstructure and interface quality of $BaTiO_3$ thin films on Ni foil.

It was found that high quality thin films could be prepared using rapid thermal annealing 750^{o}C in N_2 to crystallize the film without building up significant levels of NiO on the substrate. After building up the desired dielectric thickness, the films were heat-treated at 1000^{o}C and later re-oxidized under controlled oxygen partial pressure conditions. The resulting films have dielectric constants of 1000-1300 which are stable as a function of temperature with loss tangents less than 2%.

Furnace annealed barium titanate films on Ni foil were characterized by X-ray diffraction and transmission electron microscopy (TEM). X-ray diffraction shows a well-crystallized polycrystalline perovskite phase in furnace annealed films with a high intensity of the 100 and 200 peaks. The films show equiaxed grains with average grain size of 42 nm. There are 5-6 grains across a 200 nm thick film, suggesting that it should be possible to use grain boundaries in films in order to control the capacitor reliability, as is done with bulk capacitors. NiO was detected by X-ray diffraction, but not by transmission electron microscopy, suggesting that the oxide is not a continuous barrier layer, but is distributed inhomogeneously over the surface. Electron energy loss microscopy shows the existence of C in barium titanate grains. In addition, high

resolution transmission electron microscopy and electron energy loss spectroscopy showed that an interfacial Ni-Ba alloy develops at the interface between the $BaTiO_3$ film and the Ni foil. This would be consistent with very reducing partial pressures locally during the processing, probably as a result of retained organics.

Decomposition of both powders dried from barium titanate solutions and barium titanate films was studied by differential scanning calorimetry (DSC), thermal gravimetric analysis (TGA), Fourier transform infrared spectroscopy (FTIR) and X-diffraction. It was found that flowing N_2 delays decomposition of organics in the powders, leading to retained carbonate phases. Thus, crystallization of barium titanate occurs via decomposition of a barium carbonate phase. Retained organics, especially C, in $BaTiO_3$ films was thus found to be critical in processing of dense chemical solution deposited films in low oxygen partial pressures.

The optical properties, film density and film thickness were studied by spectroscopic ellipsometry as a function of processing conditions. It was shown that the refractive index of amorphous dried films increases as drying temperature increases. Similarly, the refractive index of the films increases as the RTA temperature increases, probably at least in part due to crystallization of $BaTiO_3$ and removal of some of the intermediate phases. On annealing at 1000°C, there is slightly increase in the refractive index of the film due to further crystallization. The final refractive index is comparable to that of 95% dense barium titanate ceramics. Re-oxidation did not change the refractive index of the film.

To facilitate studies of the dielectric/electrode interface, the optical properties of thermally grown NiO on Ni foil were extracted. It was found that the Ni foil begins to

oxidize at 300^{o}C in air. The real part of the high frequency dielectric constant of NiO is similar to that of barium titanate, which complicated modeling of NiO in barium titanate films on Ni foil.

TABLE OF CONTENTS

LIST OF FIGURES

LIST OF TABLES

ACKNOWLEDGEMENTS

I would like to express my deep gratitude to Prof. Susan Trolier-McKinstry for her advice, understanding and support throughout the years. It has been a great opportunity to work under her supervision. I am also grateful to Prof. Clive Randall for his suggestions about this work and serving as my committee. I also thank the other committee members: Prof. Venkatraman Gopalan and Prof. Amar Bhallar for their helpful suggestions.

I also would like to acknowledge Royal Thai Government scholarships, Intel and Kemet for financial supports for my entire education at Penn State.

I would like to thank Gaiying Yang, David Lu and Song Won Ko for data of parts of this work. Also, thank you to Prof. Ian Reaney of Sheffield University and Xiaojun Weng for advice on TEM sample preparation. Thanks to Trevor Clark for FIB training.

It is my pleasure to meet and work with the bunch of nice and smart people in the STM group (past and present). Thanks to all of you for your help and suggestions. Special thanks go to Roni Levi, Hajime Nagata and Song Won Ko, who work on thin film capacitors for helpful discussion and comments for this work. I also thank to MRL staff members who provided help and suggestions when I needed them.

Lastly, I thank my families for their love and support. The “thanks” is extended to Chanin for his love and caring that helped me through the difficult times.

Chapter 1

Introduction

1.1 Base-metal electrode multilayer ceramic capacitors (BME MLCCs)

Multilayer ceramic capacitors (MLCCs) have been widely used in electronic circuits, including computers and cellular telephones, because of their small size and high volume efficiency. Basically, an MLCC consists of alternating layers of dielectrics and internal electrodes, as shown in **Fig. 1.1.** The total capacitance of a MLCC is the sum for all of the dielectric layers. Such a structure allows great flexibility in preparing a wide variety of capacitance values in a range of case sizes.

The drive to increase the capacitance obtainable in a given case size has driven two factors continuously: a decrease in the dielectric thickness, and an increase in the number of layers. As an example, **Fig. 1.2** shows the evolution of Kemet's commercial (0603) Class 2 MLCCs **[1]**. The dielectric thickness decreased from 6 μm (1997) to <1 μm (2007) over the last decade. In order to continue this trend in miniaturization, Randall et al. projected that MLCC would have 1900 layers of 0.17 μm thick dielectrics in 2010 **[1]**. These layer thicknesses are below what can currently achieved by tape casting of the dielectric, and so alternative means of preparing the capacitors are being considered.

The most commonly used dielectrics for MLCC are barium titanate-based ceramics **[2, 3]**. The composition and microstructure of the barium titanate are modified to meet EIA (Electronic Industries Association) specifications for the temperature

coefficient of capacitance **[2, 4]**. For example, the core-shell structure in X7R capacitors is produced by introduction of dopants and use of a controlled sintering profile. The result is a more uniform dielectric constant over a wider temperature range. Base metals, i.e. Ni and Cu have been used as internal electrodes in MLCCs, because of instability in the price of Pd (and Pd-Ag alloys) **[2]**. The use of base metal electrodes requires cofiring in highly reducing atmosphere to prevent oxidation of the electrodes. Oxygen vacancies

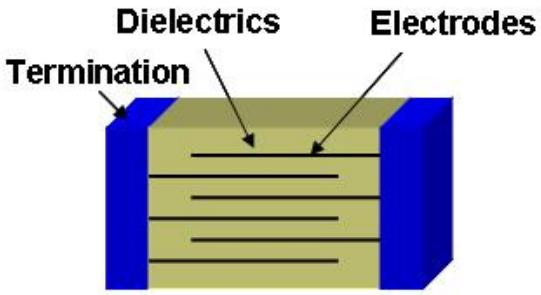

Fig. 1.1 Schematic of multilayer ceramic capacitor

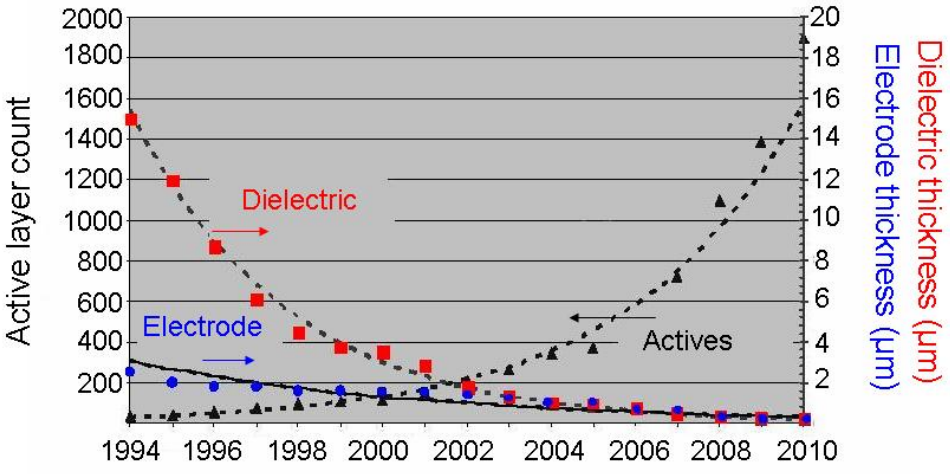

Fig. 1.2 Trend of dielectrics and electrode thickness and active layer count of Kemet's commercial (0603) Class 2 MLCCs **[1]**

introduced in the dielectric layers can be partially ameliorated by post-oxidation. In manufacturing of MLCCs, typical reducing atmospheres for cofiring and re-oxidation are 1300^{o}C in 10^{-10} atm pO_2 and 800^{o}C in 10^{-8} atm pO_2, respectively **[5, 6]**.

Despite re-oxidation, some oxygen vacancies which cause insulation resistance degradation **[7-11]** remain in the dielectrics. It was shown that the reliability of the capacitor significantly depends on the Schottky barriers at the electrode-dielectric interface and the grain boundaries that limits migration of the oxygen vacancies toward the cathode **[5, 6, 8]**. Addition of some rare-earth ions i.e. Y^{3+}, Dy^{3+} and Ho^{3+} was found to considerably improve the insulation resistance and lifetime of low pO_2 treated barium titanate **[12-16]**.

There have been some reports concentrating on the microstructure of the dielectric layer and the interface between the Ni electrode and the dielectric in MLCCs. Opitz et al. showed that in the re-oxidation step, oxygen diffusion along the Ni electrodes is faster than the direction perpendicular to it **[17]**. Oxygen vacancies in low pO_2 - processed barium titanate dielectrics resulted in the appearance of dislocation loops observable in a transmission electron microscope **[5, 18, 19]**. Later work showed that clustering of oxygen vacancies in some degraded barium titanate grains results in a modulated structure with {111}planar defects **[20, 21]**. Yang et al. **[5]** showed that the oxygen content in cofired barium titanate is not uniform, and that a higher oxygen vacancy concentration is observed near the Ni electrode. The local variation of barium titanate reduction was attributed to the effect of residual carbon. However, the uniformity of the oxygen content in barium titanate is significantly improved after the re-oxidation step. Yang et al. **[22]** also revealed the existence of a discrete layer (4-15 nm

thick) of Ni-Ti-Ba metallic alloy between the Ni and barium titanate in many commercial MLCCs. The alloy layer is formed during high temperature cofiring and is stable through the re-oxidation step. On the other hand, Chen et al. **[23]** reported interdiffusion of Ni into the dielectric layer. It was found that the thickness of the diffused layer increased as the dielectric thickness decreased.

MLCCs production has traditionally employed tape casting for the barium titanate and screen printing of the Ni electrodes. With progressive reduction in dielectric thickness, there have been major advances in optimization of the tape cast slurries and processes to obtain thinner green sheets. These include controlling solution dispersion, developing of nanopowders, etc. **[24-26]**.

Alternatively, thin film approaches to multilayer capacitors have also been explored recently. Sakabe et al. **[27]** demonstrated thin film multilayer capacitors prepared on Pt-coated MgO substrates by metalorganic chemical vapor deposition. With 12 layers of 0.26 μm thick $(Ba,Sr)TiO_3$ dielectrics, the capacitors show very promising capacitance per unit volume (33 $\mu F/mm^3$). Koutsaroff et al. **[28]** have fabricated double layer BST thin film capacitors with Pt electrodes on glazed alumina with a BST and TiO_x buffer layer by metal-organic decomposition. The capacitance density achived was 36.5 $fF/\mu m^2$. In addition, Nagata et al. have shown feasibility of making capacitors by microcontact printing **[29]** of thin films.

Development of thin film versions of MLCC requires an understanding of the factors that control the dielectric properties of single layers. In general, it is found that the permittivity of $BaTiO_3$ films rises substantially with the processing temperature **[30, 31]**. Typically, in order to achieve permittivities greater than >1000, coupled with low

loss tangents, process temperatures >800 °C should be employed. Among the substrates that have been employed for this purpose are Ni and Cu. For example, the thermal expansion coefficient of Ni foils ($13x10^{-6}/^{o}C$) and barium titanate (cubic, $9.8x10^{-6}/^{o}C$) allows processing at temperature greater than $1000^{o}C$ without film cracking. Dawley et al. (see **Fig. 1.3a**) have shown that a permittivity of 1500 can be obtained from highly oriented barium strontium titanate films deposited on Ni foils via chemical solution deposition with subsequent heat treatment at low oxygen pressure ($900^{o}C$, 10^{-18} atm pO_2) **[32]**. Likewise, Nagata et al. (see **Fig. 1.3b**) has shown comparable permittitivities in pure barium titanate films on high purity Ni foils **[29]**. Ihlefeld et al. (see **Fig. 1.3c**) reported much higher dielectric constants ($\varepsilon_r \sim 2500$) with high tunability from barium titanate films on Cu foil **[33]**. Following the procedures adopted in MLCCs production, Ihlefeld's and Nagata's work utilizes two step heat treatments: a sintering step and re-oxidation. Yuan et al. studied pulse laser deposited barium titanate thin film on Ni tape using NiO as a buffer layer **[34]**. The electrical data for these films appear to be characteristic of a lossy capacitor.

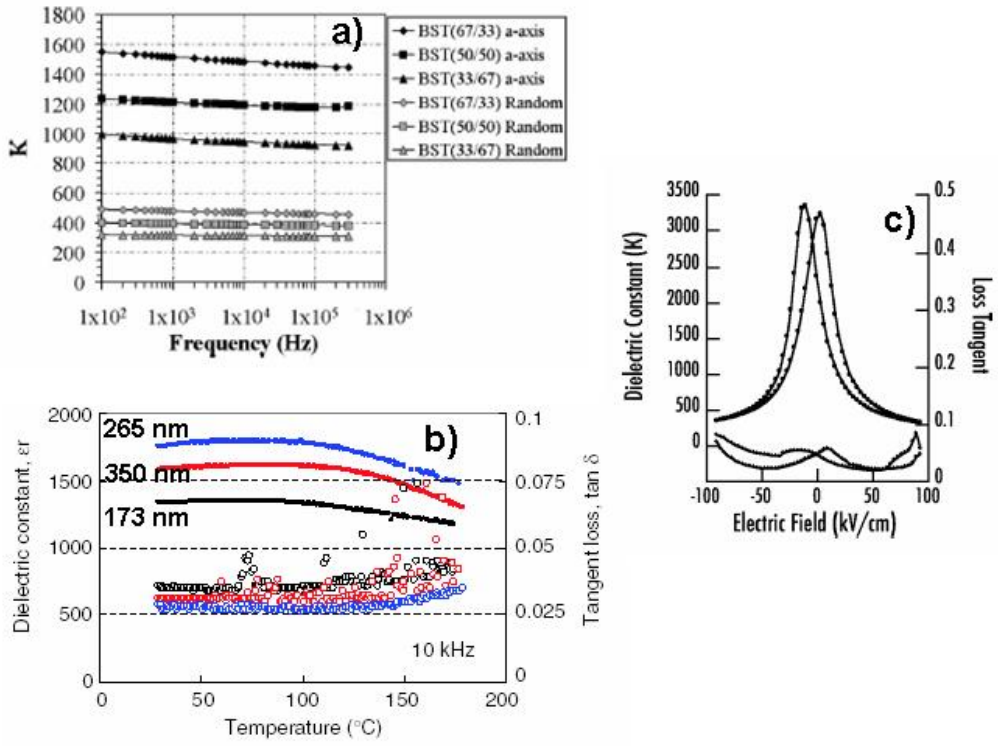

Fig. 1.3 Dielectric properties of a) (Ba,Sr)TiO_3 films on Ni foil **[32]**, b) $BaTiO_3$ films on Ni foils **[29]** and c) $BaTiO_3$ films on Cu foil **[33]**

1.2 Objectives

Although barium titanate thin films on Ni foil have shown promising electrical properties, there are many unresolved questions that form the basis for the research presented in this thesis. Firstly, the science inherent in processing chemical solution derived films under low oxygen partial pressure conditions is not well understood. In particular, the role of pyrolysis conditions, rapid thermal annealing, the high temperature crystallization step, and the reoxidation in controlling the film thickness, residual carbon content, interface quality, and grain size are not at present, understood. Secondly, there are few methods available to non-destructively characterize the $BaTiO_3$/Ni interface. In

this work, X-ray diffraction, spectroscopic ellipsometry, and transmission electron microscopy are employed in an attempt to develop highly sensitive means for interrogating the interface in the model system of films on foils. Finally, the microstructure-processing-property relations in the films were explored.

References

[1] M. Randall, D. Skamser, T. Kinard, J. Qazi, A. Tajuddin, S. Trolier-McKinstry, C. Randall, S. W. Ko and T. Dechakupt "Thin Film MLCC," In CARTS USA 2007 Symposium Proceeddings, Albuquerque, NM, Albuquerque, NM, 2007.

[2] H. Kishi, Y. Mizuno and H. Chazono, "Base-Metal Electrode-Multilayer Ceramic Capacitors: Past, Present and Future Perspectives," *Japanese Journal of Applied Physics Part 1-Regular Papers Short Notes & Review Papers*, **42** [1], 1-15 (2003).

[3] C. A. Randall, "Scientific and Engineering Issues of the State-of-the-Art and Future Multilayer Capacitors," *Journal of the Ceramic Society of Japan*, **109** [1], S2-S6 (2001).

[4] A. J. Moulson and J. M. Herbert, *Electroceramics*. 2nd ed.; Chapman & Hall: London, 1990.

[5] G. Y. Yang, E. C. Dickey, C. A. Randall, D. E. Barber, P. Pinceloup, M. A. Henderson, R. A. Hill, J. J. Beeson and D. J. Skamser, "Oxygen Nonstoichiometry and Dielectric Evolution of $BaTiO_3$. Part I - Improvement of Insulation Resistance with Reoxidation," *Journal of Applied Physics*, **96** [12], 7492-7499 (2004).

[6] G. Y. Yang, G. D. Lian, E. C. Dickey, C. A. Randall, D. E. Barber, P. Pinceloup, M. A. Henderson, R. A. Hill, J. J. Beeson and D. J. Skamser, "Oxygen Nonstoichiometry and Dielectric Evolution of $BaTiO_3$. Part II - Insulation Resistance Degradation under Applied dc Bias," *Journal of Applied Physics*, **96** [12], 7500-7508 (2004).

[7] W. A. Schulze, L. E. Cross and W. R. Buessem, "Degradation of $BaTiO_3$ Ceramic under High AC Electric-field," *Journal of the American Ceramic Society*, **63** [1-2], 83-87 (1980).

[8] H. Chazono and H. Kishi, "DC-Electrical Degradation of the BT-Based Material for Multilayer Ceramic Capacitor with Ni Internal Electrode: Impedance Analysis and Microstructure," *Japanese Journal of Applied Physics Part 1-Regular Papers Short Notes & Review Papers*, **40** [9B], 5624-5629 (2001).

[9] S. Sumita, M. Ikeda, Y. Nakano, K. Nishiyama and T. Nomura, "Degradation of Multilayer Ceramic Capacitors with Nickel Electrodes," *Journal of the American Ceramic Society*, **74** [11], 2739-2746 (1991).

[10] R. Waser, T. Baiatu and K. H. Hardtl, "DC Electrical Degradation of Perovskite-type Titanates.1. Ceramics," *Journal of the American Ceramic Society*, **73** [6], 1645-1653 (1990).

[11] J. Yamamatsu, N. Kawano, T. Arashi, A. Sato, Y. Nakano and T. Nomura, "Reliability of Multilayer Ceramic Capacitors with Nickel Electrodes," *Journal of Power Sources*, **60** [2], 199-203 (1996).

[12] H. Saito, H. Chazono, H. Kishi and N. Yamaoka, "X7R Multilayer Ceramic Capacitors with Nickel Electrodes," *Japanese Journal of Applied Physics Part 1-Regular Papers Short Notes & Review Papers*, **30** [9B], 2307-2310 (1991).

[13] Y. Okino, H. Shizuno, S. Kusumi and H. Kishi, "Dielectric-Properties of Rare-earth-oxide-doped $BaTiO_3$ Ceramics Fired in Reducing Atmosphere," *Japanese Journal of Applied Physics Part 1-Regular Papers Short Notes & Review Papers*, **33** [9B], 5393-5396 (1994).

[14] H. Shizuno, S. Kusumi, H. Saito and H. Kishi, "Properties of Y5V Multilayer Ceramic Capacitors with Nickel Electrodes," *Japanese Journal of Applied Physics Part 1-Regular Papers Short Notes & Review Papers*, **32** [9B], 4380-4383 (1993).

[15] Y. Mizuno, Y. Okino, N. Kohzu, H. Chazono and H. Kishi, "Influence of the Microstructure Evolution on Electrical Properties of Multilayer Capacitor with Ni Electrode," *Japanese Journal of Applied Physics Part 1-Regular Papers Short Notes & Review Papers*, **37** [9B], 5227-5231 (1998).

[16] S. Sato, Y. Nakano, A. Sato and T. Nomura, "Mechanism of Improvement of Resistance Degradation in Y-doped $BaTiO_3$ Based MLCCs with Ni Electrodes under Highly Accelerated Life Testing," *Journal of the European Ceramic Society*, **19** [6-7], 1061-1065 (1999).

[17] M. R. Opitz, K. Albertsen, J. J. Beeson, D. F. Hennings, J. L. Routbort and C. A. Randall, "Kinetic Process of Reoxidation of Base Metal Technology $BaTiO_3$-Based Multilayer Capacitors," *Journal of the American Ceramic Society*, **86** [11], 1879-1884 (2003).

[18] C. Metzmacher and K. Albertsen, "Microstructural Investigations of Barium Titanate-based Material for Base Metal Electrode Ceramic Multilayer Capacitor," *Journal of the American Ceramic Society*, **84** [4], 821-826 (2001).

[19] M. Shiojiri, T. Isshiki, H. Saijo, M. Tsujikura, A. Nakada, Y. Nakano, M. Ikeda and T. Nomura, "High-Resolution Electron-Microscopy Study of Domain Boundaries and Dislocation Loops in $BaTiO_3$ Crystals," *Physica Status Solidi A-Applied Research*, **129** [2], 353-362 (1992).

[20] G. Y. Yang, E. C. Dickey, C. A. Randall, M. S. Randall and L. A. Mann, "Modulated and Ordered Defect Structures in Electrically Degraded Ni-$BaTiO_3$ Multilayer Ceramic Capacitors," *Journal of Applied Physics*, **94** [9], 5990-5996 (2003).

[21] D. I. Woodward, I. M. Reaney, G. Y. Yang, E. C. Dickey and C. A. Randall, "Vacancy Ordering in Reduced Barium Titanate," *Applied Physics Letters*, **84** [23], 4650-4652 (2004).

[22] G. Y. Yang, S. I. Lee, Z. J. Liu, C. J. Anthony, E. C. Dickey, Z. K. Liu and C. A. Randall, "Effect of Local Oxygen Activity on Ni-$BaTiO_3$ Interfacial Reactions," *Acta Materialia*, **54** [13], 3513-3523 (2006).

[23] L. Chen, X. H. Wang, B. Qiao, X. Y. Deng, Z. L. Gui and L. T. Li, "Electrode-ceramic Inter-diffusion of $Ba(Ti,Zr)O_3$-based Y5V MLCCs with Ni Electrodes," *Journal of the American Ceramic Society*, **89** [12], 3734-3738 (2006).

[24] T. J. Yosenick, D. V. Miller, R. Kumar, J. A. Nelson, C. A. Randall and J. H. Adair, "Synthesis of Nanotabular Barium Titanate via a Hydrothermal Route," *Journal of Materials Research*, **20** [4], 837-843 (2005).

[25] C. Pithan, D. Hennings and R. Waser, "Progress in the Synthesis of Nanocrystalline $BaTiO_3$ Powders for MLCC," *International Journal of Applied Ceramic Technology*, **2** [1], 1-14 (2005).

[26] Y. L. Song, X. L. Liu, J. Q. Zhang, X. Y. Zou and J. F. Chen, "Rheological Properties of Nanosized Barium Titanate Prepared by HGRP for Aqueous Tape Casting," *Powder Technology*, **155** [1], 26-32 (2005).

[27] Y. Sakabe, Y. Takeshima and K. Tanaka, "Multilayer Ceramic Capacitors with Thin $(Ba,Sr)TiO_3$ Layers by MOCVD," *Journal of Electroceramics*, **3** [2], 115-121 (1999).

[28] I. P. Koutsaroff, A. Kassam, M. Zelner, P. Woo, L. McNeil, T. Bernacki, A. Cervin-Lawry and A. Patel, Dielectric Properties of $(Ba,Sr)TiO_3$ Thin Film Capacitors

Fabricated on Alumina Substrates. In *Materials Research Society Symposium Proceedings*, Boston, MA, 2003; Vol. 748, pp 413-422.

[29] H. Nagata, S. W. Ko, E. Hong, C. A. Randall and S. Trolier-McKinstry, "Microcontact Printed $BaTiO_3$ and $LaNiO_3$ Thin Films for Capacitors," *Journal of the American Ceramic Society*, **89** [9], 2816-2821 (2006).

[30] J. Thongrueng, K. Nishio, K. Nagata and T. Tsuchiya, "Preparation and Characterization of Ferroelectric $BaTi_{0.91}(Hf_{0.5},Zr_{0.5})_{0.09}O_3$ Thin Films by Sol-gel Process using Titanium and Zirconium Alkoxides," *Japanese Journal of Applied Physics Part 1-Regular Papers Short Notes & Review Papers*, **39** [9B], 5393-5398 (2000).

[31] W. C. Yi, T. S. Kalkur, E. Philofsky, L. Kammerdiner and A. A. Rywak, "Dielectric Properties of Mg-doped $Ba_{0.96}Ca_{0.04}Ti_{0.84}Zr_{0.16}O_3$ Thin Films Fabricated by Metalorganic Decomposition Method," *Applied Physics Letters*, **78** [22], 3517-3519 (2001).

[32] J. T. Dawley and P. G. Clem, "Dielectric Properties of Random and < 100 > Oriented $SrTiO_3$ and $(Ba,Sr)TiO_3$ Thin Films Fabricated on < 100 > Nickel Tapes," *Applied Physics Letters*, **81** [16], 3028-3030 (2002).

[33] J. Ihlefeld, B. Laughlin, A. Hunt-Lowery, W. Borland, A. Kingon and J. P. Maria, "Copper Compatible Barium Titanate Thin Films for Embedded Passives," *Journal of Electroceramics*, **14** [2], 95-102 (2005).

[34] Z. Yuan, J. Liu, J. Weaver, C. L. Chen, J. C. Jiang, B. Lin, V. Giurgiutiu, A. Bhalla and R. Y. Guo, "Ferroelectric $BaTiO_3$ Thin Films on Ni Metal Tapes using NiO as Buffer Layer," *Applied Physics Letters*, **90** [20], (2007).

Chapter 2

Literature Review

2.1 Dielectric properties

The dielectric constant (ε_r) is a macroscopic measurement describing the ability of a material to polarize under an applied electric field, relative to that of vacuum. **Fig. 2.1a** shows a schematic of a parallel plate capacitor with vacuum as the dielectric. The charge stored in the capacitor when it is connected to a DC voltage is due to the permittivity of vacuum. When a dielectric is inserted between the metal plates, polarization in the dielectric creates bound surface charges (see **Fig. 2.1b**). The surface charges induce free charges on the metal plates, as shown in **Fig. 2.1c**. The capacitance (C) of the capacitor is proportional to the dielectric constant of the insulator and also depends on its geometry as described in **Eq. 2.1**.

$$C = \varepsilon_0 \varepsilon_r \frac{A}{d} \qquad \textbf{Eq. 2.1}$$

where ε_0 is the permittivity of vacuum (8.85×10^{-12} F/m). The thickness (m) and active area (m^2) of capacitor are given by d and A, respectively.

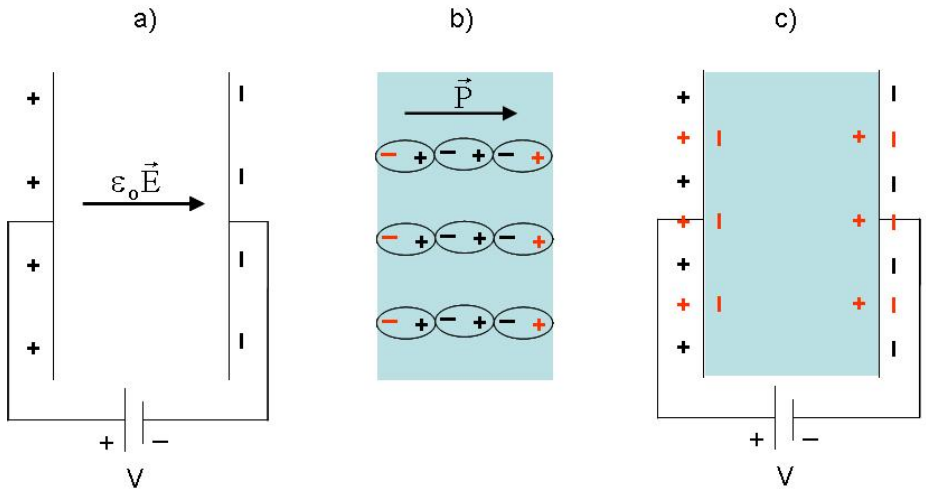

Fig. 2.1 a) Capacitor with vacuum between two parallel plates

b) Polarization of charges and net surface charges at the faces of dielectric

c) Capacitor with inserted dielectric showing bound charges at the dielectric faces and an increase in free charge on the metal plates

Since the total charge developed on the metal plates is induced by the permittivity in vacuum and the polarization of the dielectric (P), the dielectric displacement (D) of the capacitor is described as **[1]**:

$$\vec{D} = \varepsilon_0 \vec{E} + \vec{P}$$

where E is the applied electrical field. For a small AC signal, the polarization responds linearly to the electric field.

$$\vec{P} = \varepsilon_0 \chi \vec{E}$$

or

$$\vec{D} = \varepsilon_0 \varepsilon_r \vec{E}$$

where χ and ε_r are the dielectric susceptibility and relative dielectric permittivity of the dielectric material, respectively and $\chi = \varepsilon_r - 1$.

For an AC circuit, the polarization oscillates with the electric field. Because of inertia, part of the current is phase shifted with respect to the applied voltage (see **Fig. 2.2a** and **b**). As a result, there is current loss and energy dissipation in the ac circuit. Consequently, in an AC field, the permittivity of dielectrics is complex:

$$\varepsilon_r = \varepsilon_r^{'} + i\varepsilon_r^{''}$$

where $\varepsilon_r^{'}$ and $\varepsilon_r^{''}$ are the real and imaginary parts of the complex dielectric constant (ε_r), respectively. i is $\sqrt{-1}$. The dielectric loss is given by:

$$\tan\delta = \frac{\varepsilon_r^{''}}{\varepsilon_r^{'}}$$

In reality, dielectrics are not perfect insulators, but contain some point defects, i.e anion and cation interstitials or vacancies, as well as electronic carriers that lead to some conductivity. Therefore, practically, the measured tan δ consists of two types of loss: 1) dielectric loss due to inertia of charge oscillation and 2) leakage current due to flow of charge through dielectric or dc conductivity.

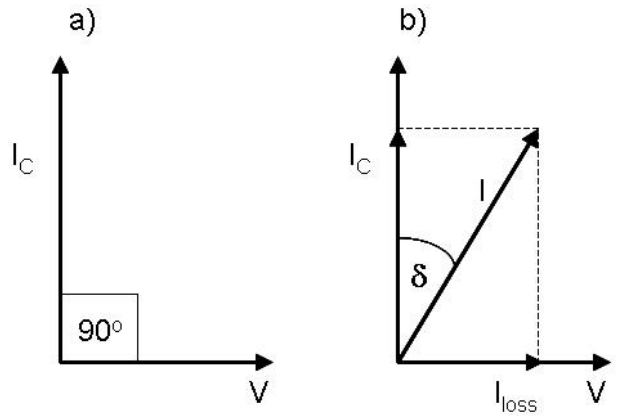

Fig. 2.2 Phasor diagram for a) perfect capacitor and b) real capacitor (V is applied voltage, I is the total current, I_C is the charging current and I_{loss} is the loss current)

The dielectric constant is attributed to various polarization mechanisms: electronic, ionic, dipolar (or orientational) and space charge polarization, as shown in **Fig.2.3a [1]**. The total polarization under an applied electric field can be described as

$$\vec{P}_{total} = \vec{P}_{elec} + \vec{P}_{ion} + \vec{P}_{dip} + \vec{P}_{sc}$$

Electronic polarization ($\vec{P}_{elec}$) occurs in all dielectrics. The process involves displacement of the nucleus with respect to the center of the electron cloud. Ionic polarization ($\vec{P}_{ion}$) is the relative displacement of anions and cations in ionic crystals. Dipolar (or orientational) polarization ($\vec{P}_{dp}$) results from aligning the permanent dipoles which exist in some dielectrics. Space charge polarization ($\vec{P}_{sc}$) is due to movement of charge carriers until they are blocked by insulating interfaces.

Each polarization mechanism has varying time response. A given polarization mechanism contributes to the dielectric only at frequencies that are low enough that the

charges can keep up with the oscillation. **Fig. 2.3b** shows a schematic of the dielectric constant and loss, showing the contributions of the polarization mechanism over a wide frequency range. The electronic and ionic polarization mechanisms respond to the applied field up to the optical (~10^{14} Hz) and infrared (~10^{11} Hz) regions, respectively. The polarization shows a resonance when the applied frequency matches the natural angular frequency of the electronic and ionic mechanisms. Dipolar and space charge polarization contribute to the dielectric constant at lower frequency. If the frequency is so high that dipoles cannot follow the alternating field, the polarization from the dipoles decreases and becomes zero. Relaxation processes are also associated with dielectric loss.

a)

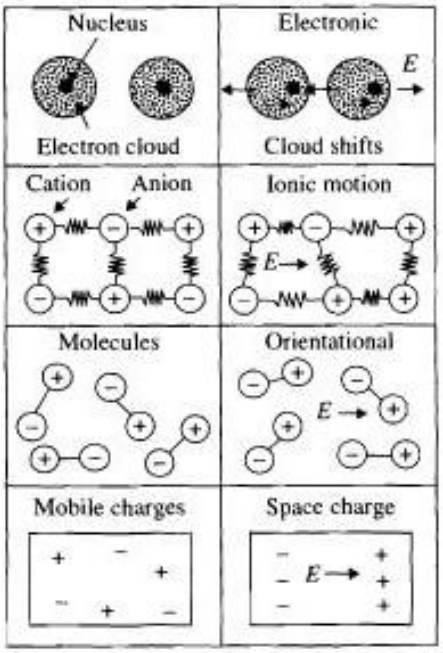

b)

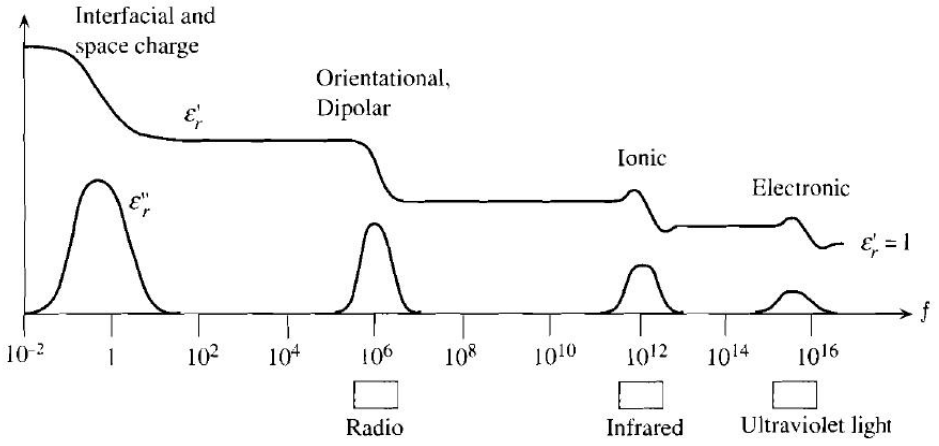

Fig. 2.3 a) Polarization mechanisms **[2]**

b) Frequency dependence of ε′ and ε′′ **[1]**. Note that in ferroelectric materials, the dipolar polarizability is not lost until the GHz frequency range.

2.2 Barium titanate materials for capacitor applications

Barium titanate is the most widely utilized material for multilayer capacitors because of its high dielectric constant over a wide temperature range. The prototype structure of barium titanate is perovskite. The general formula of the perovskite structure is ABO_3, where A is a large cation with 1+, 2+, or 3+ ion charge (i.e. Ba^{2+}) and B is a small and highly charged (3+, 4+ or 5+) cation (i.e. Ti^{4+}). As shown in **Fig. 2.4** for the cubic prototype, the Ba^{2+} ions (A site) are at the eight corners of the unit cell and the O^2 ions are at the face centers of the cube. Each Ba^{2+} ion is surrounded by 12 O^2 ions that are at the face centers of nearby cubes. The Ti^{4+} ion (B site) sits at the center of six oxygen ions, forming a TiO_6 octahedral cage. Another point of view (right hand side of the figure) shows a dodecahedral hole filled with Ba^{2+} and corner sharing of Ti octahedra in the perovskite framework.

In barium titanate, the cation sizes (Ba and Ti) do not perfectly fit the ideal perovskite structure, which is described using the tolerance factor **[3]**

$$t = \frac{(R_A + R_O)}{\sqrt{2}(R_B + R_O)}$$

where R is the radius of each ion. A, B and O are Ba, Ti and O, respectively. The tolerance factor for barium titanate (1.06, or >1), suggests that Ti^{4+} ion is too small for the octahedral site. At temperatures higher than T_c (130^{o}C), the high symmetry cubic phase is stable. The cubic structure shows a high dielectric constant with paraelectric behavior, i.e. the net polarization returns to zero after removing an applied electric field. However, as temperature decreases, the TiO_6 cage is distorted by displacement of the Ti^{4+} ion off the center of the unit cell, and the cubic structure becomes unstable.

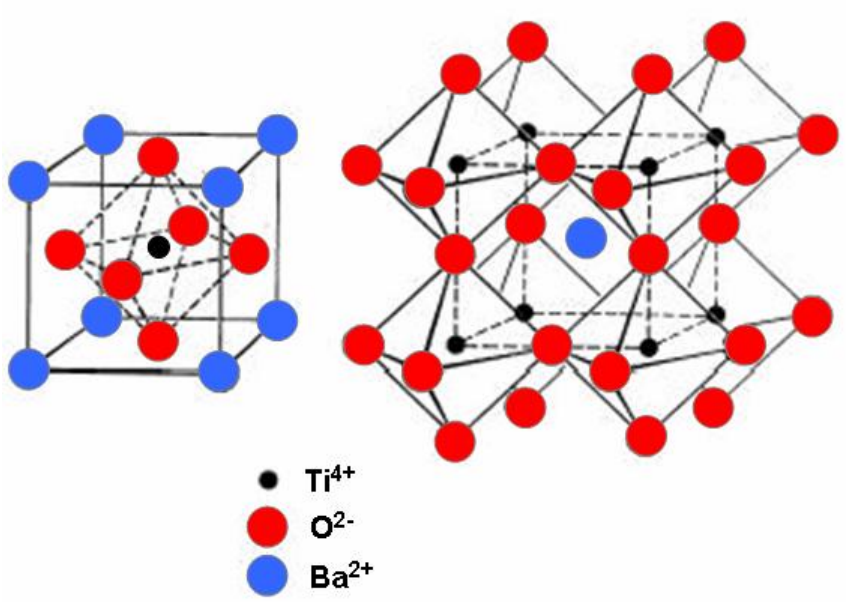

Fig. 2.4 Schematic of the cubic perovskite structure of the high temperature $BaTiO_3$ unit cell (Adapted from Kingery et al. 1991 **[4]**)

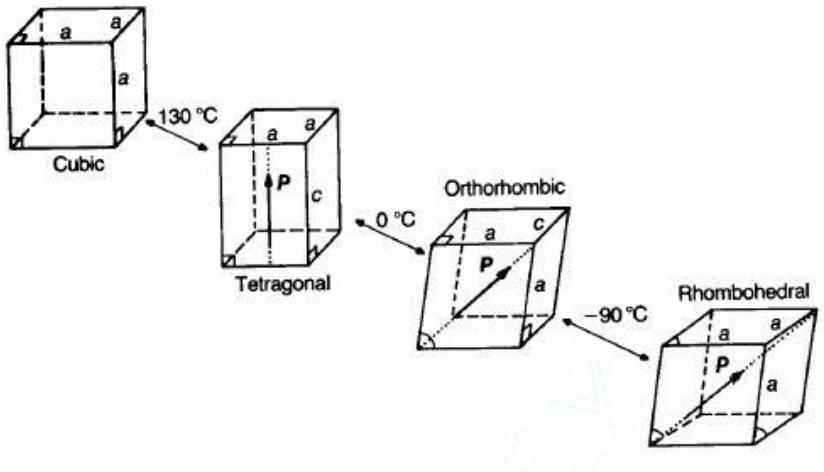

Fig. 2.5 Phase transition sequence in $BaTiO_3$ (Figure from Moulson et al. **[5]**)

Fig. 2.5 shows the structure changes in barium titanate with temperature. Below T_c, the structure is distorted by shifting the Ti^{4+} ion closer to one O^{2-} ion at a cube face (i.e. parallel to one of the <100> directions of the original cube). As a result, the cube is stretched along the edge parallel to the Ti^{4+} displacement; the perpendicular edge contract, resulting in a tetragonal structure. Upon further cooling, the structure changes to orthorhombic and rhombohedral distortions at approximately 0^oC and -90^oC, respectively. The Ti^{4+} ion is shifted along the pseudocubic <110> for the orthorhombic phase and <111> for the rhombohedral phase. Below T_C (in the tetragonal, orthorhombic and rhombohedral structures), a spontaneous polarization is retained even in the absence of an electric field. These distorted structures possess ferroelectricity because the spontaneous polarization is reorientable.

The dielectric constant of a barium titanate single crystal as a function of temperature is shown in **Fig. 2.6**. The anomaly in the dielectric constant at T_c is due to the high distortability of the structure at the phase transition. The dielectric constant above T_c follows the Curie-Weiss law.

$$\varepsilon_r' = \varepsilon_o + \frac{C}{(T - T_o)}$$

where C is the Curie constant and T_o is the Curie-Weiss temperature. As barium titanate undergoes its first order transition, T_o is slightly less than T_c and a plot of the inverse dielectric constant ($1/\varepsilon$) has a finite value at T_c. Below T_c, the dielectric constant along the *c* axis is smaller than that along the *a* axis because the displaced Ti^{4+} is tightly bound to the closest oxygen along the *c* axis **[6]**.

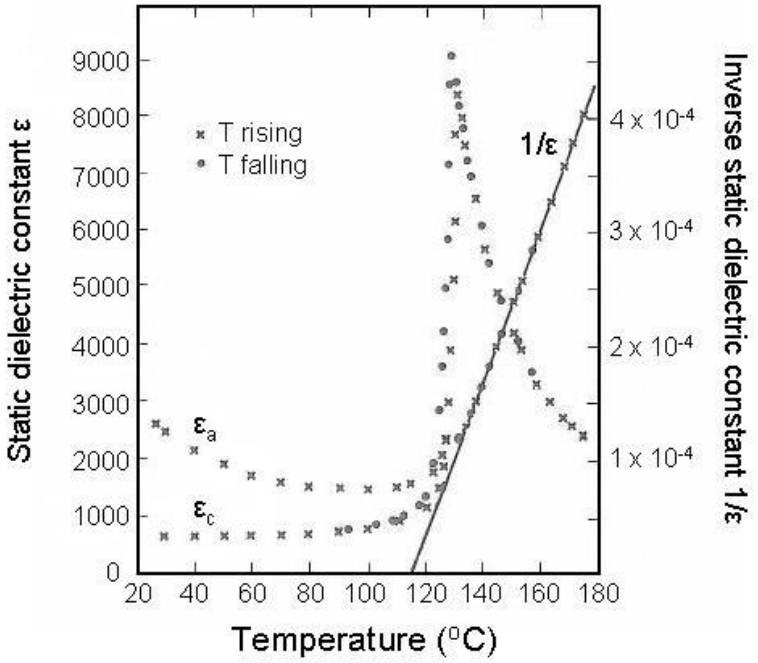

Fig. 2.6 Dielectric constant ε (equivalent to ε_r') and its inverse as a function of temperature for a $BaTiO_3$ single crystal **[7]**

2.3 Chemical solution deposition of barium titanate thin films

$BaTiO_3$ thin films have been prepared by many techniques, i.e. rf-magnetron sputtering, pulsed laser deposition, molecular beam epitaxy, metalorganic chemical vapor deposition and chemical solution deposition **[8-12]** Chemical solution deposition (CSD) has some unique advantages over the others. In principle, a stoichiometric and homogeneous composition can be obtained due to reaction at the molecular level. Incorporation of dopants into the composition is conveniently done by adding the desired precursors to the solution. In addition, large film area and inexpensive deposition methods, i.e. spin coating and dip coating are very attractive for industrial production.

Chemical solution deposition involves fabricating thin films from a chemical solution, drying to remove the liquid in the gel network and performing appropriate heat treatment to convert the as-deposited film into the desired crystalline phase. The solution is prepared by dissolving precursors containing the necessary cation species in a solvent. The cation precursors are usually carboxylates i.e. metal acetates, $M(OOCCH_3)_x$ and metalloorganic compounds i.e. alkoxides, $M(OR)_x$, where M is the metal and R is an alkyl group. The carboxylates are often used as precursors for lower-valent cations, i.e. Pb^{2+}, Sr^{2+} and Ba^{2+} **[13]**. There are several chemical routes for making thin films. The two main routes: sol-gel or chelation are included here. Hybrid processes also exist. Other processes such as metallo-organic decomposition (MOD) **[14, 15]** and Pechini routes **[16, 17]** are also used, however they are not described here.

One of the solution synthesis routes is the sol-gel process. The standard reactions in the process are hydrolysis and condensation of the alkoxide reagents:

Hydrolysis:

$$M(OR)_n + H_2O \rightarrow M(OR)_{n-1}(OH) + ROH$$

Condensation (water elimination):

$$2M(OR)_{n-1}(OH) \rightarrow M_2O(OR)_{2n-2}(OH) + H_2O$$

Condensation (alcohol elimination):

$$2M(OR)_{n-1}(OH) \rightarrow M_2O(OR)_{2n-3}(OH) + ROH$$

Hydrolysis is the reaction of a water molecule with the alkoxide, producing a hydroxyl metal alkoxide ($M(OR)_{n-1}OH$) and a released alcohol molecule (ROH).

Condensation is the further reaction of two hydroxyl metal alkoxides to form a polymeric species with metal-oxygen-metal (M-O-M) bonds.

The degree of the hydrolysis reaction can be controlled by many approaches. For a classical sol-gel process, the hydrolysis reaction occurs readily and precipitation of hydroxide species may occur. Therefore, dry chemicals and a dry atmosphere are required for solution synthesis to minimize the reaction. Alcohol exchange reactions also can slow down hydrolysis by forming a less reactive alkoxide $(M(OR')_x)$:

$$M(OR)_n + xR'OH \rightarrow M(OR')_x + ROH$$

where OR' is a less reactive polar group of an alcohol i.e. 2-methoxyethanol, which is a widely used solvent for perovskite thin films.

Another synthesis approach, called the chelating process, involves modifying the alkoxide with chelating legands, i.e. acetic acid or 2,4-pentanedione (acetylacetone) to reduce the hydrolysis reaction of the alkoxide precursor. For acetic acid, the chelation reaction is **[18]**

$$M(OR)_n + xCH_3COOH \rightarrow M(OR)_{n-x}(OOCCH_3)_x + xROH$$

The term "hybrid" refers to the use of carboxylate precursors for the A site and alkoxides for the B site in perovskite thin films. The carboxylate acid, often acetic acid, serves both to dissolve the carboxylates and also as a chelating agent for the alkoxides.

In chemical solution deposition, thin films are usually deposited through spin coating or dip coating of the solution on a substrate. After deposition, the as-deposited film is amorphous and contains a large fraction of entrapped solvent and organics associated in the gel network. To obtain the crystalline phase, generally the film is first

heat treated at low temperature (200-400^{o}C) for drying and organic pyrolysis and then subjected to higher temperature (500-700 ^{o}C) for crystallization and densification.

References

[1] S. O. Kasap, *Principles of Electronic Materials and Devices*. 3rd ed.; McGraw Hill: New York, 2006.

[2] R. E. Newnham, *Properties of Materials*. Oxford University Press: New York, 2005.

[3] F. Jona and G. Shirane, *Ferroelectric Crystals*. Pergamon Press: Frankfert am Main, 1962.

[4] W. D. Kingery, H. K. Bowen and D. R. Uhlmann, *Introduction to Ceramics*. 2nd. ed.; John Wiley & Sons: Singapore, 1991.

[5] A. J. Moulson and J. M. Herbert, *Electroceramics*. 2nd ed.; Chapman & Hall: London, 1990.

[6] B. Jaffe, W. R. Cook Jr. and H. Jaffe, *Piezoelectric Ceramics*. Academic Press: 1971.

[7] C. J. Johnson, "Some Dielectric and Electro-optic Properties of $BaTiO_3$ Single Crystals (Temperature Dependence E)," *Applied Physics Letters*, **7** [8], 221 (1965).

[8] R. Thomas, D. C. Dube, M. N. Kamalasanan and S. Chandra, "Optical and Electrical Properties of $BaTiO_3$ Thin Films Prepared by Chemical Solution Deposition," *Thin Solid Films*, **346** [1-2], 212-225 (1999).

[9] M. G. Norton, K. P. B. Cracknell and C. B. Carter, "Pulsed-laser Deposition of Barium-titanate Thin-films," *Journal of the American Ceramic Society*, **75** [7], 1999-2002 (1992).

[10] R. A. McKee, F. J. Walker, J. R. Conner, E. D. Specht and D. E. Zelmon, "Molecular-beam Epitaxy Growth of Epitaxial Barium Silicide, Barium Oxide, and Barium-titanate on Silicon," *Applied Physics Letters*, **59** [7], 782-784 (1991).

[11] M. H. Frey and D. A. Payne, "Nanocrystalline Barium-Titanate - Evidence for the Absence of Ferroelectricity in Sol-Gel Derived Thin-Layer Capacitors," *Applied Physics Letters*, **63** [20], 2753-2755 (1993).

[12] D. A. Neumayer, D. B. Studebaker, B. J. Hinds, C. L. Stern and T. J. Marks, "New Precursors for Barium Metal-organic Chemical-vapor-deposition - In-situ Growth of Epitaxial Barium-Titanate Film Using a Liquid Barium Precursor," *Chemistry of Materials*, **6** [7], 878-880 (1994).

[13] R. W. Schwartz, T. Schneller and R. Waser, "Chemical Solution Deposition of Electronic Oxide Films," *Comptes Rendus Chimie*, **7** [5], 433-461 (2004).

[14] W. Zhu and R. W. Vest, "Metalloorganic Decomposition Technology for PZT Films in Memory Applications," *Journal of Materials Processing Technology*, **29** [1-3], 373-384 (1992).

[15] J. R. Hanrahan, E. Sanchez, J. J. Santiago, D. H. Berry and Q. Jiang, "Synthesis of Ferroelectric Thin-Films via Metalloorganic Decomposition," *Thin Solid Films*, **202** [2], 235-242 (1991).

[16] V. Agarwal and M. L. Liu, "Preparation of Barium Cerate-based Thin Films using a Modified Pechini Process," *Journal of Materials Science*, **32** [3], 619-625 (1997).

[17] M. L. Liu and D. S. Wang, "Preparation of $La_{1-Z}Sr_zCO_{1-Y}Fe_yO_{3-X}$ Thin-films, Membranes, and Coatings on Dense and Porous Substrates," *Journal of Materials Research*, **10** [12], 3210-3221 (1995).

[18] R. W. Schwartz, "Chemical Solution Deposition of Perovskite Thin Films," *Chemistry of Materials*, **9** [11], 2325-2340 (1997).

Chapter 3

Experimental Procedure

3.1 Chemical solution deposition of $BaTiO_3$ Film

In this work, $BaTiO_3$ thin films were prepared by chemical solution deposition, following the work of Nagata et al. **[1]**. Undoped $BaTiO_3$ with a 1:1 Ba:Ti ratio was chosen for the microstructure and interface studies since it provides an excellent model system.

3.1.1 $BaTiO_3$ solution

The starting materials in this experiment were barium acetate (99.999%, Sigma-Aldrich) and Ti-isopropoxide (99.99%, Sigma-Aldrich). Acetylacetone was used as a chelating agent for Ti-isopropoxide, which is known to be a moisture-sensitive reagent. The precursors and chemicals were batched in a glove box under an Ar atmosphere. Two types of solvent were used: methanol and 2-methoxyethanol. It was found that 2-methoxyethanol-based solutions provide better wetting of the first deposited layer on a Ni foil surface.

The process-flow for preparation of methanol-based $BaTiO_3$ solutions is shown in **Fig. 3.1**. First, 0.01 mole of barium acetate was stirred in 12 ml of glacial acetic acid at 105^{o}C for 1 hour or until completely dissolved, using a rotary evaporator flushed with flowing Ar. The flask containing the barium precursor was immersed in a heated silicone oil bath and rotated at 120 rpm. In a separate flask, 2 ml of acetylacetone and 0.01 mole of titanium isopropoxide were combined. Then, the dissolved Ba precursor was poured

into the flask containing Ti. A small amount of acetic acid (6 ml) was used to rinse the remaining Ba solution from the flask. The mixture of Ba and Ti precursors was allowed to react at 105^{o}C for 1 hour. An appropriate amount (80 ml) of methanol was added to obtain 0.1 M $BaTiO_3$ solution and then the solution was stirred at room temperature until homogenized. It is noted that the volume ratio of acetic acid to methanol was approximately 1:4.

Preliminary work has shown that for the same solution concentration, the 2-methoxyethanol-based film thickness is a factor of two less than that of the methanol-based films. Therefore, 0.2 M 2-methoxyethanol based solutions were made as shown in **Fig. 3.2**. Preparation proceeded exactly as described for the methanol-based solution, including the dissolution of the barium acetate and the mixing of the Ba and Ti precursors. However, the mixture was vacuum distilled at 105^{o}C until the volume of the solution was approximately 10 ml, before re-diluting the solution to the desired molarity. It is expected that the majority of the volume loss was due to acetic acid since its boiling point (~ 118^{o}C) is lower than that of acetylacetone (~ 140^{o}C). Then, 40 ml of 2-methoxyethanol was added and stirred until homogenized.

Keeping the ratio of acetic acid to solvent to 1:4 served two purposes. First, the possibility of changing the solution charateristics (and so factors such as the degree of cross-linking, etc.) is avoided. Secondly, it was found that if the concentration of acetic acid in the solution was too high, it attacked and damaged the Ni foil surface. This complicated interpretation of the resulting spectroscopic ellipsometry data due to the roughened interface.

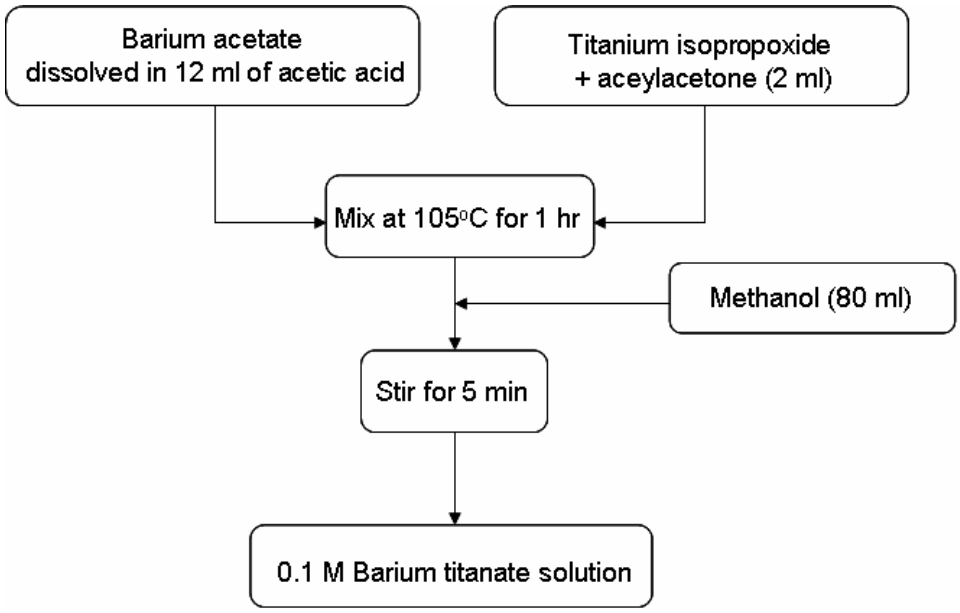

Fig. 3.1 Schematic of methanol-based solution preparation method

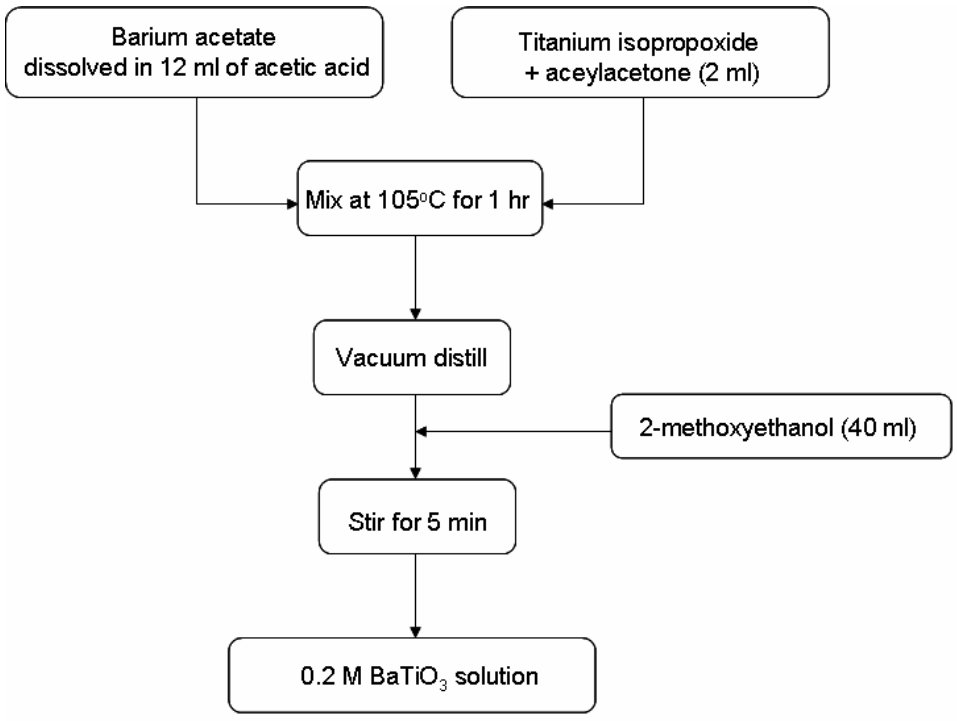

Fig. 3.2 Schematic of 2-MOE-based solution preparation method

3.1.2 Film deposition and crystallization

High purity Ni foils (99.99%, Alfa Aesar) that were 25 μm thick were used to prepare $BaTiO_3$ films on Ni substrates. The Ni foil was pre-annealed at 900°C in approximately $1x10^{-16}$ atm pO_2, using a reducing furnace which will be described in section 3.2. The pre-annealing step was to smooth the Ni surface and remove native oxide and organic contamination, if present **[1]**. Since rolled Ni foils have a finite level of surface roughness, which will be presented in chapter 5, Al_2O_3 and Si wafers were also used as substrates in some cases to provide smoother surfaces.

Fig. 3.3 shows a schematic of the preparation of $BaTiO_3$ thin films. A syringe with a 0.1 μm filter was used to dispense the solution onto the substrate. After covering the substrate surface with solution, the spinner was rotated at 3000 rpm for 30 seconds. After each deposition, the films were dried at 180°C for 3 min and then 280°C for 3 min on hotplates in air. After every two spinning/drying steps, the organic was further removed at 350°C for 1 min. Films were then heat-treated at temperatures between 600 and 750°C for 1 minute under a N_2 gas flow (23 SLPM) in a rapid thermal annealer (RTA 600, Modular Process Technology Corp., San Jose, CA). Spinning, drying and RTA annealing were repeated until the desired thickness was obtained. The films were then crystallized at 1000°C for 1 hour in $5x10^{-17}$ atm pO_2 (setting value) in a reducing furnace and then re-oxidized at 600°C for 30 minutes in $1x10^{-10}$ atm pO_2 (setting value). The heating rate of both steps in the reducing furnace was 5°C/min. The conditions employed in this work are comparable to those reported by Nagata et al. **[1]**. A schematic showing the oxygen pressures and temperatures employed for some of the steps is shown along with the Ellingham diagram in **Fig. 3.4**. It is clear that the conditions used for

reoxidation could lead to oxidation of the Ni foil, if the $BaTiO_3$ layer does not provide a sufficient kinetic barrier against oxygen diffusion.

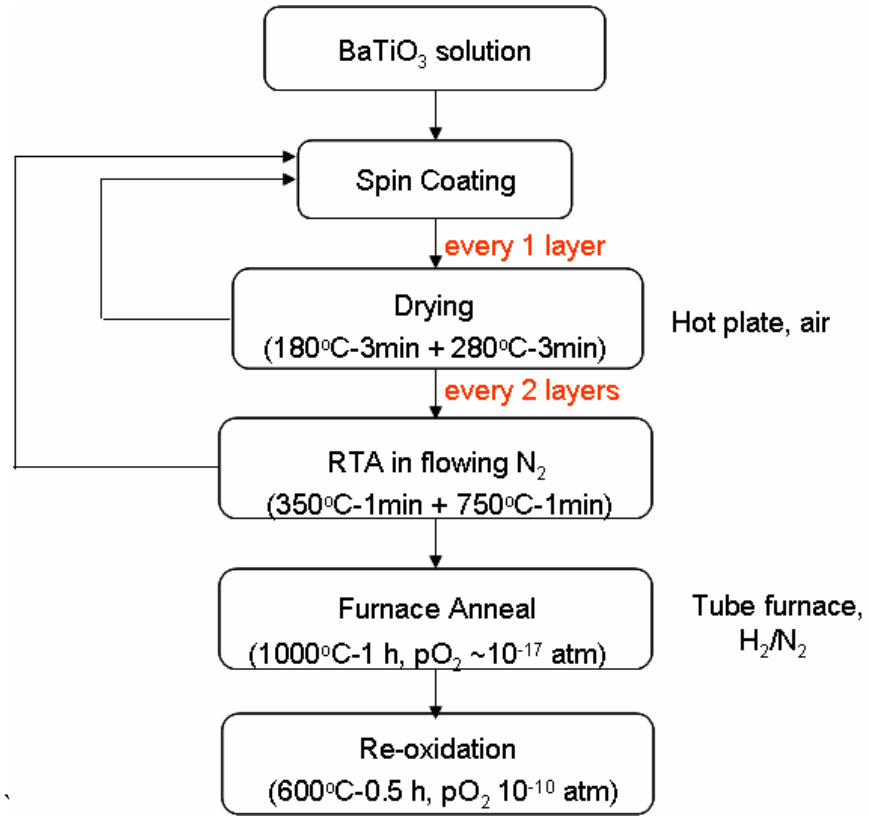

Fig. 3.3 Schematic of preparation of $BaTiO_3$ thin films

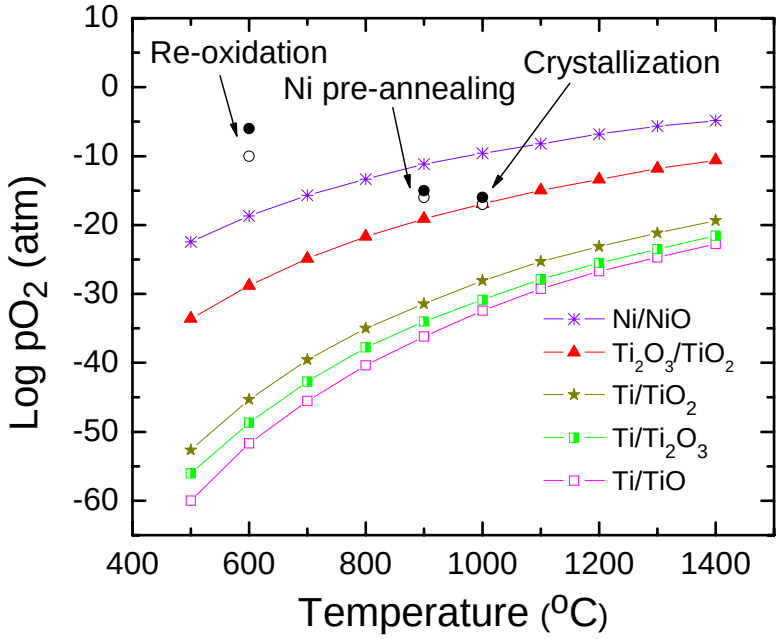

Fig. 3.4 Stability of Ni and various oxidation state of titanium (Circles, ○ and ●, shows typical setting values and measured values for the pO_2 for each heat treatment) (Adapted from Yang et al. **[2]**)

3.2 Reducing furnace system

As mentioned in sections 3.1.1 and 3.1.2, high temperature annealing of either the Ni foil or $BaTiO_3$ films on Ni foils requires a reducing atmosphere to prevent oxidation of the Ni. In this experiment, high purity nitrogen and either hydrogen or forming gas (5% H_2 and 95% N_2) were flowed into a tube furnace to control the oxygen partial pressure. Part of the nitrogen gas was directly fed to the furnace (dry nitrogen) while an appropriate amount was passed through water to carry water vapor into the furnace (wet

nitrogen). The oxygen partial pressure within the furnace was controlled by the equilibrium of hydrogen and water vapor through the following chemical reaction.

$$H_2(g) + \frac{1}{2}O_2(g) \leftrightarrow H_2O(g); \qquad K_p = \frac{P_{H_2O}}{P_{H_2} P_{O_2}^{\frac{1}{2}}} \qquad 3.1$$

and

$$\ln K_p = -\frac{\Delta G^o}{RT} \qquad 3.2$$

K_p is the equilibrium constant which is dependent on temperature (T in Kelvin) and ΔG^o (J) is the standard Gibbs free energy of formation of water vapor **[3]**.

$$\Delta G^o = -246{,}740 + 54.81T \qquad 3.3$$

For a desired temperature and oxygen partial pressure, K_p is calculated from equation 3.2 and 3.3, then the ratio of P_{H_2O} and P_{H_2} required in the furnace were obtained. The total pressure and total gas flow in the furnace were 1 atm and 500 cc/min, respectively. Once the flow rate of H_2 is defined (usually in the range of 1 to 50 cc/min), the flow rate of wet N_2 (which helps determine the water vapor pressure, P_{H_2O}) is calculated. The dry N_2 is added to maintain the total gas flow (500 cc/min). Typical gas flows for different reducing conditions, i.e. crystallization and re-oxidation are shown in Table 3.1. For the re-oxidation condition (600°C), $P_{H_2} \approx 2P_{O_2}$ is used in equation 3.1 because there is no H_2 gas in the system.

Fig. 3.5 is a schematic of the reducing furnace. The pressure of water vapor and hydrogen was controlled by mass flow controllers (MFC, MKS Type 1179A). The outgoing gas was passed through a flask containing silicone oil to insure flow by

checking the bubble rate. An extra empty flask was put between the end of the furnace and the oil container to trap any oil from backstreaming into the furnace system. An oxygen probe with a zirconia-based sensor and a thermocouple was used to read the actual oxygen partial pressure and temperature at the center of the furnace. One sensor surface is exposed to the reducing atmosphere in the furnace while the other is in contact with an air reference containing 20% oxygen. The voltage developed due to the difference in oxygen content between the two surfaces was measured. Then, using an independent measurement of temperature, the oxygen pressure in the furnace was calculated from the Nernst equation.

$$pO_2(\text{atm}) = 0.209 \exp\left(\frac{-46.42E}{T}\right) \qquad 3.3$$

where E is the oxygen signal (mV) and T is temperature (K). Since the operating temperature of the sensor is between 700^{o}C and 1700^{o}C, it is reasonable that the pO_2 read during the 600^{o}C re-oxidation step may differ significantly from the setting value, as shown in **Table 3.1**.

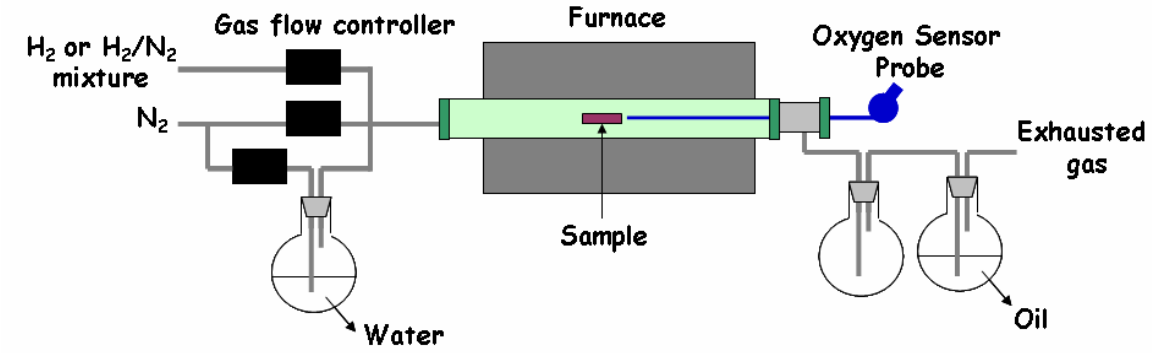

Fig. 3.5 Schematic of reducing furnace system

Table 3.1 Reducing setting condition and actual pO_2 measured by an oxygen sensor

Reducing condition (^oC, atm pO_2)	**Gas flow rate (SLPM)**			**Actual pO_2** (atm)
	H_2	**Wet N_2**	**Dry N_2**	
900^{o}C, 1x10^{-16}	**10**	**136.5**	**353.5**	**1x10^{-15}**
1000^{o}C, 5x10^{-17}	**10**	**40.98**	**449.02**	**1x10^{-16}**
600^{o}C, 1x10^{-10}	**-**	**27.9**	**472.1**	**2x10^{-6}**

3.3 Spectroscopic ellipsometry

3.3.1 Introduction to ellipsometry

Spectroscopic ellipsometry (SE) was used to determine the depth profile, film thickness, microstructure and optical constants of the $BaTiO_3$ films on Ni foils and other substrates. Ellipsometry measures the change in the polarization state of a light beam after reflection from a sample. For the rotating analyzer spectroscopic ellipsometer which was used in this experiment, linearly polarized light is incident on a sample and elliptically polarized light is produced, as illustrated in **Fig. 3.6**. The basic configuration of the ellipsometer is shown in **Fig. 3.7**. White light from a Xe lamp is separated into different wavelengths by a monochromator. The monochromatic light is passed through a polarizer before hitting the sample surface. At each wavelength, the intensity of the reflected light is measured as a function of analyzer position by a photomultiplier tube (PMT), thus providing a measurement of the polarization state of the reflected light.

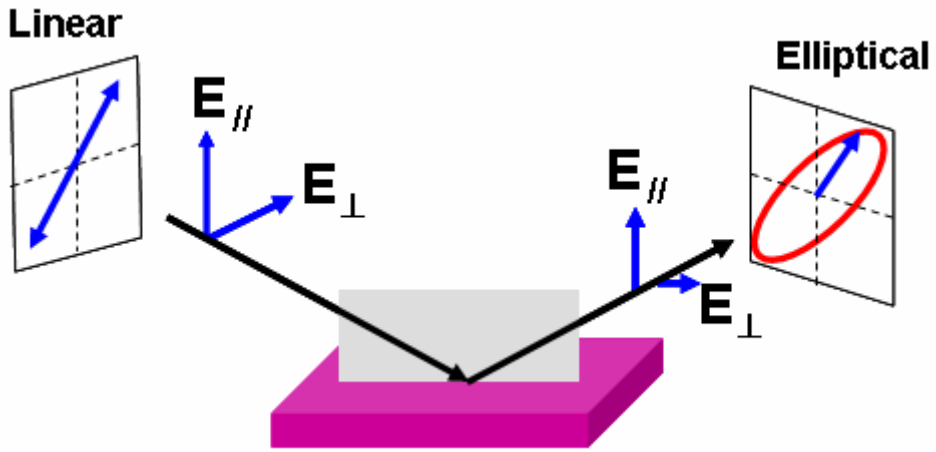

Fig. 3.6 Reflection of light at an interface

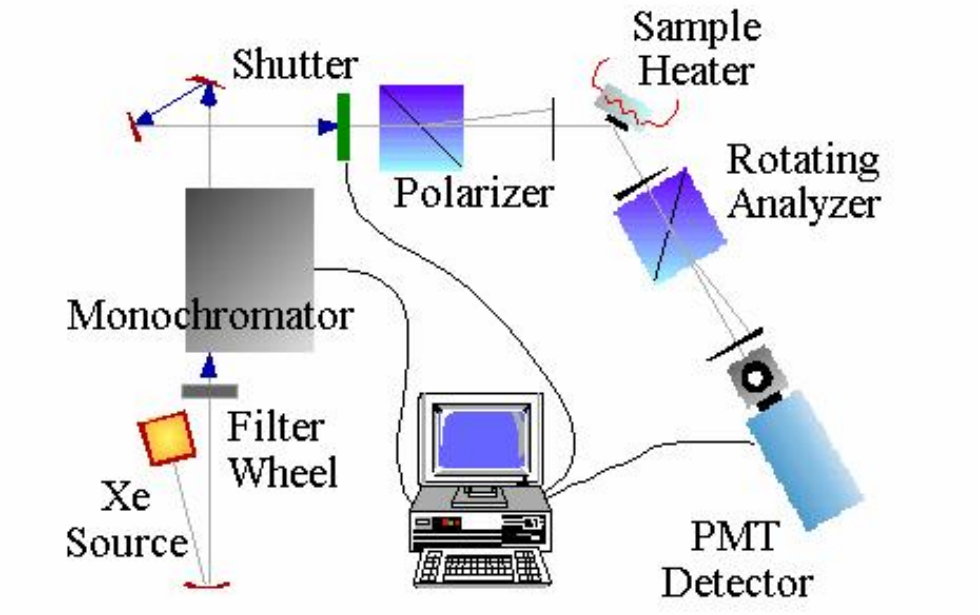

Fig. 3.7 Schematic of rotating-analyzer spectroscopic ellipsometer **[4]**

Two parameters, the relative phase shift (Δ) and amplitude change (tanΨ) of the parallel $(E_{//})$ and perpendicular $(E_{\perp})$ components of the light wave, are measured **[5]**.

$$\Delta = \delta_r - \delta_i \qquad 3.4$$

and

$$\tan\Psi = \frac{|r_{//}|}{|r_{\perp}|} \qquad 3.5$$

where δ is the phase difference between $E_{//}$ and $E_{\perp}$ of the reflected and incident light; the subscript r and i denote the reflected and incident waves. The parameters $r_{//}$ and $r_{\perp}$ are the complex Fresnel reflection coefficient of $E_{//}$ and $E_{\perp}$, respectively. For reflection of light from a homogeneous isotropic material, the Fresnel coefficients are **[5]**:

$$r_{//} = \frac{N_1 \cos\phi_0 - N_0 \cos\phi_1}{N_1 \cos\phi_0 + N_0 \cos\phi_1} \quad 3.6$$

$$r_{\perp} = \frac{N_0 \cos\phi_0 - N_1 \cos\phi_1}{N_0 \cos\phi_0 + N_1 \cos\phi_1} \quad 3.7$$

where ϕ_0 and ϕ_1 are angles of incidence and refraction, respectively and N_1 and N_2 are the complex refractive indices of air and the sample, respectively at the wavelength (λ) used.

For multiple interfaces, like a thin film on a substrate as shown in **Fig. 3.8**, the total reflection coefficients count reflections from all interfaces and are defined as

$$r_{//} = \frac{r_{//,01} + r_{//,12} e^{-2i\beta}}{1 + r_{//,01} r_{//,12} e^{-2i\beta}} \quad 3.8$$

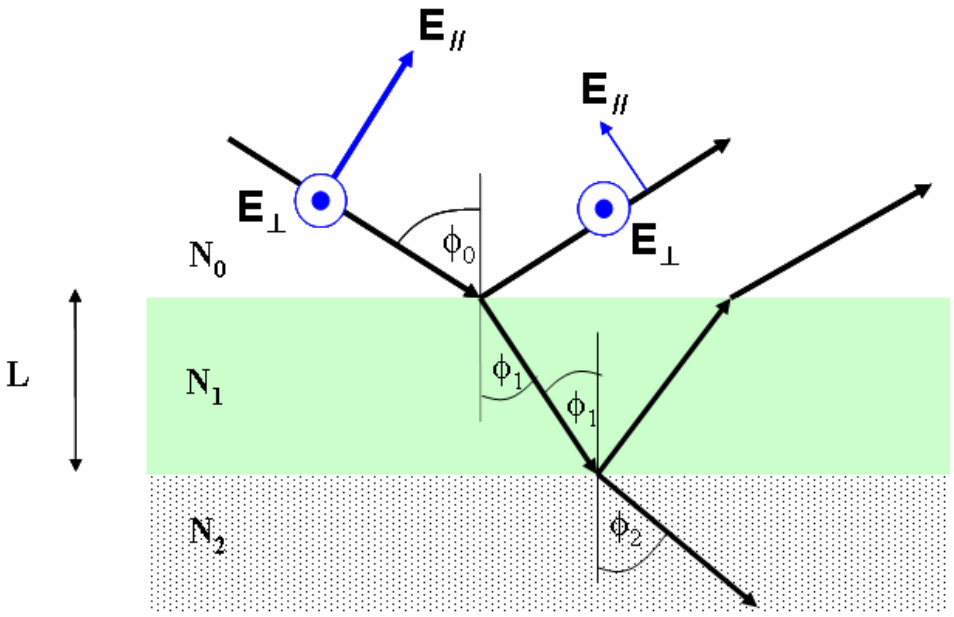

Fig. 3.8 Reflection of light from a thin film on a substrate

and $$r_{\perp} = \frac{r_{\perp,01} + r_{\perp,12} e^{-2i\beta}}{1 + r_{\perp,01} r_{\perp,12} e^{-2i\beta}} \quad 3.9$$

where $r_{//,ij}$ and $r_{\perp,ij}$ are the Fresnel reflection coefficients of the parallel and perpendicular waves traveling from medium i to j, respectively.

$$\beta = 2\pi\left(\frac{L}{\lambda}\right) N_1 \cos\phi_1 \quad 3.10$$

When there are multiple films, the measured delta and psi are influenced by the optical depth profile of the entire stack. Δ and $\tan\Psi$ can be expressed as:

$$\tan\Psi e^{i\Delta} = \frac{r_{//}}{r_{\perp}} = \rho(N_i, L_i, \lambda) \quad 3.11$$

Therefore, the measured Δ and Ψ contain information on the optical properties and thickness of the film(s). Because it is relative measurement, rather than an absolute measurement of intensities, ellipsometry is a very accurate and reproducible. Data at different wavelengths obtained from spectroscopic measurements enable analysis of samples with complicated depth profiles.

3.3.2 Data collection

System alignment and calibrations of the rotating-analyzer spectroscopic ellipsometer were performed as described by Chindaudom **[6]**. Since the Ni foil is flexible, $BaTiO_3$ films on Ni foils were flattened and fixed onto a glass slide using double

sided tape. The sample was put on the SE stage and aligned. The SE parameters, delta (Δ) and psi (Ψ), were collected at wavelengths from 250 to 750 nm with an increment of 5 nm at an incident angle of 70 degrees. For samples in which there was at least one absorber in the film stack, the incident light was linearly-polarized at 30°. At each wavelength, data from 50 turns of the analyzer were averaged. Background spectra (obtained with the PMT voltage set to the value during the measurement, but with the light beam blocked by a shutter) were also collected and subtracted from the measured data before calculating Δ and Ψ.

3.3.3 SE measurement with a compensator

It has been reported that the error in Δ for a rotating analyzer ellipsometry measurement is proportional to $1/\mathrm{Sin}\Delta$ **[7]**. Therefore, for a transparent film on a transparent substrate, the measured Δ is inaccurate because the value is near 0^o or 180^o for the whole measured spectrum **[6, 7]**. To resolve the problem, an achromatic compensator, or a quarter-wave plate, is used to add a 90^o phase shift to the incident beam. As a result, accurate measurements of Δ near 90^o can be obtained.

In this thesis, the compensator was used to measure Δ and Ψ of $BaTiO_3$ films on Al_2O_3 substrates. The polarizer was fixed at 45^o and the compensator was inserted between the polarizer and the sample to obtain a 90^o phase shift or circularly-polarized incident light. Two SE measurements were required. First, the true phase shift induced by the compensator was measured without any sample in the straight-through configuration (i.e. with a 90^o incident angle) for the entire wavelength range. Then, the

sample was aligned at a 70^{o} angle of incidence and another set of data was measured. The Δ and Ψ of the sample was calculated by **[6]**

$$\tan\Psi\, e^{i\Delta} = \frac{\tan\Psi_2\, e^{i\Delta_2}}{\tan\Psi_1\, e^{i\Delta_1}} \qquad 3.12$$

where the subscripts 1 and 2 refer to the straight-through measurement and the sample measurement, respectively. It is noted that the back surface of the Al_2O_3 was roughened using a diamond file and then painted with a carbon adhesive to remove reflection from the back surface of the substrate.

3.3.4 SE data modeling

Spectroscopic ellipsometry is an indirect characterization method because the measured data need to be modeled. First, a model is constructed assuming discrete layers of optically homogeneous materials parallel to the sample surface. Then, the thickness and optical properties of each layer were used to calculate Δ and Ψ as defined in equation 3.11. To minimize the number of parameters that must be fit, it is important to be able to input as much information as is known for the optical properties of the various layers in the sample.

For known materials, reference data of the optical properties were used if available. When the optical properties of the materials were not known, it was necessary to generate the data. Several approaches were utilized here. First, if the SE measurement is performed on an ideally smooth surface of a homogeneous material (i.e. a substrate),

the complex refractive index of the material can be directly inverted from the measured Δ and Ψ by **[6]**

$$N_1 = \tan\phi_0\left[1-\frac{4\rho\sin^2\phi_0}{(1+\rho)^2}\right]^{\frac{1}{2}} \qquad 3.13$$

where N_1 is the complex refractive index. However, generally, the sample surface is not perfectly smooth. Therefore, the complex refractive index obtained from the direct inversion without correcting for the real structure of the sample is not accurate. Since the surfaces of the Ni foils are very rough, this approach could not be employed. Instead, two sets of reference data of Ni were used (see section 5.1) Secondly, for unknown dielectric materials, a damped Sellmeier dispersion equation was used to describe the optical properties of the unknown phase **[8]**.

$$N^2(\lambda) = A_1 + \frac{A_2\lambda^2}{(\lambda^2 - A_3^2 - 2i\lambda A_4)} \qquad 3.14$$

where A_1 -A_4 are fitting constants. In all cases, A_1 was assigned to 1.

If any layer in the model had two constituents, consisting of f_A volume percent of phase A and f_B volume percent of phase B, Bruggeman effective medium theory was applied to calculate the optical properties of the layer **[5]**.

$$f_A\frac{\varepsilon_A-\varepsilon}{\varepsilon_A+2\varepsilon} + f_B\frac{\varepsilon_B-\varepsilon}{\varepsilon_B+2\varepsilon} = 0 \qquad 3.15$$

where ε is the complex dielectric function of the composite. This was used, for example, to calculate the net optical properties of low density layers as a mixture of the material and air.

Using one set of values for the optical properties and thickness of each layer, it is possible to calculate the Fresnel coefficients and the Δ and Ψ values for each wavelength. Once this is done, an unbiased estimator of the error in the fit was then calculated **[8]**:

$$\sigma = \frac{1}{m-p-1}\left[\sum_{i=1}^{m}\{(\cos\Delta_{i,exp} - \cos\Delta_{i,cal})^2 + (\tan\Psi_{i,exp} - \tan\Psi_{i,cal})^2\}\right]^{1/2} \qquad 3.16$$

where $\Delta_{i,exp}$, $\Psi_{i,exp}$ are the measured data; $\Delta_{I,cal}$, $\Psi_{i,cal}$ are the calculated values from the optical model at the i^{th} wavelength; p is the number of unknown variables in the model and m is the number of data points. A grid search in parameter space was then performed to obtain reasonable initial model parameters, where the values chosen were those that led to a minimum value for σ. Then, the program iterated around the best initial parameters, using a linear regression analysis. Once a best fit was achieved for a given model, a new model was attempted, and the process was repeated. For modeling of a $BaTiO_3$ film on a transparent substrate such as sapphire, the cosine of delta is very small, which underweights the importance of the Δ data. Thus, in this case, a difference of delta values was used to calculate sigma, rather than a difference in cosΔ **[6]**.

The best fit model was chosen based on the following criteria **[8]**:

1) A physically reasonable model

2) A small value of σ

3) Good agreement between experimental and calculated data

4) Reasonable values for the 90% confidence limits

5) Low values for the cross-correlation coefficients

3.4 Microstructural characterization

The microstructure and interface quality of $BaTiO_3$ films on Ni foils before and after a 1000^oC furnace anneal were observed in a transmission electron microscope (Philips 420) with a 120 keV tungsten source. This enabled observation of changes in grain size, grain morphology, and the presence of second phases in the films.

Cross-section TEM samples were prepared either by conventional polishing and ion milling or a focused ion beam technique. It was found that conventional polishing is useful for $BaTiO_3$/Ni foil samples after furnace annealing. However, RTA annealed films readily detached from the Ni foil during polishing, as shown in **Fig. 3.9**. Therefore, focused ion beam milling was utilized for such samples as it enables preparation of cross-section TEM samples without a mechanical polishing step **[9, 10]**.

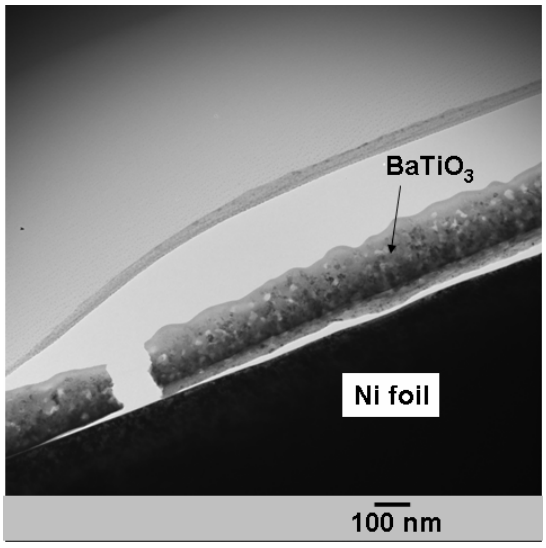

Fig. 3.9 Bright field TEM image showing $BaTiO_3$ film detached from the Ni foil due to conventional polishing preparation. This complicated studies of the interface quality.

3.4.1 Conventional polishing and ion milling

Preparation of cross-section TEM specimens from Si single crystal substrates was described by Bravman et al. **[11]**. In this work, Prof. Ian Reaney of Sheffield University was extremely helpful in suggesting appropriate ways of preparing TEM samples using polishing and milling. Since the Ni foils employed here are quite thin (25 μm) and hard to handle, buffers were used to support the foils for polishing. In this experiment, Si wafers were chosen as the mechanical supports due to their ready availability. Two pieces of approximately 3 mm square were cut from a $BaTiO_3$ film on Ni foil. Ni foils are easily bent; therefore, the pieces were flattened by gently pressing them between two glass slides. Two Si pieces of equivalent size were also cut and cleaned in acetone. To make a cross-section stack, the Si wafers and the samples were glued in the following order: Si/Ni-BT/BT-Ni/Si, using M-bond 610 adhesive (Vishay Micro-Measurements, Raleigh, NC 27611). Both the $BaTiO_3$ films and the polished side of the Si pieces faced the center of the stack. The stack was heated on a hotplate at 150^{o}C for 30 min to cure the glue. Pressure was applied to the stack to minimize the thickness of the glue layer and to avoid trapping air bubbles. Minimizing the thickness of the glue between the two $BaTiO_3$ surface also provided better uniformity during ion milling.

For the cross-section samples, the stack was mounted to a polishing stub using crystalbond. The sample was then gently polished with the polishing direction parallel to the interfaces. Polishing normal to the interface tended to break the stack and worsen the smear of the ductile Ni on top of the $BaTiO_3$. Both sides of the cross-section were polished using SiC paper #600 (16 μm grain) finished by #1200/4000 (5 μm grain) with a water rinse. To increase the mechanical stability of the stack during thinning, the first

completely polished side was glued onto a copper grid using M-bond adhesive before polishing the other side, as shown in **Fig. 3.10**. After thinning down to 40 μm thick, the sample on copper grid (3 mm in diameter) was cleaned in acetone and isopropanol. Then, it was further thinned using an EA Fishione Model 3000 ion mill operating at 5 kV and 5 mA. The inclination angle was set at 12 degrees and then 10 degrees to finish the ion milling.

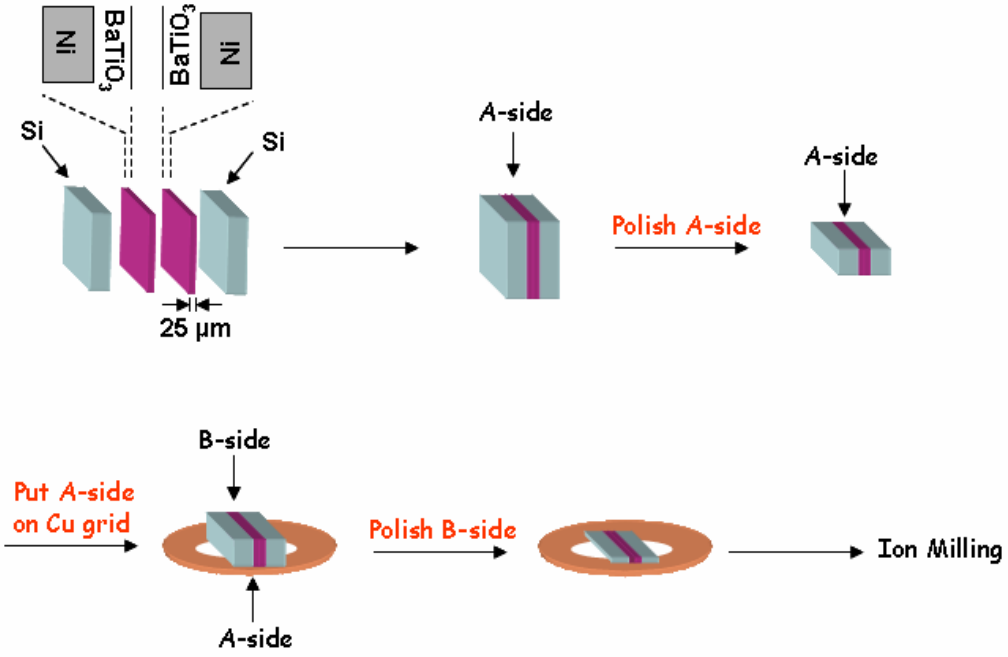

Fig. 3.10 Preparation of cross-sectional TEM samples by conventional polishing

3.4.2 Focused ion beam (FIB) TEM specimen preparation

Cross-sectional TEM samples of $BaTiO_3$ films on Ni foils were also prepared using an FEI Quanta 200 3D dual beam FIB (with the assistance of Trevor Clark). The system consists of an ion column (Ga), an electron column, a gas delivery system and a micromanipulator station. The system provides capability for ion milling, real-time monitoring of the sample and material (i.e. W) deposition. W deposition was performed using ion beam assisted chemical vapor deposition of chemical precursors.

In this experiment, the lift-out technique was used to prepare cross-sectional samples. The technique entails directly cutting a cross-sectional sample from the substrate and transferring it to a TEM grid where further thinning is performed. In this case, the $BaTiO_3$/Ni foil sample was coated with conductive carbon before mounting in the FIB to prevent charging as a result of ion/electron bombardment.

A 20 μm thick tungsten strip was first deposited on the desired region (20x2 μm^2), as shown in **Fig. 3.11**. This layer protects the $BaTiO_3$ surface underneath during subsequent ion milling. Then, the material surrounding the area of interest was wedge-cut free by ion milling. Then the piece of sample was lifted out and attached to a Cu grid (see **Fig. 3.12a**) using an omni probe. It is noted that an omni probe was attached to the sample by W deposition. On the Cu grid, the material at both sides along the interface of the sample was milled away until the width of the W strip was approximately 0.7-1 μm, as shown in **Fig. 3.12b**. The milling depth was just about half of the sample thickness, not all the way through the thickness. The material at either end and the bottom of the sample was retained to keep the sample mechanically stable. Then, the sample was further milled using an ion beam current from 300 to 100 pA, with alternate sample

tilting at 1 degree from the normal ion beam to enable milling on both sides. The final milling (100 pA) was finished when there was no W left in at least one region, as shown in **Fig. 3.12e**. It is noted that, as shown in **Fig. 3.12c-e**, one-third of the sample was thinned at a time.

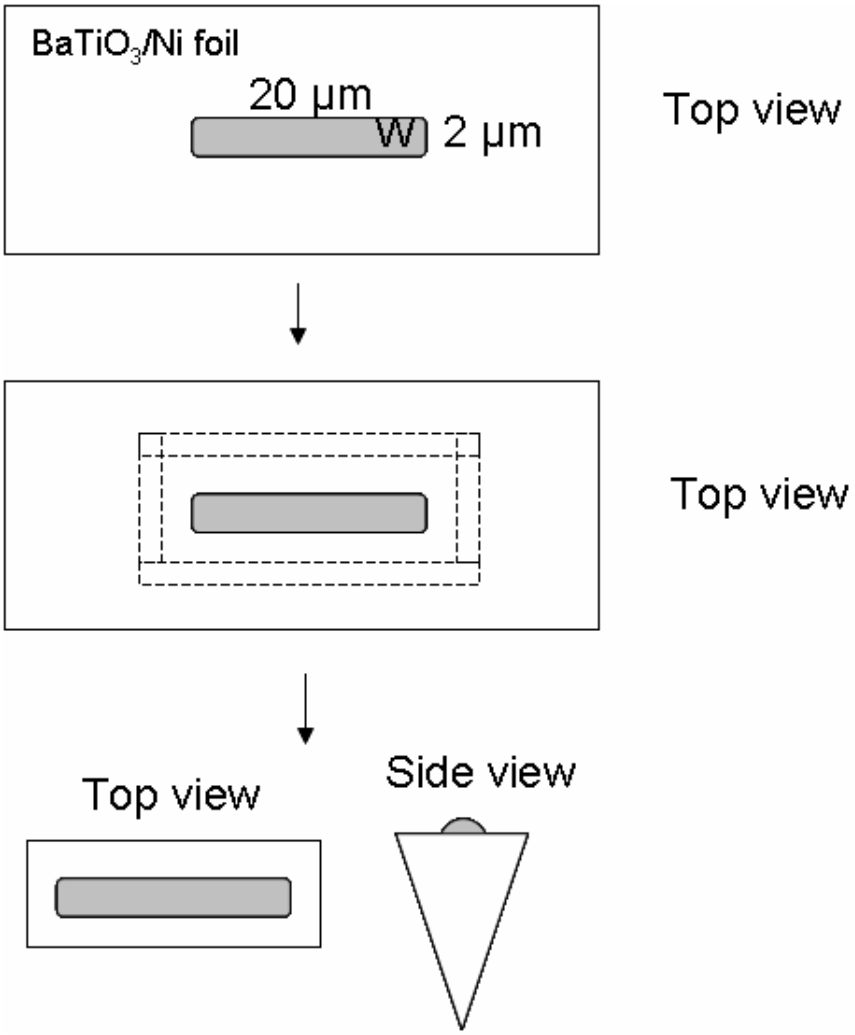

Fig. 3.11 Diagram of the FIB lift out process

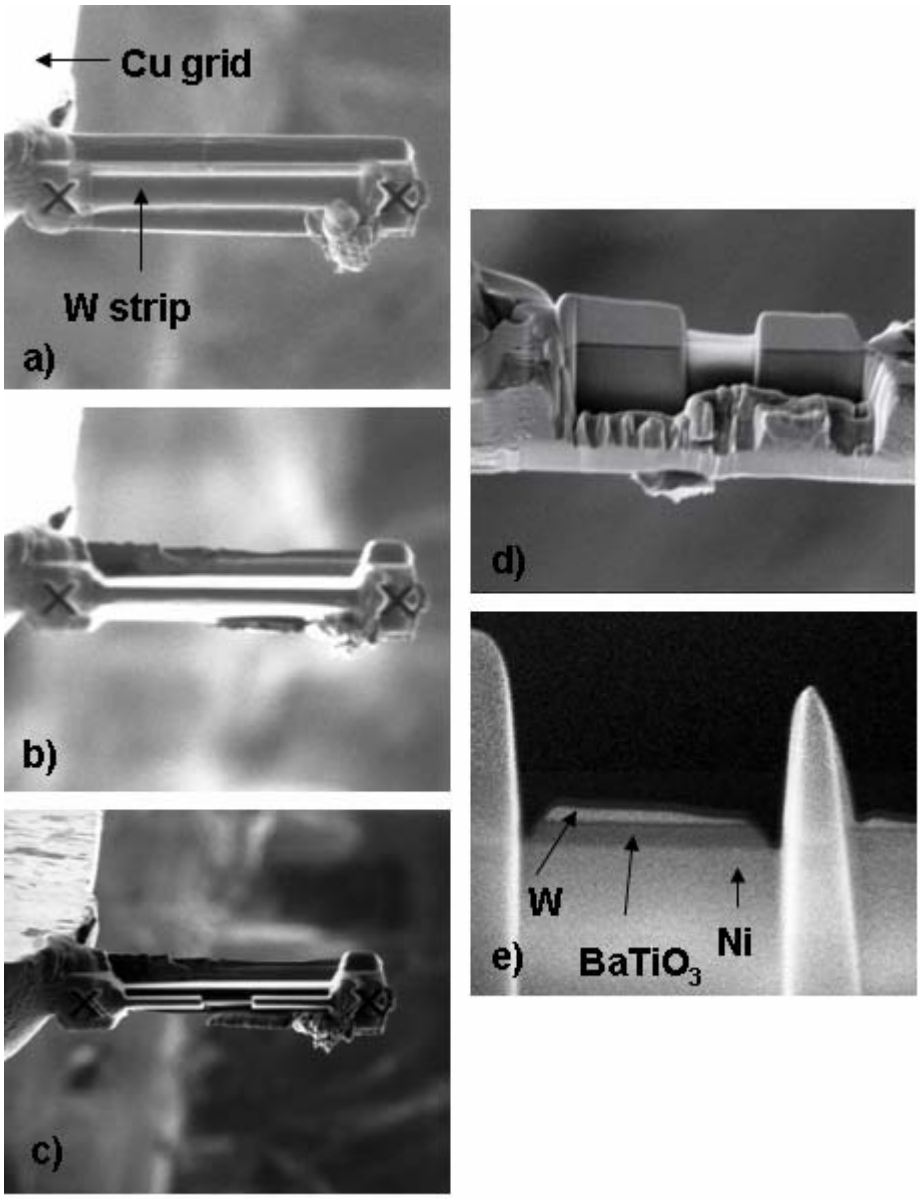

Fig. 3.12 (a – c) Series of top-view secondary ion images showing the thinning procedure for cross-sectional TEM sample by FIB a) a lift-out sample is attached to a Cu grid b) the sample is thinned by milling along the interface c) one-third of the sample is further thinned. (d-e) side view secondary electron images d) side view of c), e) final sample which is thinned until all of the W in a region disappears

3.4.3 Chemical analysis by electron energy loss spectroscopy (EELS)

A JEOL (2010F) transmission electron microscope with a field emission electron source combined with a Gatan Enfina parallel electron energy-loss spectrometer (EELS) was used for chemical analysis of $BaTiO_3$ films on Ni foils (with the assistance of Dr. Gaiying Yang). The microscope was operated at an accelerating voltage of 200 kV and the EELS spectra were acquired using diffraction mode. The resolution of the EELS spectra was 1.1 eV at the zero loss peak and the electron collection angle was 14 mrad.

Cross-sectional samples of furnace annealed $BaTiO_3$ film were prepared by conventional polishing, as described in section 3.4.1. Initial attempts to prepare the sample as described above resulted in very long milling times. To reduce the milling damage for the EELS specimens, the final thinning was performed on a cooling stage (using liquid N_2) in the EA Fishione Model 3000 ion mill. Nonetheless, it is possible that the long milling time may have influenced the oxidation state of the $BaTiO_3$ film.

3.5 Other characterization

3.5.1 Structural characterization

The crystallinity of the $BaTiO_3$ films on Ni foils was monitored routinely using a Scintag V X-ray diffractometer (Scintag Inc., Cupertino CA) with Cu Kα radiation. Data were collected from 20 to 60 ^{o} 2θ with a step size of 0.02^{o} and a 0.5 second acquisition time per step. A slow scan with a count time of 5 second was also used when a small amount of some phase, i.e. NiO, was expected.

3.5.2 Surface roughness

The surface roughness of Ni foil and $BaTiO_3$ films on Ni foil was determined by atomic force microscopy (Multimode IIIa, Digital Instruments), using tapping mode over

a scanning area of 5x5 μm or 3x3 μm, depending on feature size of the samples. The Si cantilever of 160 μm long was operated at its resonance frequency of 300 kHz.

3.5.3 Electrical measurement

The room temperature dielectric constant and loss tangent of the $BaTiO_3$ films were measured using a Hewlett-Packard 4192A impedance analyzer (Agilent Technology, Palo Alto, CA). The frequency dependence (0.1 kHz-1 MHz) was measured using an oscillating voltage of 0.03 V, using Ni and Pt as bottom and top electrodes, respectively. Capacitance as a function of voltage was measured by superimposing a small AC voltage (0.03 V) on DC Bias. Typical electrode size for these measurements is ~50 μm in diameter.

The temperature dependence of dielectric constant was measured using a Hewlett-Packard 4284A LCR meter. The measurement was performed at 0.03 V AC at different frequencies (0.1 kHz-1 MHz). The capacitance was measured over a temperature range of 25-200^{o}C with a heating rate of 2^{o}C/min. A typical electrode size for this measurement is ~150 μm in diameter.

The top electrode pattern was prepared by lift-off photolithography and Pt sputtering. First, LOR5A, used for better undercut control, was spin coated on the film at 4000 rpm for 45 s and then baked at 180^{o}C for 2 min. After the sample was cooled down, photoresist was spin coated on the top of film using the same spinning conditions and baked at 100^{o}C for 1 min. Then, the top of sample was exposed to UV (~300 W) through a photomask for 30 s. The photoresist and LOR pattern were developed using CD-26 (Shipley, Marlboro MA) and rinsed with deionized water. A 1000 Å thick Pt film was deposited using the W.M. Keck Smart Materials Integration Laboratory (Lesker CMS-18)

sputtering system. The substrate was held near room temperature and sputtering was done using an Ar pressure of 2.5 mTorr. The sample was dipped in acetone and then CD-26 to lift-off the unnecessary Pt, leaving only the Pt electrode pattern on the film surface.

References

[1] H. Nagata, S. W. Ko, E. Hong, C. A. Randall and S. Trolier-McKinstry, "Microcontact Printed $BaTiO_3$ and $LaNiO_3$ Thin Films for Capacitors," *Journal of the American Ceramic Society*, **89** [9], 2816-2821 (2006).

[2] G. Y. Yang, S. I. Lee, Z. J. Liu, C. J. Anthony, E. C. Dickey, Z. K. Liu and C. A. Randall, "Effect of Local Oxygen Activity on Ni-$BaTiO_3$ Interfacial Reactions," *Acta Materialia*, **54** [13], 3513-3523 (2006).

[3] D. V. Ragone, *Thermodynamics of Materials*. John Wiley & Sons Inc: New York, 1995; Vol. I.

[4] B. J. Gibbons. "Real-time Spectroscopic Ellipsometry and its Application to the Processing of $YBa_2C_3O_{7-\delta}$ Films by Molecular Beam Epitaxy," Ph.D. Thesis, The Pennsylvania State University, University Park, 1998.

[5] H. G. Tompkins and W. A. McGahan, *Spectroscopic Ellipsometry and Reflectometry: A User's Guide*. John Wiley & Son Inc: New York, 1999.

[6] P. Chindaudom. "Characterization of Inhomogeneous Transparent Thin Films on Transparent Substrates by Spectroscopic Ellipsometry," Ph.D. Thesis, The Pennsylvania State University, University Park, 1991.

[7] J. M. M. Denijs and A. Vansilfhout, "Systematic and Random Errors in Rotating-Analyzer Ellipsometry," *Journal of the Optical Society of America A-Optics Image Science and Vision*, **5** [6], 773-781 (1988).

[8] S. McKinstry. "Characterization of Ferroelectric Surfaces and Thin Films by Spectroscopic Ellipsometry," Ph.D. Thesis, The Pennsylvania State University, University Park, 1992.

[9] R. J. Young, P. D. Carleson, X. Da, T. Hunt and J. F. Walker, "High-Yield and High-Throughput TEM Sample Preparation Using Focused Ion Beam Automation," In Proceedings of 24th International Symposium for Testing and Failure Analysis, Dallas, Texas, Dallas, Texas, 1998; pp 329-336.

[10] R. M. Langford and A. K. Petford-Long, "Preparation of Transmission Electron Microscopy Cross-section Specimens Using Focused Ion Beam Milling," *Journal of Vacuum Science & Technology A: Vacuum, Surfaces, and Films*, **19** [5], 2186-2193 (2001).

[11] J. C. Bravman and R. Sinclair, "The Preparation of Cross-section Specimens for Transmission Electron Microscopy," *Journal of Electron Microscopy Technique*, **1** [1], 53-61 (1984).

Chapter 4

Cross-sectional Transmission Electron Microscopy Studies of $BaTiO_3$ Films on Ni Foils

This chapter details the use of transmission electron microscopy (TEM) to observe the microstructure and interface quality of $BaTiO_3$ films on Ni foil after heat treatment in either the RTA or the reducing furnace. The $BaTiO_3$ films used in these experiments were obtained from 0.1 M methanol-based $BaTiO_3$ solutions. The deposition method was described in section 3.1.2. Two layers were deposited on the pre-annealed Ni foil; each layer was dried and pyrolyzed. After deposition, the film was annealed in an RTA at temperatures of 700-750^{o}C. Another two layers were deposited and the drying, pyrolysis and RTA annealing were repeated until 8 layers were processed. Then, the 8 layer film was annealed in the reducing furnace at 1000^{o}C and re-oxidized at 600^{o}C. Either focused ion beam (FIB) milling or a conventional polishing/milling method was used to prepare cross-sectional TEM samples, as described in section 3.4. A discussion of damage due to FIB milling of an RTA annealed $BaTiO_3$ films is in section 4.1. The microstructures of RTA'd films and furnace annealed films are presented in sections 4.2.1 and 4.2.2, respectively.

4.1 Damage Artifacts Produced by FIB Milling

As described in section 3.4, cross-sectional TEM samples of low temperature annealed (RTA) $BaTiO_3$ films could be prepared without the films detaching from the Ni

foil by FIB milling. It is well-known that the rastered Ga^+ ion beam used in FIB milling creates several forms of damage (i.e. ion implantation, amorphization and re-deposition of milled materials) on the machined surface that can complicate TEM studies, including imaging, structural and chemical analysis **[1-4]**. Therefore, it is necessary to understand the nature and cause of the damage both to minimize damage issues in a specific sample and to avoid inaccurate TEM study and analysis.

Fig. 4.1a shows a large, uniform, electron-transparent area in a cross-section of a $BaTiO_3$ film on Ni foil prepared by FIB. The cross-section shows the Ni foil, $BaTiO_3$, conductive C and a W layer (which was deposited in the FIB before cutting and thinning the TEM sample). In the figure, it is noticeable that the $BaTiO_3$ film exhibits discrete layers of crystallized grains. The layers are visible through the film thickness in areas where the thick W protective layer is intact. **Fig. 4.1b** shows an undamaged film cross-section. In contrast, where the W layer is thinner, the $BaTiO_3$ grain structure at the top of the film is difficult to resolve. The disappearance of this feature is believed to be a result of damage induced by ion beam milling. These results suggest that the damage occurs mainly during final thinning, rather than during deposition of W layer. For these images, the final thinning conditions used a 30 keV, 100 pA beam. Although this current is already low, it is possible that the ion energy could be reduced to 5 – 10 keV to further reduce the damage. Alternatively, it might be possible to minimize the impact of ion-bombardment induced damage by finishing sample preparation using an Ar^+ ion beam.

There are no reports available on the mechanism for damage in similar samples. Nonetheless, the loss of the grain structure suggests that perhaps amorphization of the surface is responsible **[5, 6]**.

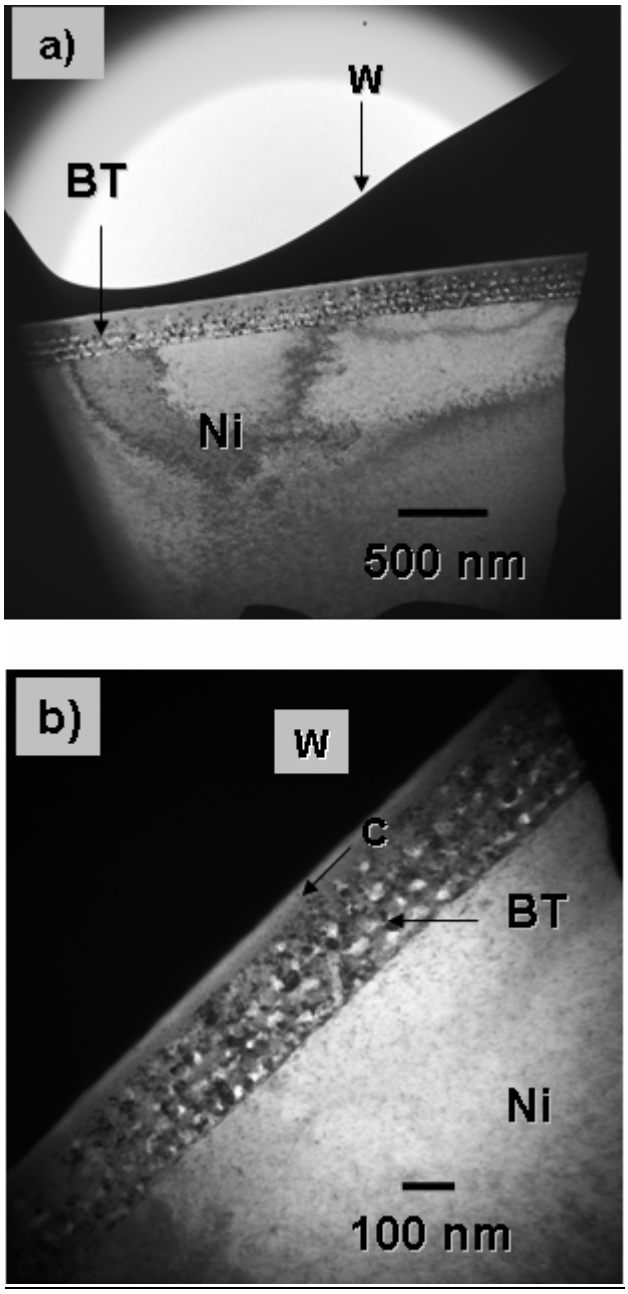

Fig. 4.1 TEM cross-sectional micrograph of 750^{o}C annealed $BaTiO_3$ films on Ni foil showing a) partial film damage by ion milling at the top of the film and b) discrete crystallization layers in a region where the film is thick and a large amount of W is still intact. BT = $BaTiO_3$

4.2 Microstructure

4.2.1 RTA annealed $BaTiO_3$ films

Discrete crystallization layers are apparent in the $BaTiO_3$ films annealed at 700^{o}C and 750^{o}C. There is no significant difference in grain size across the film thickness, as clearly shown in the undamaged area in **Fig. 4.1b**. The high magnification bright-field TEM micrographs in **Fig. 4.2a and b** show the microstructure of the $BaTiO_3$ films on Ni foil after RTA annealing at 700^{o}C and 750^{o}C, respectively. It is noted that an additional Au layer was deposited between the $BaTiO_3$ and C coat in order to provide better contrast of the film surface. (Although Au is conductive, it is easily milled by Ga^+ ions. Therefore, the C layer is necessary for charging protection.) A $BaTiO_3$ thickness of approximately 200 nm was achieved with 8 coatings and 4 RTA anneals, yielding 25 nm for each layer of deposition. Although the TEM samples were partially damaged, it is shown that both RTA'd $BaTiO_3$ films have equiaxed polycrystalline grain structures. The grain size of the $BaTiO_3$ film annealed at 700^{o}C varied from 5 to 20 nm with an average grain size of 12 nm. On increasing the RTA temperature to 750^{o}C, the average grain size slightly increases to 18 nm and the grain size is between 10 and 30 nm. Both films contain a few nano-size (<10 nm) pores and no cracking was observed. The $BaTiO_3$ / Ni foil interfaces in samples annealed at 700^o and 750^{o}C show no evidence of any interfacial layer such as NiO.

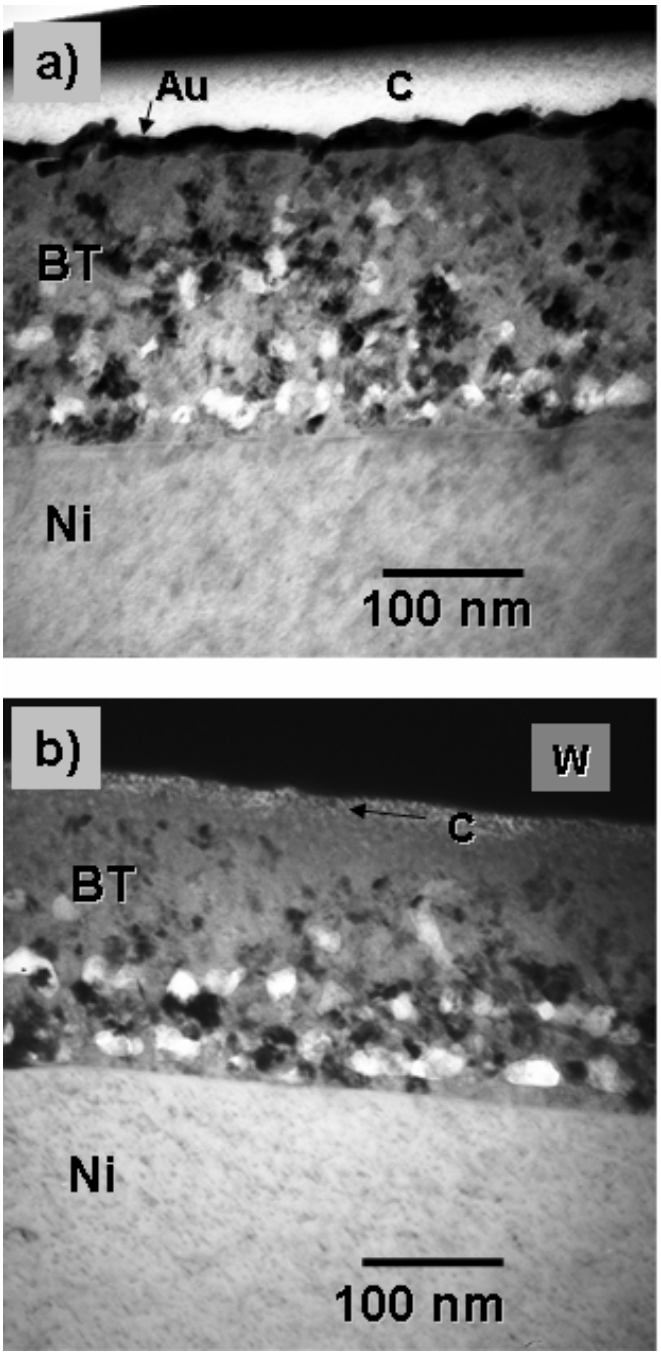

Fig. 4.2 TEM bright-field micrograph of microstructure and interface of $BaTiO_3$ films on Ni foils annealed on RTA at a) 700^{o}C and b) 750^{o}C

The grain size of the chemical solution deposited based-$BaTiO_3$ films in this work is compared to previous reports in **Table 4.1**. In the table, the substrate type and heat treatment conditions of the films is included. The morphology of most of the films was reported to be equiaxed; it is noted if the authors stated otherwise. The grain size range of 5-30 nm of the RTA'd films at 700^{o}C and 750^{o}C in this experiment was small. Neglecting the difference in precursor chemistry and substrate materials, this small grain size is reasonable, compared to the reported grain size of 15-20 nm of $(Ba,Sr)TiO_3$ films on Pt/Si substrates prepared using similar conditions **[7]**. A larger grain size (20-60 nm) was reported for films that were annealed at 700^o or 750^{o}C for longer times (0.5-1 hr) **[8-10]**.

The appearance of consecutive layers of $BaTiO_3$ grains confirmed that crystallization occurred during each RTA annealing at both 700^{o}C and 750^{o}C. Perovskite $BaTiO_3$ was also apparent in electron diffraction patterns of the RTA'd films. **Fig. 4.3** shows sample areas and the corresponding diffraction patterns of $BaTiO_3$ films on Ni foils. **Fig. 4.3a-b** shows a film crystallized using an RTA temperature of 700^{o}C. A 0.4 μm aperture covering only the Ni and $BaTiO_3$ was used to avoid diffraction from Au or C. Only $BaTiO_3$ rings appear, implying the observed area did not have NiO at the interface. Only two diffraction spots were seen for the Ni substrate. **Fig. 4.3c-d** shows the results for a furnace annealed film. A larger number of more continuous rings were observed because an aperture of 0.8 μm was used to cover more film area. Similar to the RTA'd film, only perovskite $BaTiO_3$ rings appear and there are two Ni spots.

AFM was used to confirm the surface morphology of the films, as shown in **Fig. 4.4**. In AFM scans over a 0.5 x 0.5 μm area for $BaTiO_3$ films annealed at 700^{o}C and

750^{o}C (See **Fig. 4.4a**), a somewhat larger feature size is observed, compared to that obtained from the cross-sectional TEM sample. This discrepancy is believed to be due to detection of clusters of $BaTiO_3$ grains, rather than primary grains, by AFM.

The equiaxed, polycrystalline structure of the $BaTiO_3$ films suggests bulk nucleation in this work. However, it has been shown elsewhere that the substrate materials and preparation conditions can also affect the microstructure of the films. Sedlar et al. showed isolated large grains in a Ce-doped BST film at the film/Pt-Si interface. In that case, the grain size decreased from the interface to the film surface because of multiple coating and annealing at 750^{o}C **[7]**. Gust et al. observed that heterogeneous nucleation at the film/Pt-Si interface competes with major bulk nucleation due to the small lattice mismatch between the $BaTiO_3$ film and Pt (~3%) **[9]**. Using Pt-Si substrates, chemical solution deposited $BaTiO_3$ (or $SrTiO_3$) films with columnar structure can be achieved by controlling film thickness and performing multiple coating and annealing. It was shown that depositing very thin layers (10-20 nm) and annealing after each layer can induce nucleation at the bottom surface and local epitaxial growth within each columnar grain. This effectively suppresses bulk nucleation **[11-13]**.

Table 4.1 Reported grain size and average grain size (in parentheses) of $BaTiO_3$ – based films prepared by various groups under a variety of different conditions

Film/substrate	Annealing condition		Grain size and (avg grain size) (nm)	Total Thick-ness (nm)	Ref
	T(^{o}C)/Time	Atmosphere			
This work: $BaTiO_3$/Ni foil	700^{o}C, 1 min* 750^{o}C, 1 min* 1000^{o}C, 1 hr	N_2 N_2 10^{-16}	5-20 (12) 10-30 (18) 24-75 (42)	200 200 200	-
$BaTiO_3$/Pt-Si	700^{o}C, 30 min	O_2	20-60 (40)	250	**[8]**
(Ba,Sr)TiO_3/Pt-Si	700, 1 h	air	50	400	**[10]**
Ce-(Ba,Sr)TiO_3/ Pt-Si	750^{o}C, 2 min*	n/a	(15-20)	200	**[7]**
$BaTiO_3$/Si	750^{o}C, 1 hr	O_2	20-60	300	**[9]**
(Ba,Sr)TiO_3/Ni foil	900^{o}C, 1 hr 900^{o}C, 1 hr*	10^{-18} 10^{-18}	30-35** 40-50**	400 400	**[14]**
$BaTiO_3$/Cu foil	900^{o}C, 30 min	10^{-9}	100-300 (200)	600	**[15]**

* Multiple annealing
** No evidence of grain morphology reported

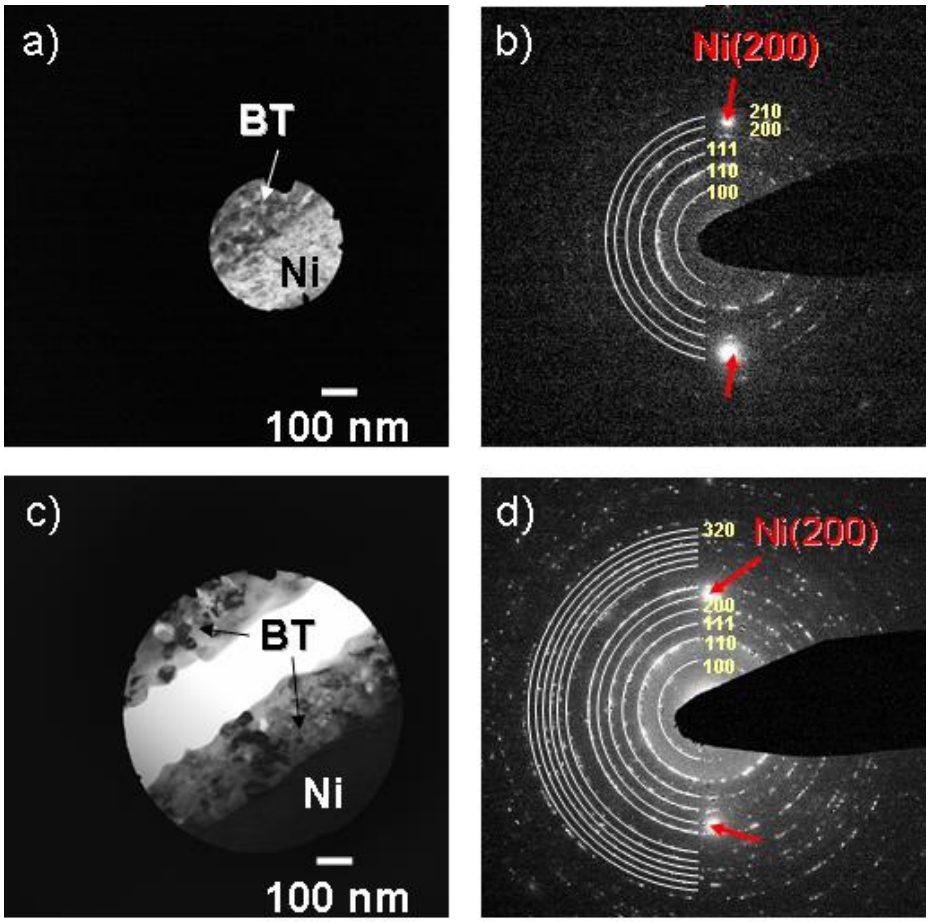

Fig. 4.3 Investigated area and corresponding electron diffraction patterns of $BaTiO_3$ films on Ni foils: a-b) are for a 700 RTA'd annealed film, c-d) are from a furnace annealed film (1000^{o}C)

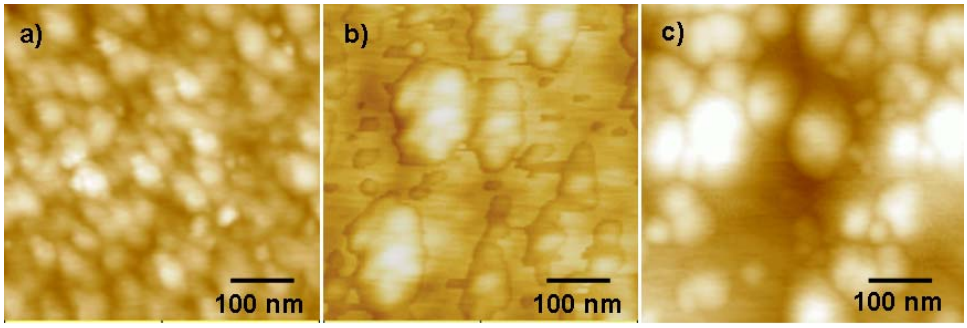

Fig. 4.4 AFM scan area 0.5 x 0.5 um of $BaTiO_3$ films annealed at a) 700^{o}C (RTA), b) 750^{o}C (RTA) and c) 1000^{o}C

In this experiment, the equiaxed morphology in films annealed at 700^{o}C and 750^{o}C suggested that the nucleation occurs throughout the films. The grain size was uniformly distributed across the film thickness, implying that repetition of the RTA annealing induced crystallization of newly deposited layers, but did not cause considerable grain growth of the previously-crystallized $BaTiO_3$. It is also possible that the large lattice mismatch of $BaTiO_3$ and Ni (~13% **[16]**) may not cause preferential nucleation at the film/substrate interface.

No clear interfacial layer between the $BaTiO_3$ films and Ni foil was observed for films annealed at 700^{o}C or 750^{o}C, indicating that covering the Ni foil with at least ~ 50 nm of amorphous $BaTiO_3$ film (first 2 layers) and using N_2 flow during both film pyrolysis at 350^{o}C and RTA annealing 700^{o}C or 750^{o}C prohibited oxidation of the underlying Ni foil. It is possible that pyrolysis in the nitrogen ambient did not allow complete removal of carbon, so that the local oxygen partial pressure during the RTA step was lower than that of the ambient. This will be discussed further in section 5.3.2. Finally, it is noted that the observed cross-sectional $BaTiO_3$ films are on a single grain of Ni. Therefore, no comment can be made about the presence of an oxide layer (i.e. of contaminants in the Ni foil, or due to NiO formation) at the junction of the $BaTiO_3$ film and a grain boundary in the Ni substrate.

4.2.2 Furnace annealed $BaTiO_3$ films

The $BaTiO_3$ film, which was RTA annealed at 700^{o}C, was crystallized in a tube furnace at 1000^{o}C at 10^{-16} atm pO_2. This pO_2 is below that for the Ni/NiO equilibrium,

so NiO is not expected to be thermodynamically stable. Subsequently, the sample was re-oxidized at 600^{o}C at 10^{-6} atm pO_2.

The cross-section of the furnace annealed film was prepared by mechanical polishing and Ar^{+} ion milling. **Fig. 4.5a** shows a TEM cross-section showing two pieces of the same film. It is noticed that there is some variation in grain size and thickness between the two pieces of films. The film surface is rough due to grain growth at high temperature. As shown in **Fig. 4.5a** and **b**, the films exhibit polycrystalline, equiaxed grains. The average grain size of the furnace annealed film is 42 nm, and the grain size ranged from 24 to 75 nm (from the piece with the larger overall grain size). The grain size distribution is similar to that in the film before furnace annealing, implying that no abnormal grain growth occurs. The film contains 5-6 grains across a film thickness of ~200 nm. There are a few isolated voids (with a size on the order of the grain size) distributed in the film. The voids may be from either from porosity or damage due to (Ar^{+}) ion milling. There is no interfacial layer between $BaTiO_3$ film and Ni foil, indicating that neither the heat-treatment, not the re-oxidation caused extensive Ni oxidation.

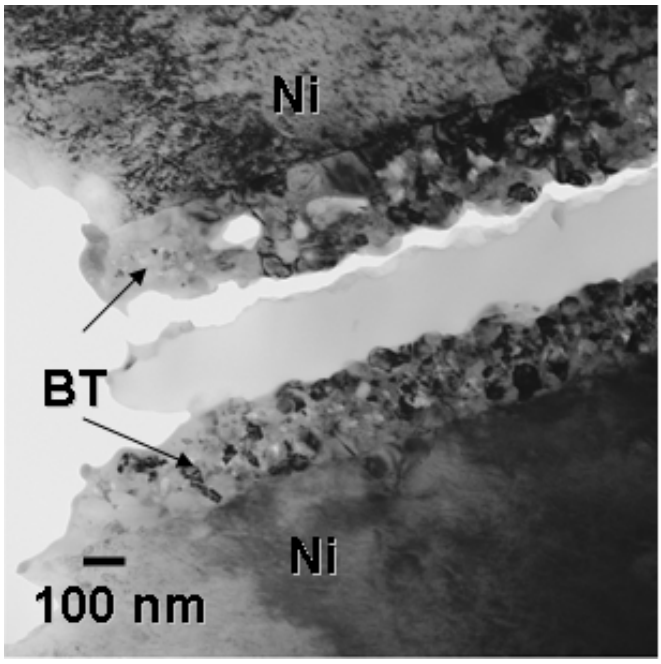

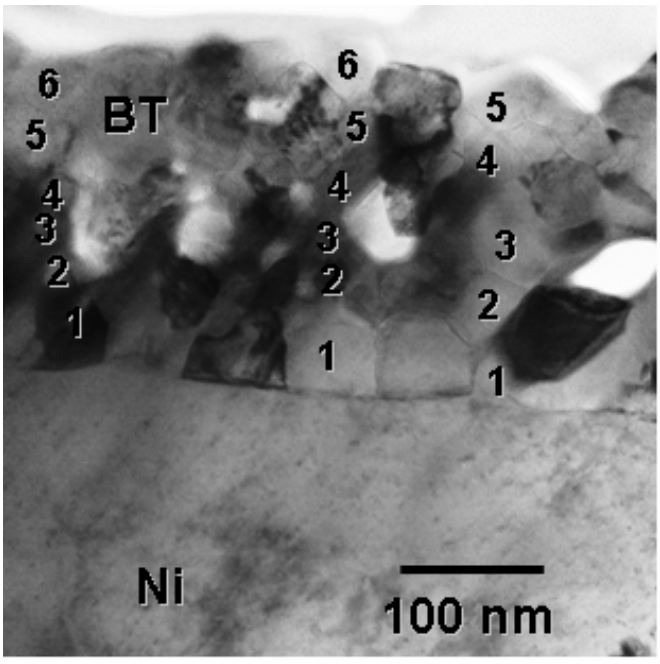

Fig. 4.5 Bright-field micrographs of the microstructure and interface of $BaTiO_3$ films on Ni foils annealed in furnace 1000^{o}C. (High magnification figure is courtesy of Dr. Ian Reaney)

The change in microstructure of the furnace annealed $BaTiO_3$ film was expected to be dominated by the 1000^oC step since the re-oxidation was performed at much lower temperature (600^oC), where the cation mobility is low **[17, 18]**. However, considering the high pO_2 used at 600^oC, the re-oxidation step can affect the interface quality and oxygen content in $BaTiO_3$ lattice, which will be discussed in section 4.3.

Compared to the RTA annealed film in **Fig. 4.2a**, the furnace annealed $BaTiO_3$ film has a much larger average grain size (42 nm) due to grain growth at higher temperature. Again, the AFM image in **Fig. 4.3c** showed a much larger cluster size.

There are few reports of preparing $BaTiO_3$ films by CSD method at temperatures higher than 800^oC, as shown in **Table 4.1**. The grain size of the furnace annealed $BaTiO_3$ film in this experiment is comparable to that reported in Dawley et al.'s work where BST films on Ni foil were prepared at 900^oC in a similar reducing atmosphere **[14]**. In contrast, the grain size of the furnace annealed film here is much smaller than that of $BaTiO_3$ films on Cu foil, which consists of two equiaxed grains of 300 nm size across the film thickness, as shown in Ihlefeld et al.'s work **[15]**. Since the solution chemistry of the two films was similar, the differences may be due to the annealing conditions. In this experiment, the $BaTiO_3$ film was pre-crystallized in an RTA at 700^oC before being subjected to the furnace anneal (1000^oC), while in Ihlefeld's work, the $BaTiO_3$ was crystallized once at 900^oC. In addition, the pO_2 used for annealing $BaTiO_3$ films on Ni foils (10^{-16} atm) is much lower than that of Cu foil (10^{-9} atm). It has been reported that prior H_2 heat treatments of $BaTiO_3$ ceramics can freeze abnormal grain growth in subsequent air sintering **[19, 20]**. Also, Polotai et al. showed that average grain size of a $BaTiO_3$ ceramic strongly decreased from 296 to 137 nm as the pO_2 during sintering

decreased from 10^{-1} to 10^{-19} atm **[21]**. Thus, it is speculated that the difference in grain size for films on Cu and Ni can be attributed to a combination of the number of crystallized grains before the high temperature furnace annealing and the effect of the pO_2 atmosphere. Since the RTA'd $BaTiO_3$ film contains a high concentration of small grains, grain impingement during growth may limit the final grain size during furnace annealing.

Although a columnar structure was reported to improve the dielectric properties of $BaTiO_3$ - based films **[12, 22, 23]**, equiaxed grains are necessary to limit oxygen vacancy mobility in base-metal MLCCS. Many studies have shown that the dc insulation resistance degradation originates from electromigration of oxygen vacancies in the perovskite lattice **[11, 24-27]**. In equiaxed structures, the grain boundaries parallel to the interface provide Schottky barriers for migration of the oxygen vacancies created by the reducing atmosphere processing. Thus, it is encouraging that there are multiple grains across the thickness of a quarter micron thick CSD-derived layers.

4.3 Chemical analysis and oxygen nonstoichiometry

Oxygen nonstoichiometry is very important to the electrical properties and reliability of $BaTiO_3$ capacitors. In an attempt to investigate this parameter, furnace annealed (re-oxidized) $BaTiO_3$ films on Ni foils were investigated by electron energy loss spectroscopy (EELS) in a transmission electron microscope. The data were obtained with the help of Dr. Gaiying Yang. The energy loss peaks for Ba, Ti and O were observed using the Ba $M_{4,5}$ (781 eV), Ti $L_{2,3}$ (455.5 eV) and O K edges (532 eV), respectively. Since the films were processed at low pO_2, it is also of interest whether

there is any residual C in the film. The C K edge is at 283.8 eV. In this experiment, all EELS spectra were calibrated (to shift the peaks to the correct position) by using the onset of the O K edge. High resolution TEM imaging was used to confirm any contamination on the surface of the thin specimen.

Fig. 4.6 shows a cross-section of a bright field image of $BaTiO_3$ on Ni foil. EELS analysis with an electron beam size of ~ 10 nm was randomly performed on 4-5 grains of the furnace annealed $BaTiO_3$ film on Ni foil. All grains show similar EELS spectra, which consist of a strong C K edge peak associated with the existence of Ba $M_{4,5}$, Ti $L_{2,3}$ and O K edges, as shown in **Fig. 4.7**. EELS spectra of the Ni foil show only the Ni $L_{2,3}$ edge (854 eV) without the C K edge. The result suggested that C really existed in the $BaTiO_3$ film and was not solely surface contamination.

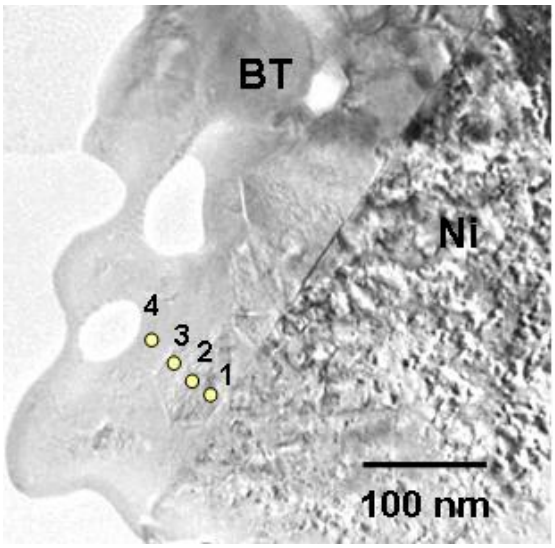

Fig. 4.6 Cross-sectional bright field image of $BaTiO_3$ film on Ni foil (Courtesy of Dr. Gaiying Yang). Positions for EELS analysis are marked.

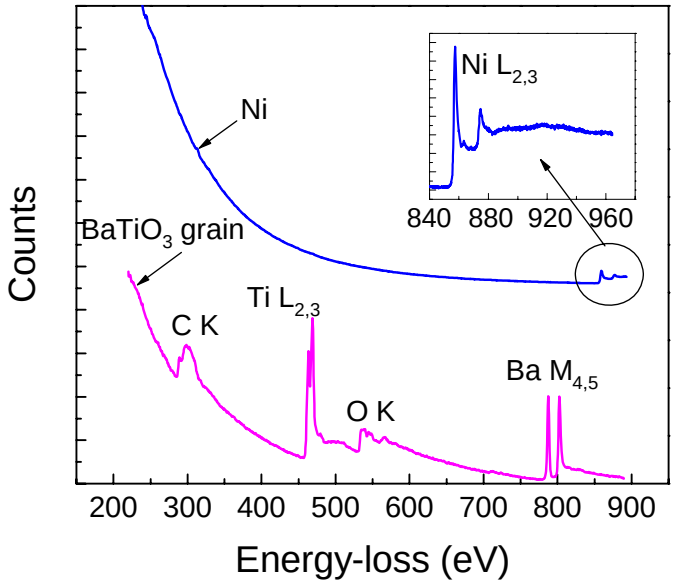

Fig. 4.7 EELS spectra of $BaTiO_3$ grain and Ni foil, showing existence of C in the $BaTiO_3$ (Data courtesy of Dr. Gaiying Yang)

Oxygen non-stoichiometry is usually determined using the $Ti_{2,3}$ and O K edges. A reference EELS spectrum of an air sintered, precious metal electrode (PME) MLCC (**Fig. 4.8b)** shows the fine structure in the Ti $L_{2,3}$ and O K edges for oxygen-stoichiometric dielectrics. The splitting of the Ti L_3 edge (lower energy) into e_g and t_{2g} features and the high intensity of the O K edge peak series are characteristic of a low concentration of oxygen vacancies in the PME dielectrics. Of interest for this discussion is the clarity of the splitting in the Ti $L_{2,3}$ edge.

EELS analysis on a furnace annealed $BaTiO_3$ film on Ni foil was performed at 3-4 areas as a function of distance from Ni electrode. **Fig. 4.6** is marked with 4 spots where the EELS spectra were acquired. EELS spectra for the C K, Ti $L_{2,3}$, O K and Ba $M_{4,5}$ edges were first collected from each spot using an energy dispersion of 0.5 eV/channel to cover the broad range of C, Ti, O and Ba edge positions. Finer resolution of the Ti $L_{2,3}$ and O K edges was obtained by re-measuring each spot with an energy dispersion of 0.1 eV/channel.

Fig. 4.8a shows broad range EELS spectra from the 4 spots in **Fig. 4.6**. It was found that, in this area of the $BaTiO_3$ film, every spot contains at least some C. The lowest carbon concentrations were observed near the electrode and a grain boundary. Oxygen diffusion is faster along grain boundaries in $BaTiO_3$, which would facilitate carbon oxidation from those regions. The EELS spectrum near the Ni foil (Point 1) show no splitting of e_g and t_{2g} peaks and a lower intensity of the O K edge, implying a partial reduction of the Ti oxidation state from 4+ to 3+ which is usually associated with low oxygen content. The spectrum at Point 4 shows almost fully oxidized Ti, similar to the PME dielectric. The fact that near- stoichiometric $BaTiO_3$ was observed in some regions

of the sample suggests that the reduced regions observed elsewhere were not simply the product of ion milling.

Two more areas were also examined. A lower amount of C was found near the electrode in both areas. In one of these, nearly stoichiometric $BaTiO_3$ was found near the Ni foil and the oxygen content slightly decreased as a function of distance from Ni foil. In another area, nearly stoichiometric $BaTiO_3$ was found at all depths. The existence of C is probably a consequence of incomplete removal of C from the organic precursors in the film. This is reasonable given the low pO_2 conditions used. The variation in oxygen content as a function of distance from Ni foil was thus variable in this re-oxidized film. It is suggested that this parameter be investigated more thoroughly by examining films after the high temperature heat treatment, but prior to re-oxidation.

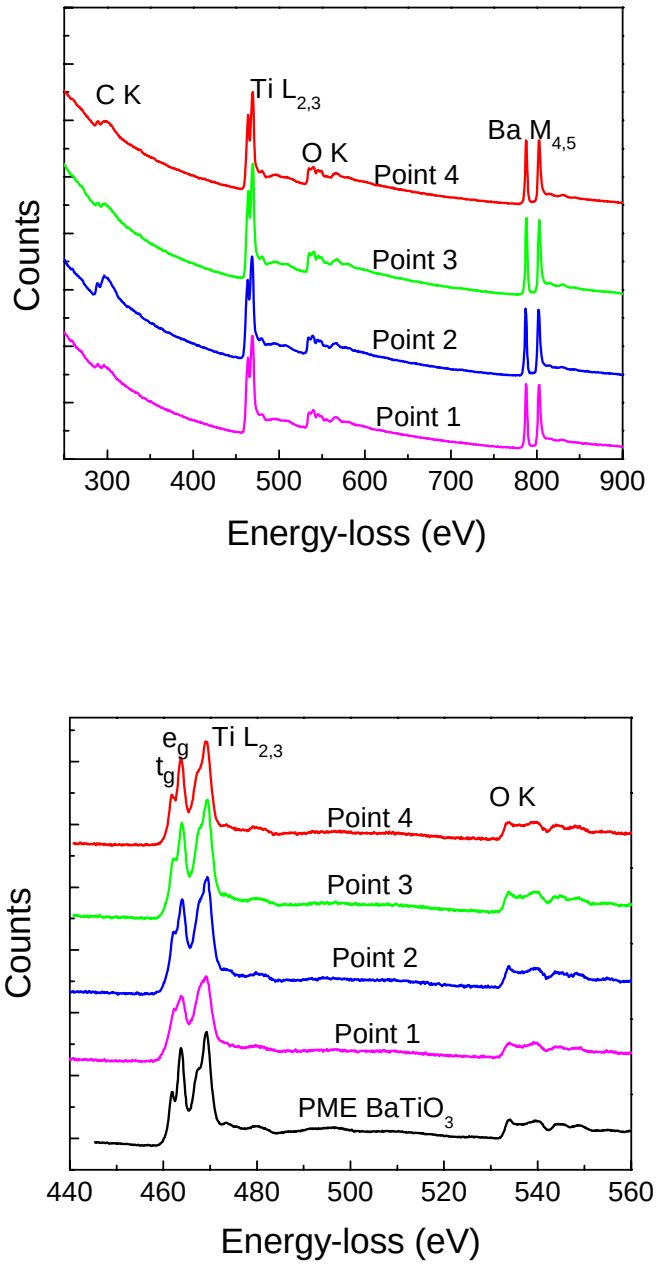

Fig. 4.8 EELS spectra collected from $BaTiO_3$ film as a function of distance from Ni foil a) broad range spectra b) resolved spectra of the fine structure of Ti $L_{2,3}$ and O K edges including that of PME $BaTiO_3$ (Data courtesy of Dr. Gaiying Yang)

HRTEM was performed to investigate the $BaTiO_3$ / Ni interface, as shown in **Fig. 4.9**. The clear atomic arrangement in the $BaTiO_3$ confirms that there is no contamination on the sample surface or damage due to sample preparation. Atomic steps were observed along the Ni foil surface. The Moiré fringes in the Ni region are not fully understood, however it is suspected that the fringes are due to absorbed oxygen on the surface of Ni foil **[28]**.

The Ni foil surface shows some image contrast at the top ~ 5-8 nm. **Fig. 4.10** shows representative EELS spectra obtained from deeper in the Ni region and this interfacial layer. The Ni $L_{2,3}$ edge confirms that in both cases Ni is in a metallic state, not an oxide **[29]**. Thus, the associated O K edge is due to O absorbed on the Ni surface. The interfacial layer shows primarily metallic Ni $L_{2,3}$ with a small Ba $M_{4,5}$ edge and no O K edge. The result suggested the interfacial layer is a Ni-Ba alloy. EELS spectra of the interfacial layer and Ni region were confirmed at 3-5 spots and the same results were obtained. A wider view of the interface showing this is given in **Fig. 4.11**. It is noted that no NiO is observed.

Oxygen non-stoichiometry and the internal dielectric / electrode interfaces in $BaTiO_3$ MLCC with Ni electrodes were studied by Yang et al. **[24, 25, 28]**. It was shown that the oxygen content in co-fired $BaTiO_3$ increases as a function of distance from the Ni electrode after the sintering step, but becomes more spatially homogeneous after re-oxidation. They also discovered the presence of a Ni-Ti-Ba alloy layer (4-15 nm thick) between the $BaTiO_3$ and the Ni in commercial MLCCs **[28]**. It was found that the metallic alloy layer develops during the co-firing step (1300^oC, 10^{-10} atm pO_2) and survives the re-oxidation step (800^oC, 10^{-8} atm pO_2). Carbon residue was proved to be

the cause of the metallic alloy interface layer and the local variation of oxygen content in the co-fired $BaTiO_3$. Belated decomposition of the organics, especially C, from the Ni paste may rob oxygen from the $BaTiO_3$ lattice, resulting in oxygen vacancies near the electrode **[24]**.

It is believed that the Ni-Ba layer observed in the films occured during the high temperature heat treatment and was retained through re-oxidation. It is important to note that for all of the firing conditions employed, BaO, rather than Ba is thermodynamically stable. This implies that there must have been a strongly reducing local environment to produce metallic Ba. It was suggested by Yang et al. **[28]** that such a highly reducing atmosphere could be induced by local CO/CO_2 reactions with Ni as a catalyst. The C in the films could be from incomplete organic removal at the low oxygen partial pressure employed during the RTA step. It is interesting that the alloy composition seen in the thin films does not apparently show any Ti. This could be a result of the lower process temperatures used for thin film firing, than for bulk ceramics.

The origin of the interfacial alloy is not well understood. One possibility is that a Ni-Ba liquid phase develops due to the existence of low melting temperature eutectics on the phase diagram (See Figure 4.12). Ba-containing crystallites could precipitate from the liquid phase on to the Ni (FCC) surface, producing a structure-matched FCC Ba-rich phase. This would explain the observation that the Ni-Ba alloy structure is coherent with that of the Ni.

It will be important in the future to determine the alloy composition more quantitatively, and to estimate its impact on the Schottky barrier layer at the film/foil interface. Further study of organic removal in low pO_2 will be discussed more in section

5.3.2. The observed spatial nonuniformity in the C content may be linked to the local variations in the Ti^{3+}/Ti^{4+} ratio.

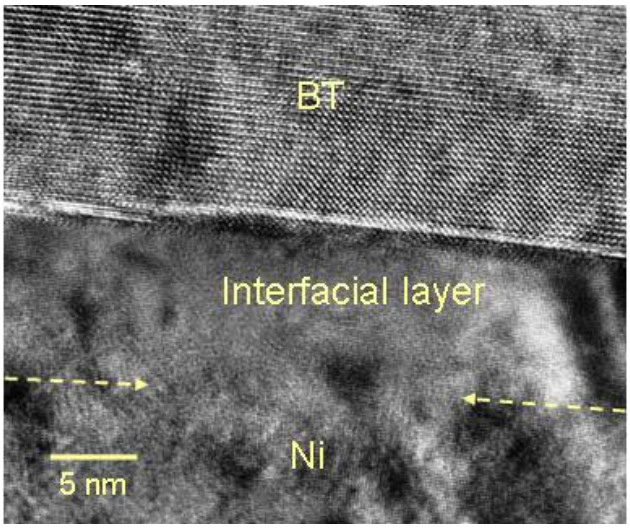

Fig. 4.9 HRTEM image of furnace annealed $BaTiO_3$ film/ Ni foil interface (Data courtesy of Dr. Gaiying Yang)

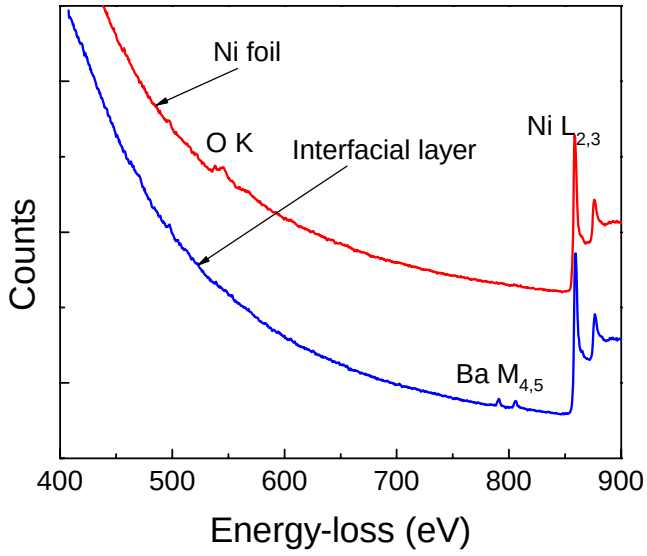

Fig. 4.10 EELS spectra collected from Ni region and interfacial layer between $BaTiO_3$ and Ni (Data courtesy of Dr. Gaiying Yang)

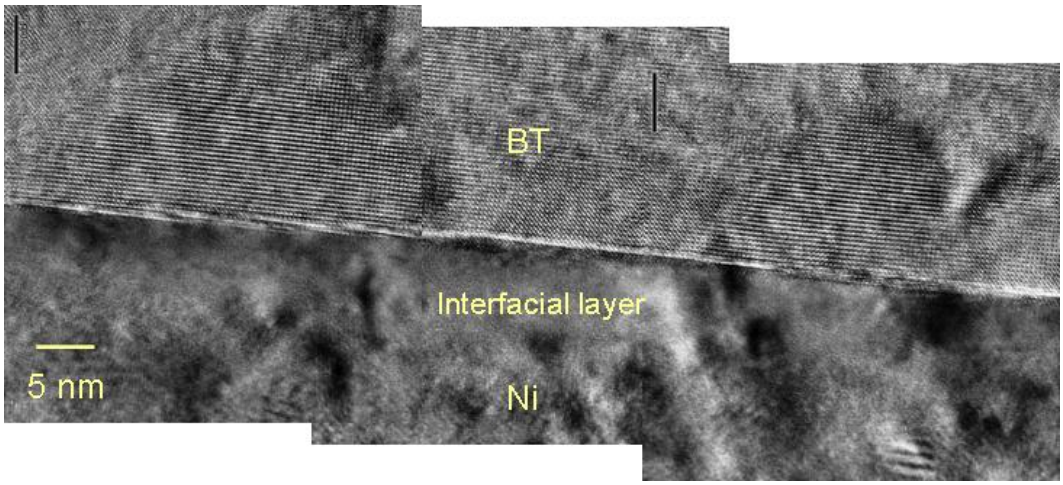

Fig. 4.11 View of a larger section of the $BaTiO_3$/Ni interface showing the interface layer and the lack of NiO (Data courtesy of Dr. Gaiying Yang)

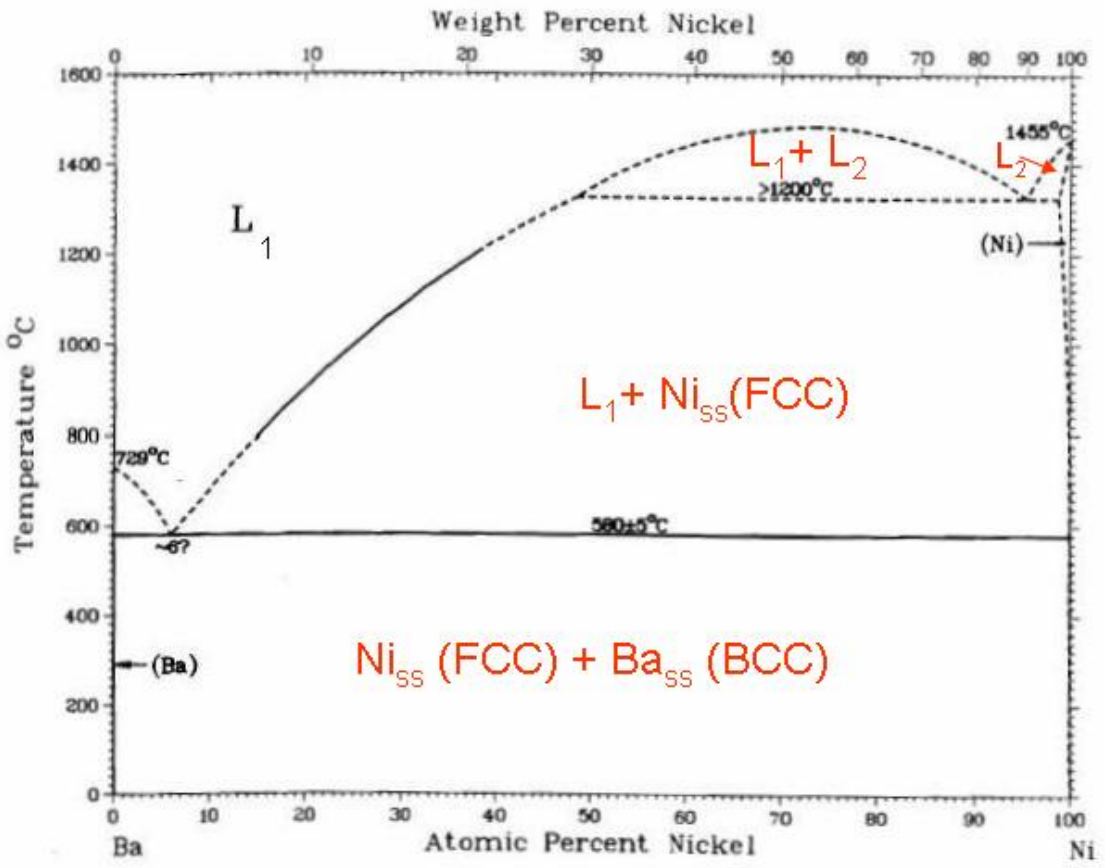

Fig. 4.12 Binary alloy phase diagrams of Ba-Ni (Adapted from Massalski **[30]**)

References

[1] L. A. Giannuzzui and F. A. Stevie, *Introduction to Focused Ion Beams*. Springer: New York, 2005.

[2] J. P. McCaffrey, M. W. Phaneuf and L. D. Madsen, "Surface Damage Formation during Ion-beam Thinning of Samples for Transmission Electron Microscopy," *Ultramicroscopy*, **87** [3], 97-104 (2001).

[3] S. Rubanov and P. R. Munroe, "FIB-induced Damage in Silicon," *Journal of Microscopy-Oxford*, **214**, 213-221 (2004).

[4] J. M. Cairney and P. R. Munroe, "Redeposition Effects in Transmission Electron Microscope Specimens of FeAl-WC Composites Prepared using a Focused Ion Beam," *Micron*, **34** [2], 97-107 (2003).

[5] Z. Surowiak, A. M. Margolin, I. N. Zakharchenko and S. V. Biryukov, "The Influence of Structure on the Piezoelectric Properties of $BaTiO_3$ and $(BaSr)TiO_3$ Thin-films with a Diffuse Phase-transition," *Thin Solid Films*, **176** [2], 227-246 (1989).

[6] B. Angadi, P. Victor, V. M. Jali, M. T. Lagare, R. Kumar and S. B. Krupanidhi, "High Energy Li Ion Irradiation Effects in Ferroelectric PZT and SBT Thin Films," *Thin Solid Films*, **434** [1-2], 40-48 (2003).

[7] M. Sedlar, M. Sayer and L. Weaver, "Sol-Gel Processing and Properties of Cerium Doped Barium Strontium Titanate Thin Films," *Journal of Sol-Gel Science and Technology*, **5** [3], 201-210 (1995).

[8] M. C. Gust, L. A. Momoda, N. D. Evans and M. L. Mecartney, "Crystallization of Sol-Gel-Derived Barium Strontium Titanate Thin Films," *Journal of the American Ceramic Society*, **84** [5], 1087-1092 (2001).

[9] M. C. Gust, N. D. Evans, L. A. Momoda and M. L. Mecartney, "In-Situ Transmission Electron Microscopy Crystallization Studies of Sol-Gel-Derived Barium Titanate Thin Films," *Journal of the American Ceramic Society*, **80** [11], 2828-2836 (1997).

[10] D. M. Tahan, A. Safari and L. C. Klein, "Preparation and Characterization of $Ba_xSr_{1-x}TiO_3$ Thin Films by a Sol-Gel Technique," *Journal of the American Ceramic Society*, **79** [6], 1593-1598 (1996).

[11] C. L. Jia, K. Urban, S. Hoffmann and R. Waser, "Microstructure of Columnar-Grained $SrTiO_3$ and $BaTiO_3$ Thin Films Prepared by Chemical Solution Deposition," *Journal of Materials Research*, **13** [8], 2206-2217 (1998).

[12] R. W. Schwartz, P. G. Clem, J. A. Voigt, E. R. Byhoff, M. Van Stry, T. J. Headley and N. A. Missert, "Control of Microstructure and Orientation in Solution-Deposited $BaTiO_3$ and $SrTiO_3$ Thin Films," *Journal of the American Ceramic Society*, **82** [9], 2359-2367 (1999).

[13] S. Hoffmann, U. Hasenkox, R. Waser, J. L. Jia and K. Urban, "Chemical Solution Deposition of $BaTiO_3$ and $SrTiO_3$ with Columnar Microstructure," In *Mater. Res. Soc. Symp. Proc.*, 1997; Vol. 474, p 9.

[14] J. T. Dawley and P. G. Clem, "Dielectric Properties of Random and < 100 > Oriented $SrTiO_3$ and $(Ba,Sr)TiO_3$ Thin Films Fabricated on < 100 > Nickel Tapes," *Applied Physics Letters*, **81** [16], 3028-3030 (2002).

[15] J. Ihlefeld, B. Laughlin, A. Hunt-Lowery, W. Borland, A. Kingon and J. P. Maria, "Copper Compatible Barium Titanate Thin Films for Embedded Passives," *Journal of Electroceramics*, **14** [2], 95-102 (2005).

[16] R. J. Ong, J. T. Dawley and P. G. Clemk, "Chemical Solution Deposition of Biaxially Oriented (Ba,Sr)TiO_3 Thin Films on < 100 > Ni," *Journal of Materials Research*, **18** [10], 2310-2317 (2003).

[17] R. Wernicke, "Defect Chemistry and Electrical-conductivity of Doped Barium-Titanate Ceramics. 4. Kinetics of Equilibrium Restoration in Barium-Titanate Ceramics," *Philips Research Reports*, **31** [6], 526-543 (1976).

[18] N. H. Chan, R. K. Sharma and D. M. Smyth, "Non-Stoichiometry in Undoped $BaTiO_3$," *Journal of the American Ceramic Society*, **64** [9], 556-562 (1981).

[19] Y. I. Jung, S. Y. Choi and S. J. L. Kang, "Grain-growth Behavior during Stepwise Sintering of Barium Titanate in Hydrogen Gas and Air," *Journal of the American Ceramic Society*, **86** [12], 2228-2230 (2003).

[20] S. Y. Choi and S. J. L. Kang, "Sintering Kinetics by Structural Transition at Grain Boundaries in Barium Titanate," *Acta Materialia*, **52** [10], 2937-2943 (2004).

[21] A. Polotai, K. Breece, E. Dickey, C. Randall and A. Ragulya, "A Novel Approach to Sintering Nanocrystalline Barium Titanate Ceramics," *Journal of the American Ceramic Society*, **88** [11], 3008-3012 (2005).

[22] S. Hoffmann and R. Waser, "Control of the Morphology of CSD-Prepared (Ba,Sr)TiO_3 Thin Films," *Journal of the European Ceramic Society*, **19** [6-7], 1339-1343 (1999).

[23] T. Hosokura, A. Ando and Y. Sakabe, "Fabrication and Electrical Characterization of Epitaxially Grown (Ba,Sr)TiO_3 Thin Films Prepared by Sol-Gel Method," in *Electroceramics in Japan IX*, 2006; Vol. 320, pp 81-84.

[24] G. Y. Yang, E. C. Dickey, C. A. Randall, D. E. Barber, P. Pinceloup, M. A. Henderson, R. A. Hill, J. J. Beeson and D. J. Skamser, "Oxygen Nonstoichiometry and Dielectric Evolution of $BaTiO_3$. Part I - Improvement of Insulation Resistance with Reoxidation," *Journal of Applied Physics*, **96** [12], 7492-7499 (2004).

[25] G. Y. Yang, G. D. Lian, E. C. Dickey, C. A. Randall, D. E. Barber, P. Pinceloup, M. A. Henderson, R. A. Hill, J. J. Beeson and D. J. Skamser, "Oxygen Nonstoichiometry and Dielectric Evolution of $BaTiO_3$. Part II - Insulation Resistance Degradation under Applied dc Bias," *Journal of Applied Physics*, **96** [12], 7500-7508 (2004).

[26] R. Waser, T. Baiatu and K. H. Hardtl, "DC Electrical Degradation of Perovskite-type Titanates.1. Ceramics," *Journal of the American Ceramic Society*, **73** [6], 1645-1653 (1990).

[27] H. Chazono and H. Kishi, "DC-Electrical Degradation of the BT-Based Material for Multilayer Ceramic Capacitor with Ni Internal Electrode: Impedance Analysis and Microstructure," *Japanese Journal of Applied Physics Part 1-Regular Papers Short Notes & Review Papers*, **40** [9B], 5624-5629 (2001).

[28] G. Y. Yang, S. I. Lee, Z. J. Liu, C. J. Anthony, E. C. Dickey, Z. K. Liu and C. A. Randall, "Effect of Local Oxygen Activity on Ni-$BaTiO_3$ Interfacial Reactions," *Acta Materialia*, **54** [13], 3513-3523 (2006).

[29] R. D. Leapman, L. A. Grunes and P. L. Fejes, "Study of the L_{23} Edges in the 3d Transition-metals and Their Oxides by Electron-Energy-Loss Spectroscopy with Comparisons to Theory," *Physical Review B*, **26** [2], 614-635 (1982).

[30] Massalski, T. B., *Binary Alloys Phase Diagrams: V1*, ASM International: OH, 1986.

Chapter 5

Processing Studies for $BaTiO_3$ Films on Ni Foils

This chapter focuses on the use of spectroscopic ellipsometry, X-ray diffraction, and FTIR to characterize the composition and depth profile of the Ni foils and $BaTiO_3$/Ni samples as a function of temperature. Of particular interest was developing an understanding of the effect of processing conditions on the $BaTiO_3$ microstructure, as well as evaluation of the conditions under which NiO forms. Spectroscopic ellipsometry is a useful complement to the transmission electron microscopy studies, because it is a large area technique with good depth resolution.

5.1 Oxidation of Ni foil

In order to develop appropriate processing conditions for $BaTiO_3$ films on Ni foils, it is useful to understand at what point in the processing oxidation of the foil surface would be expected. Thus, the oxidation of Ni foil surfaces was studied by spectroscopic ellipsometry (SE) as a function of process temperature. The Ni foil used for this study was 50 μm thick and 99+ % purity. The surface was visually rough. Atomic force microscopy (AFM) was used to determine the surface roughness of the as-received foil, as shown in **Fig. 5.1**. Over a 5x5 μm area, the average surface roughness was 27 nm, the root-mean-square (rms) roughness was 37 nm, and the peak to valley roughness is as large as 330 nm.

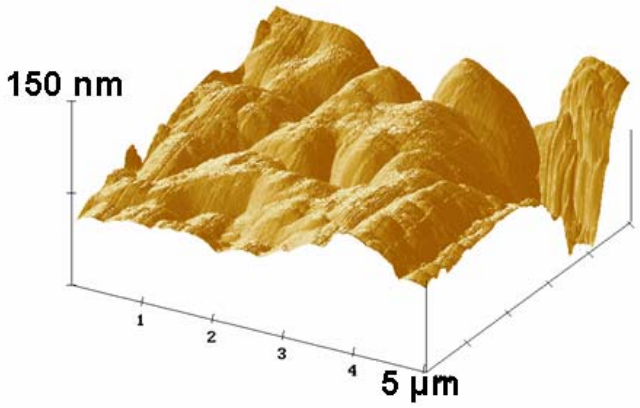

Fig. 5.1 Surface morphology of low purity (99+ %) Ni foil

Ni foils (99+ %) were heated on a hot plate at 200-450^{o}C at 50^{o}C intervals for 2 min. in air. Although none of the XRD patterns (not shown here) had NiO peaks, the color of the Ni foil changed from silver (unannealed) to yellow gold after annealing at 450^{o}C, suggesting the development of a transparent overlayer.

SE data from 250 to 700 nm collected from the Ni foils after each annealing step are shown in **Fig. 5.2**. It is clear that the SE data progressively change as the annealing temperature increases from 200^{o}C to 350^{o}C. A significant change was observed after the Ni foil was annealed at 450^{o}C, implying either a considerably change in the depth profile of the sample or oxidation. It is noted that the intensity of the reflected light from the Ni foils is low due to their surface roughness. This caused difficulty in sample alignment on the ellipsometer.

SE data modeling was performed on these samples by using different possible model structures i.e. models with and without NiO, as shown schematically in **Fig. 5.3**. Surface roughness layers on the Ni foil were treated as a layer of Ni+air on Ni. Models

with NiO consist of either a layer of Ni+NiO or NiO+air on the Ni substrate. In most cases, it was necessary to model SE data only over the range from 300-650 nm since it significantly improves the fit. It is noted that reference data of optical properties for single crystal O-rich NiO **[1]** were used for the growing NiO layer. This point will be further discussed in section 5.4.1.

Two sets of reference data for Ni single crystals (measured at 4 K and room temperature) were used to describe the bulk Ni. The best available data are those measured at 4K, as a well-defined surface was prepared, and the optical properties are reported at a large number of wavelengths over the visible range. Unfortunately, the available data sets for Ni at room temperature are considerably more sparse, and it was not immediately clear what errors would result from using cryogenic data for the Ni. In an attempt to provide a better reference data set, the 4K data were scaled to overlap, as well as possible, with the available room temperature data, without changing the shape of ε_1 and ε_2 as a function of wavelength. **Fig. 5.4** shows reference data for the dielectric function of Ni at 4 K, room temperature and the modified room temperature data. Both data sets, as well as mixtures of the two, were then used to model the data for the Ni foils.

It was found that mixing of the two Ni dielectric functions often decreases sigma and improves the fit to the experimental data on foils. In particular, the best-fit models for Ni foils annealed between 200 and 400^{o}C were obtained using mixed Ni reference data. The relative volume fraction of the 4K reference data was found to vary randomly from 0.12 up to 0.48 for the different annealing temperatures. However, the best fits for the untreated foils and 450^{o}C annealed foils were obtained using only reference data for a Ni single crystal at room temperature and 4 K as the substrate, respectively. At least

some of these discrepancies in the best Ni reference data may result from the fact that the peak-to-valley roughness on these foils, as determined by AFM, is approximately the same as the wavelength used to probe the samples, and is variable from point-to-point and sample-to-sample. Thus, some degree of diffuse scattering is likely to complicate the ellipsometry modeling. Since there is no clear trend for the variation in the optical properties of Ni substrate, only "Ni" will be used to represent the Ni phase in the following discussion.

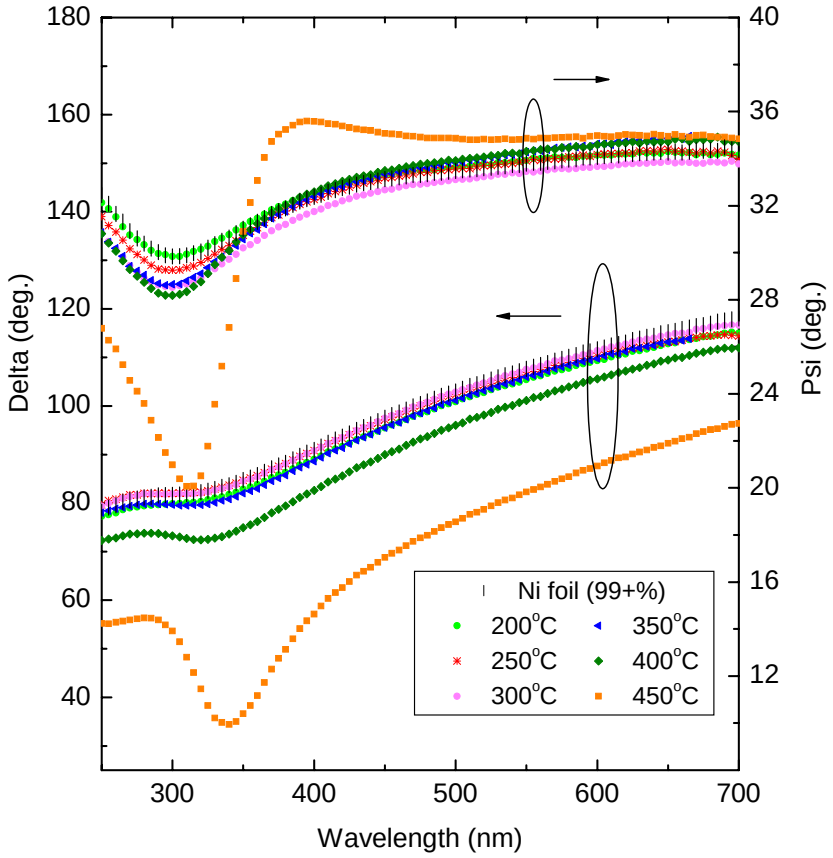

Fig. 5.2 SE data of Ni foil (99+ %) and Ni foil after annealing at 200-450°C for 2 min in air

Fig. 5.3 Schematic of SE models for Ni foils with and without NiO

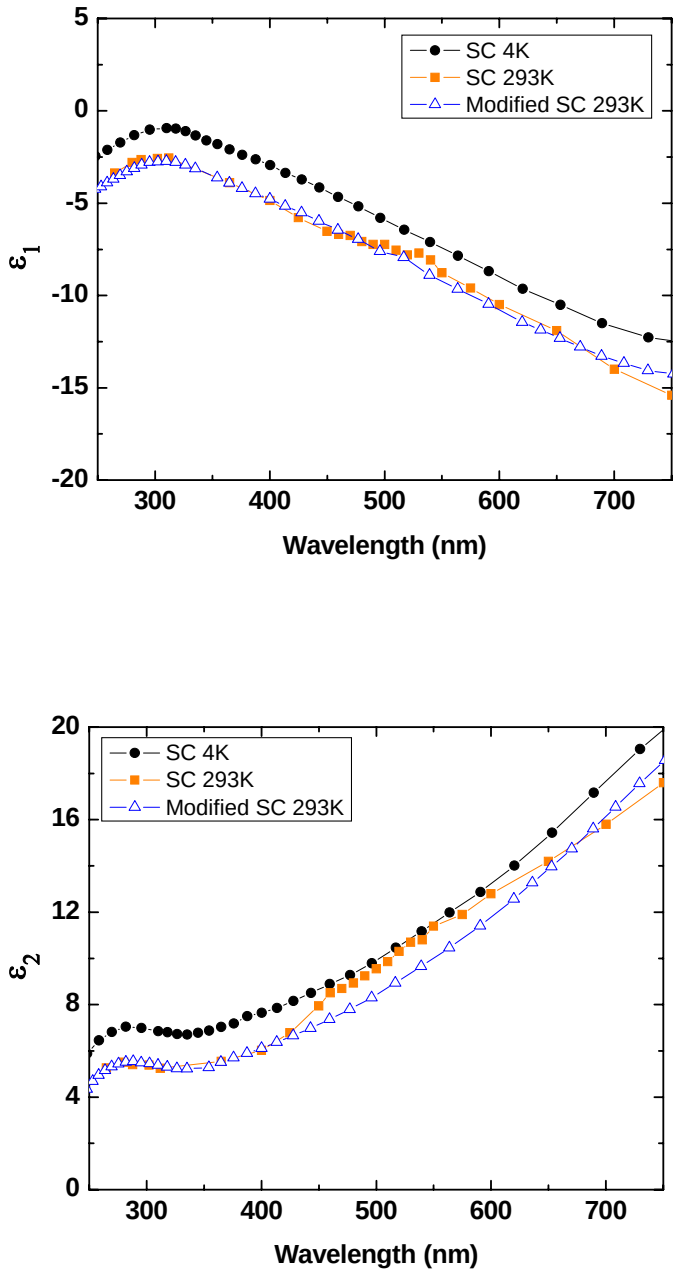

Fig. 5.4 Dielectric functions of Ni single crystals (SC) at 4 K and 293 K. The modified room temperature data set developed in this work is also shown.

To establish a baseline, data for an as-received Ni foil were first modeled. The best fit model for the sample included a layer of surface roughness, but no NiO. Compared to a model of Ni/Ni+NiO, the model involving only roughness showed an improved fit at short wavelengths, as shown in **Fig. 5.5**, and sigma decreased from 0.019 to 0.01. The roughness layer is 72.1± 4.1 Å thick with 21% volume air, as shown in **Fig. 5.7**. Thus the layer of surface roughness of the Ni foil detected by SE is thinner than that detected by AFM. This may be a result of differences in the sampling areas or problems associated with the inability to properly model asperities with a size scale on the order of the wavelength of light. It is noted that modeling the as-received sample with Ni/NiO+air gave an unreasonable model.

Best fit models of Ni foils annealed at 200^{o}C or 250^{o}C were also found to consist of rough Ni, the same as for the as-received Ni foil. For Ni foils annealed at 300^{o}C and higher (up to 450^{o}C), the best fit models were obtained from Ni/NiO+air. The results suggested that Ni oxidation begins when un-coated Ni foils are annealed at 300^{o}C. Fits of experimental and modeled data of these annealed foils are shown in **Fig. 5.6**.

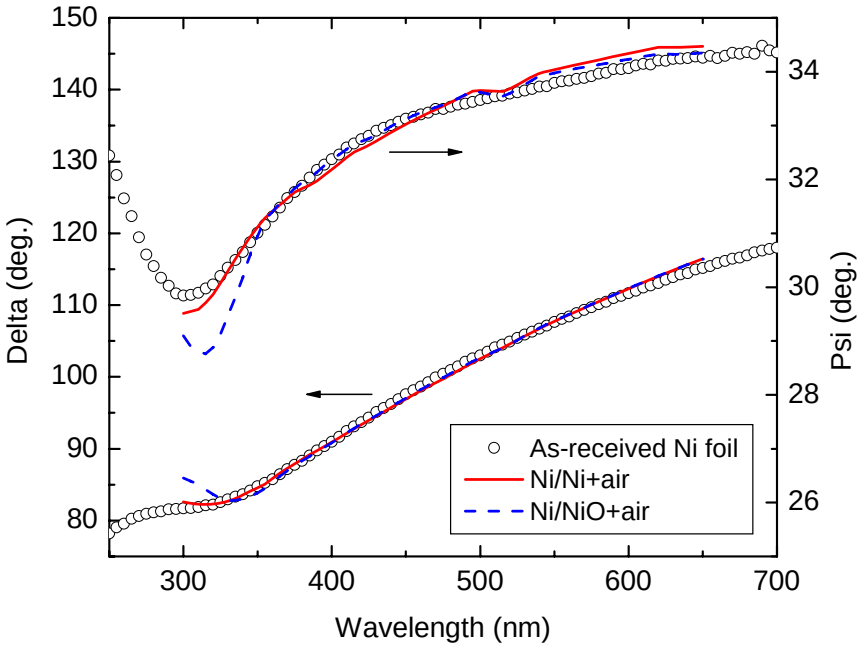

Fig. 5.5 Experimental and modeled data with and without NiO for an as-received Ni foil

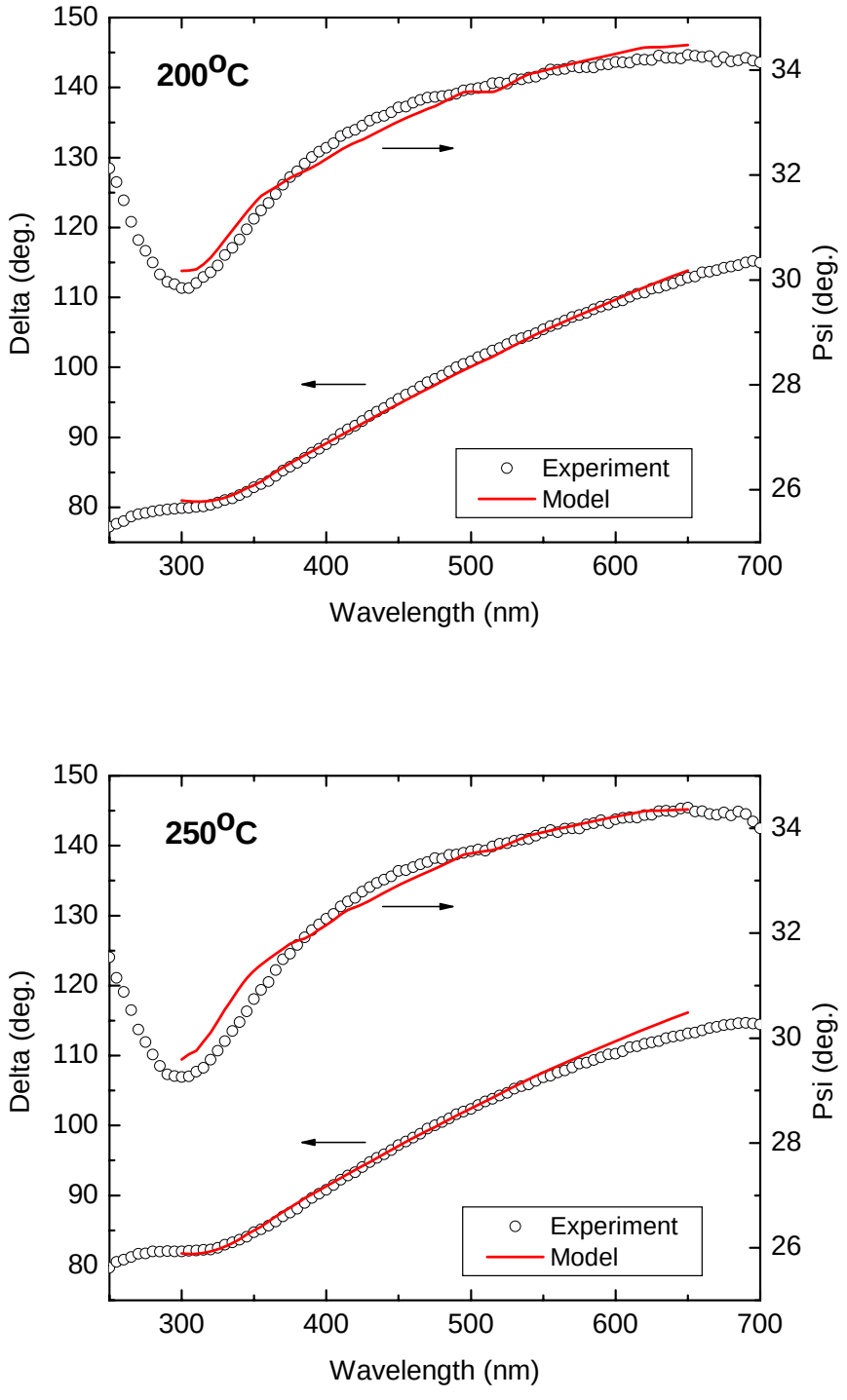

Fig. 5.6 Experimental and modeled data for Ni foils annealed at different temperatures

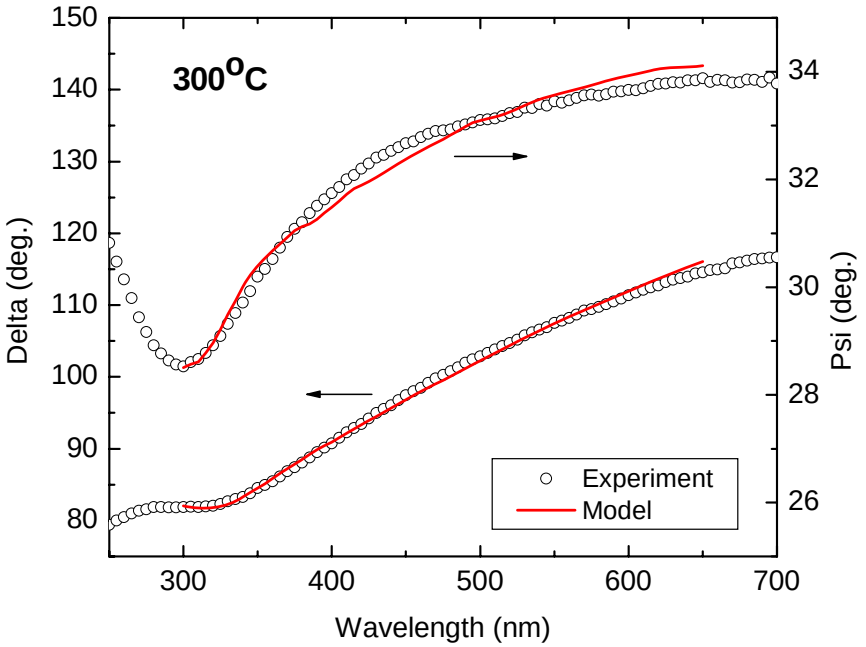
300°C
Delta (deg.)
Psi (deg.)
Wavelength (nm)
Experiment
Model
150
140
130
120
110
100
90
80
34
32
30
28
26
300
400
500
600
700

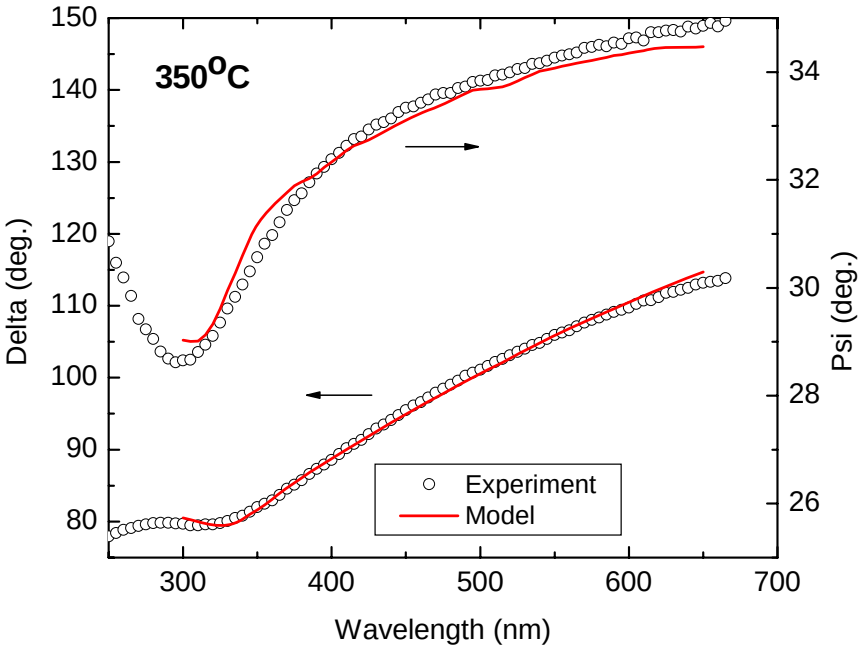
350°C
Delta (deg.)
Psi (deg.)
Wavelength (nm)
Experiment
Model
150
140
130
120
110
100
90
80
34
32
30
28
26
300
400
500
600
700

Fig. 5.6 (cont.)

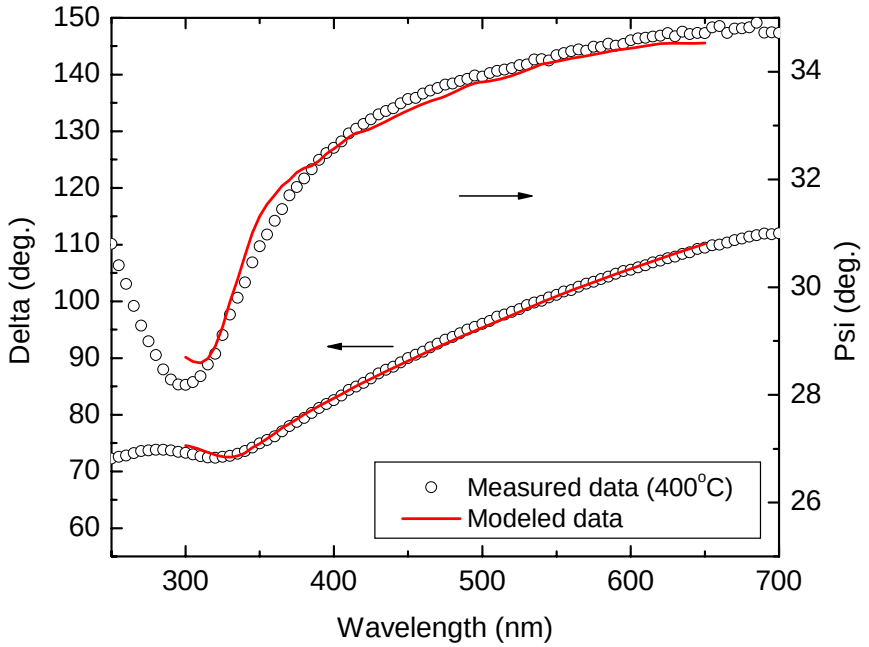
Delta (deg.)
Psi (deg.)
Wavelength (nm)
Measured data (400°C)
Modeled data

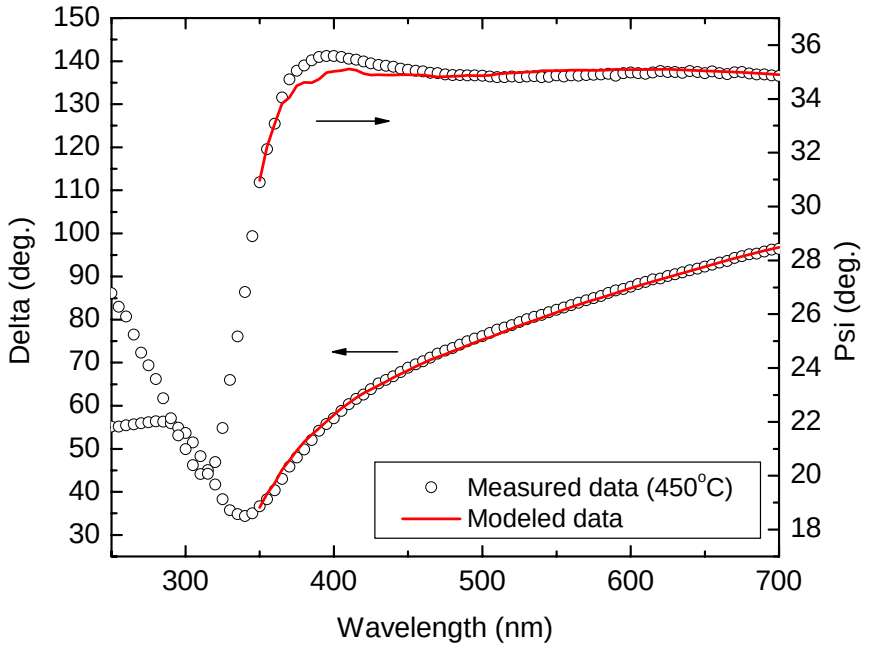
Delta (deg.)
Psi (deg.)
Wavelength (nm)
Measured data (450°C)
Modeled data

Fig. 5.6 (cont.)

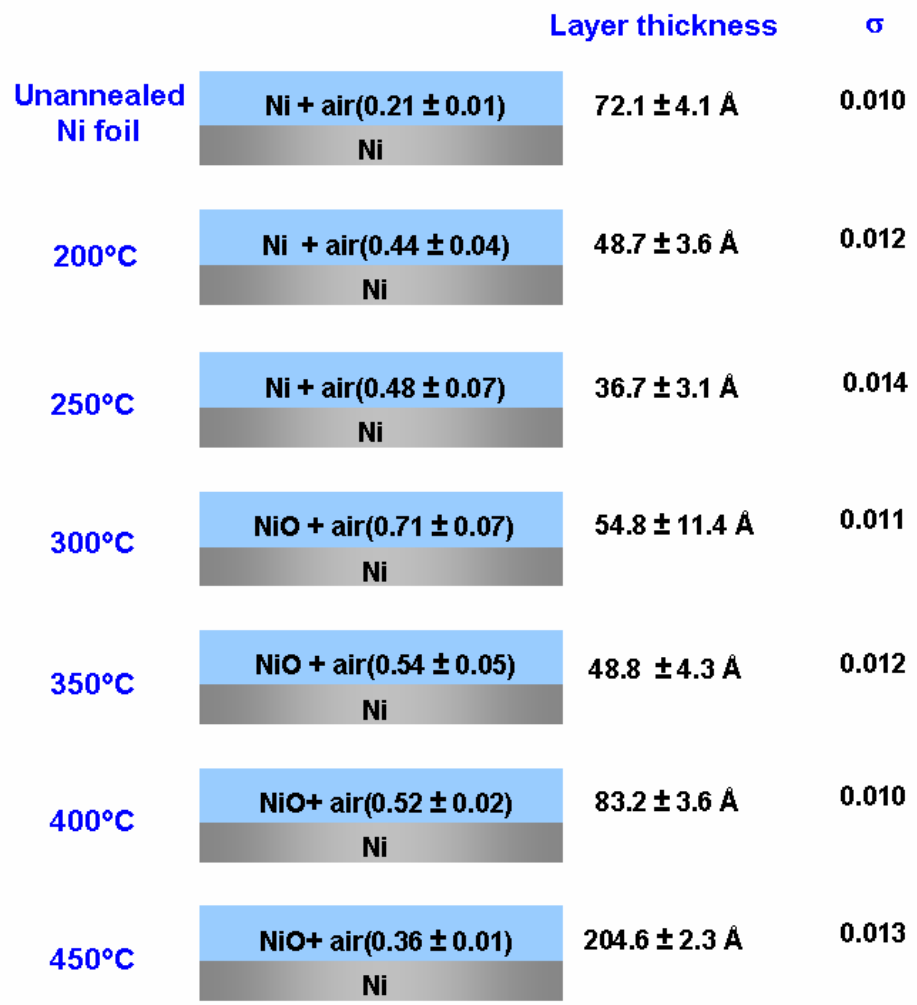

Fig. 5.7 SE – determined depth profiles from as-received and annealed Ni foils

Depth profiles of the best-fit models for as-received and annealed Ni foils are presented in **Fig. 5.7**. In addition to an increase in the thickness of the NiO+air layer, the volume fraction of air in the layer decreases from 0.71±0.07 to 0.36±0.01as the annealing temperature increases from 300°C to 450°C. The total thickness of the NiO+air layer and the effective thickness of NiO for each sample are plotted in **Fig. 5.8**. The effective thicknesses of NiO were calculated by multiplying the volume fraction of NiO by the thickness of the layer. Thus, despite the difficulties associated with the rough Ni surface, the SE results of this experiment agree well with an *in situ* reflectance study of a heated Ni film **[2]**, which showed oxidation occurs at 300°C.

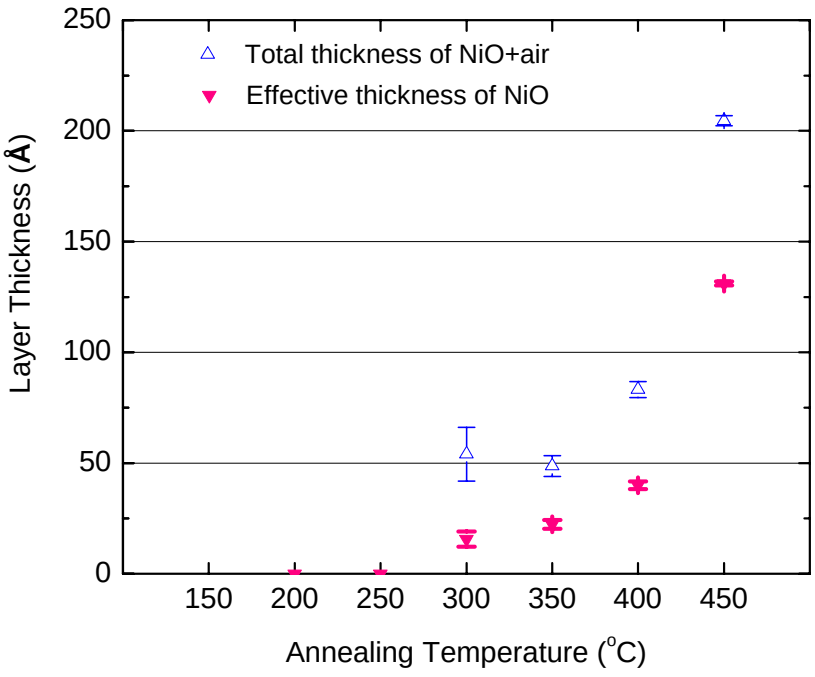

Fig. 5.8 Plot of total thickness of NiO+air layer and effective thickness of NiO

5.2 High purity Ni foils

In the previous section it was shown that, despite the rough surface, low purity Ni foil (99%) can be used in a SE study to observe oxidation and determine the NiO thickness at low temperatures. However, preliminary work found that these foils were less useful for SE study when severe oxidation occurred, i.e. the surface of the foil became seriously roughened and the amount of detected light was too low. In addition, it was found that the acetic acid used in $BaTiO_3$ solution attacked the Ni surface, presumably etching it, and further increasing the surface roughness. This made it impossible to obtain interference fringes in SE data from $BaTiO_3$ films on low purity Ni foils (See **Fig. 5.9**).

To minimize these difficulties, high purity cold-rolled Ni foil (99.99%) was chosen as the substrate for further study of the Ni-$BaTiO_3$ thin film interface by SE as its surface is smoother than the one of 99+% purity. Earlier work of Nagata et al. **[3]** reported that pre-annealing these Ni foils at 900^{o}C results in a much smoother surface. Also, due to its higher purity, there were fewer oxidized contaminants on the surface after annealing, compared to the low purity Ni foil. In addition, the smooth and clean surface of the high purity Ni foil provides better dielectric properties for the resulting $BaTiO_3$ thin films **[3]**.

In this experiment, a high purity Ni foil was pre-annealed at 900^{o}C for 1 hour in 10^{-16} atm pO_2. **Fig. 5.10** shows the surface microstructure and morphology of the as-received and pre-annealed Ni foil. The as-received Ni foil, which was cold-rolled and thus highly deformed, shows no clear grain features. The scratches and roughness on the surface are due to the rolling process. After pre-annealing, the Ni grain size varies

between 20 and 200 μm. The surface of Ni foil becomes much smoother due to diffusion at high temperature. In addition, grain boundary grooves develop at the surface in order to reduce the combined surface and grain boundary free energy **[4, 5]**.

The surface roughness of the high purity Ni foils was investigated by AFM. The measured area was 5x5 μm^2, which is very small compared to the grain size. It was found that the average roughness (R_a) decreases from 6 nm to 4 nm after annealing. **Fig. 5.9** demonstrates that using high purity Ni foil as a substrate, interference fringes from the transparent $BaTiO_3$ film can be seen in the SE data. Also, the smoother surface of the underlying substrate results in good reflection and easier sample alignment. Models of the SE data for $BaTiO_3$ film on the Ni foil will be discussed in section 5.4.

As was the case for the lower purity foils, the surface roughness measured by ellipsometry was smaller than the AFM result (see **Table 5.1**). However, the correlation between the two was good. That is, foils that were measured to be smoother by AFM were also smoother by SE. Again, the differences may be due to some of the larger scale topology that complicates the SE modeling.

Table 5.1 AFM and SE surface roughness of 99+% and pre-annealed 99.99% Ni foil

Sample	Surface roughness (d)	
	d_{AFM} (Å) (or R_a)	d_{SE} (Å)
Ni foil (99+%)	270	72.1 ± 4.1
Pre-annealed Ni foil (99.99%)	40	2.0 ± 0.8

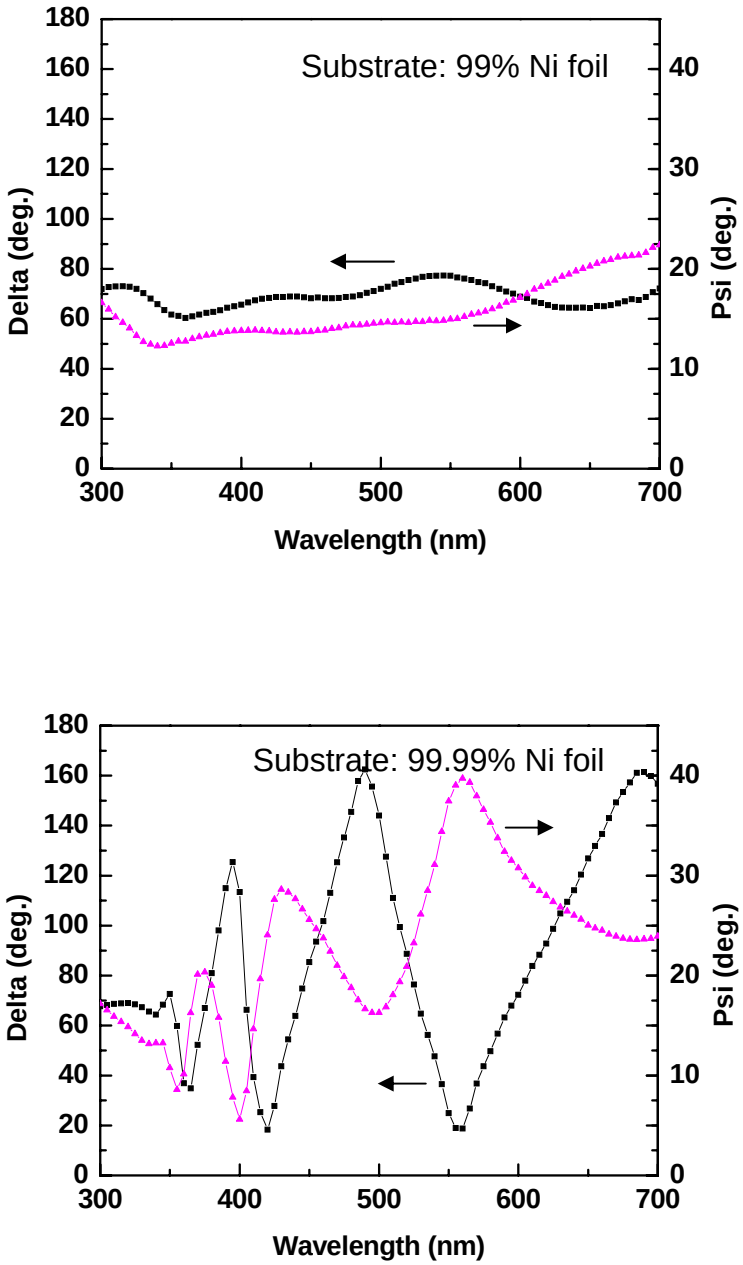

Fig. 5.9 SE data collected from $BaTiO_3$ films on 99% and 99.99% Ni foils

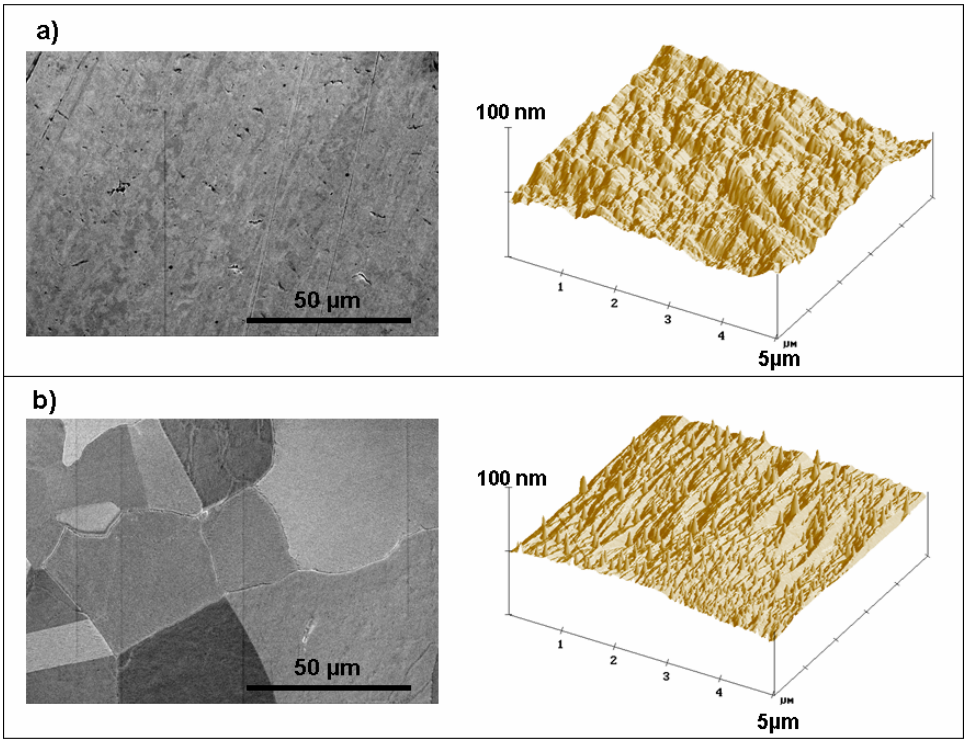

Fig. 5.10 Microstructure and surface morphology of high purity Ni foils (99.99 %) a) as-received and b) after pre-annealing at 900^{o}C. Both SEM and AFM data are shown.

5.3 $BaTiO_3$ films on Ni foils

5.3.1 Structure and microstructure

Fig. 5.11 showed XRD patterns of a pre-annealed Ni foil and $BaTiO_3$ films RTA'd at different temperatures under flowing N_2. The pre-annealed Ni foil shows only a strong 200 diffraction peak, suggesting that the foil is at least partially oriented after re-crystallization. The film RTA'd at 600°C shows an extremely low intensity of the $BaTiO_3$ 100 and 110 peaks, along with a trace amount of a second phase at a two-theta of 26.7°. The second phase peak corresponded to the highest peak of an oxycarbonate ($Ba_2Ti_2O_5CO_3$), which was reported to be an intermediate phase in the crystallization of perovskite $BaTiO_3$ **[6-9]**. A recent paper suggests that this intermediate phase may, in fact, contain very little Ti **[10]**. For the films RTA'd at 650-750°C, the "oxycarbonate" phase disappears and slightly higher intensity $BaTiO_3$ peaks are shown. However, the low intensity of the $BaTiO_3$ XRD peaks in RTA films suggested that the films are either not well-crystallized, or have small coherently diffracting region sizes even for RTA temperatures of 750°C. This could be due to the small thermal budget and the low pO_2 (N_2 flow) used in the RTA step. Since the electron diffraction pattern showed no sign of an amorphous phase (diffuse ring), the low intensity of the RTA films is presumably due to the small crystallite size.

These same films were then annealed in a reducing atmosphere furnace at 1000°C for 1 hour. The XRD patterns after furnace annealing are shown in **Fig. 5.12**. The patterns for all films correspond to a well-crystallized polycrystalline perovskite phase with a high intensity of the 100 and 200 peaks. There is no clear peak splitting for the 001/100, 101/110, 002/200 or 112/211 peak pairs. Thus, the $BaTiO_3$ films on Ni foil

have a pseudocubic perovskite structure with some degree of <100> orientation. The high intensity and narrow peaks suggest furnace annealed films exhibit larger grain size, compared to those of RTA'd films.

Since NiO peaks were not observed in XRD patterns measured with a 0.5 sec. collection time per point (**Fig. 5.10** and **Fig. 5.11**), a slower scan with a 5 sec. collection time per point was performed on all films over the 2-theta range where the NiO 111 and 200 peaks are expected. **Fig. 5.13** shows that slow x-ray diffraction scans on RTA films did not show NiO. For furnace annealed films (**Fig. 5.14**), there is a small NiO 200 peak, however, no NiO 111 peak is observed.

Thus, the slow scan x-ray diffraction showed that NiO appears after the furnace anneal. To isolate whether the NiO formed during the high temperature step, or during subsequent re-oxidation, slow scan diffraction was performed after each step. It was found that NiO formation occurs in the re-oxidation step (See **Fig. 5.15**). The re-oxidation was done at 600^{o}C at a pO_2 of 10^{-6} atm, which is above the Ni/NiO equilibrium. Thus, it is possible that annealing for 1 hour could cause Ni oxidation. The very low intensity of the peak implies that there is only a small amount of NiO. There is no significant trend in the amount of NiO for the furnace annealed films as a function of the RTA temperature.

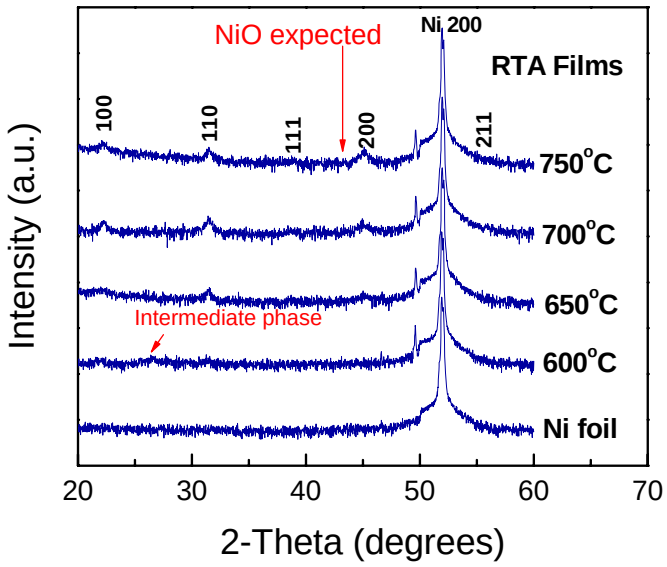

Fig. 5.11 XRD patterns of $BaTiO_3$ films on high purity Ni foils RTA'd at different temperatures

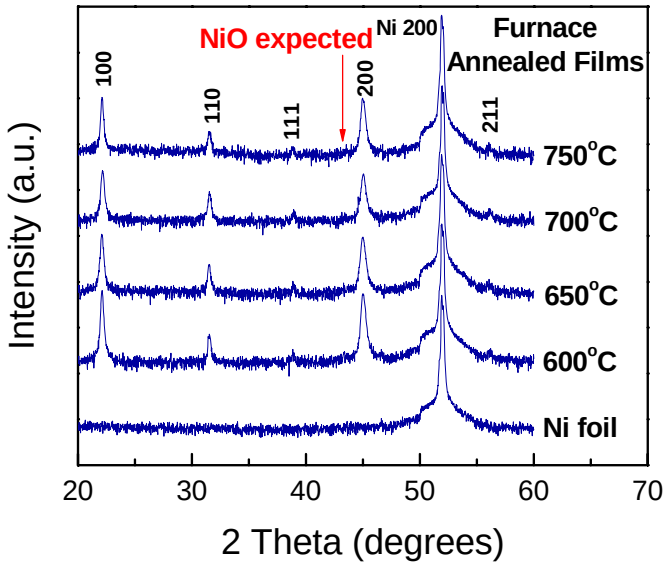

Fig. 5.12 XRD patterns of furnace annealed $BaTiO_3$ films that were RTA'd at different temperatures

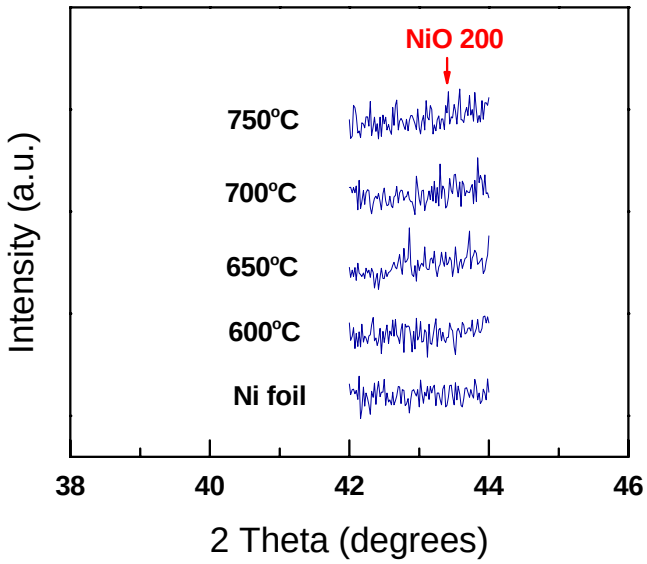

Fig. 5.13 Slow x-ray diffraction scan of RTA annealed $BaTiO_3$ films on Ni foil

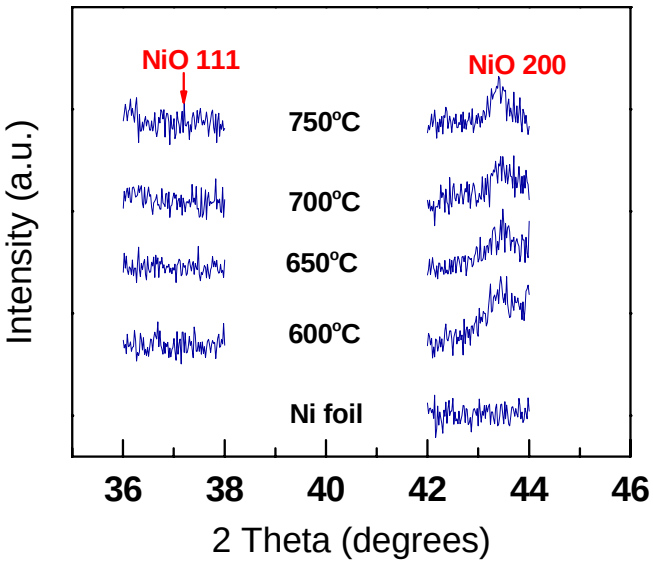

Fig. 5.14 Slow scan x-ray diffraction pattern of furnace annealed $BaTiO_3$ films on Ni foil The films were RTA annealed at different temperatures (600-750°C) before the furnace anneal step

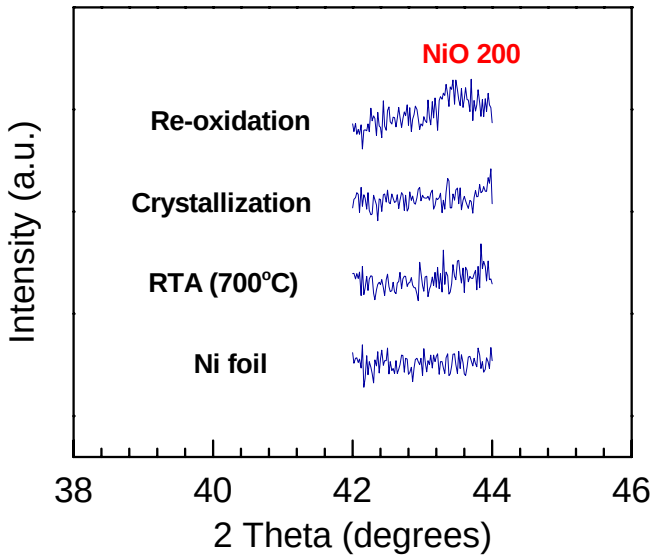

Fig. 5.15 Slow scan of x-ray diffraction showing NiO after re-oxidation of 700°C RTA'd $BaTiO_3$ film

The surface microstructure of furnace annealed (1000°C) $BaTiO_3$ films on Ni foils was observed by SEM, as shown in **Fig. 5.16.** All the films are crack-free and consist of equiaxed grains with some porosity. The grain size of the furnace annealed films that were RTA'd at 600°C and 650°C appear to be about 80-100 nm. The 700°C RTA'd film shows a slightly smaller grain size of 50-80 nm while a slightly larger grain size of 80-150 nm is observed in the 750°C RTA'd film. It is noted that all the films also contain some grains of very small grain size, on the order of 25 nm or less, which are hard to resolve by SEM. It was also observed that there was some spatial non-uniformity in the grain size on a given film. It is recommended that in future work, the grain size be studied as a function of solution aging and/or variation of pO_2 during annealing.

The porosity tends to decrease as the RTA temperature increases. It is believed that in an RTA step with flowing N_2, organic removal is incomplete (See section 5.3.2) and that porosity is developed when the film is subsequently furnace annealed. As has been described by Scherrer, in some solution–deposited films, if crystallization is initiated before densification is complete, the resulting films can incorporate porosity **[11]**.

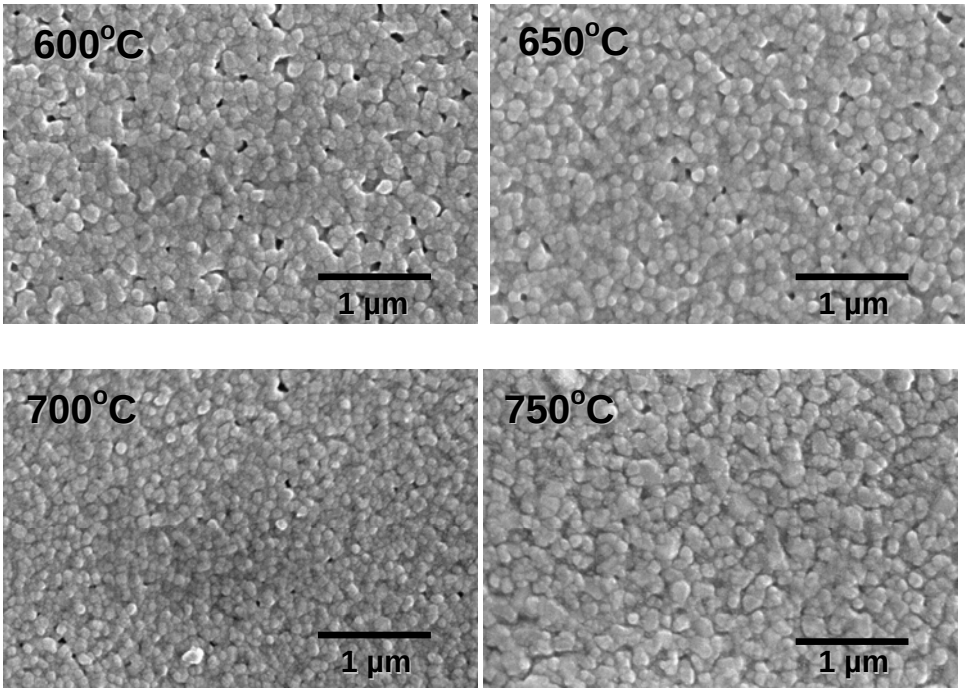

Fig. 5.16 Microstructure of furnace annealed $BaTiO_3$ films (for different RTA temperatures) on Ni foil

5.3.2 Organic decomposition at low temperature processing

Methanol-based $BaTiO_3$ solution

The previous section demonstrated that the residual porosity in $BaTiO_3$ films depends on the RTA annealing (600-750^oC). It is important to note that the porosity is retained after the furnace anneal at 1000^oC. To determine whether this could be related to retained carbon, thermal gravimetric analysis (TGA) and differential scanning calorimetry (DSC) on the dried powders were carried out simultaneously on a TA Instruments SDT 2960 to examine the decomposition behavior of a $BaTiO_3$ powder obtained from a solution. The $BaTiO_3$ solution was air dried at 150^oC for 15 h and then ~ 20 mg of powder was heated to 900-1200^oC at a heating rate of 5 or 10^oC/min. The measurements were performed both in air and with the N_2 flow rate set at 100 cc/min. To complement this study, dried $BaTiO_3$ powders were also calcined at different temperatures (500-900^oC) in air for 1 h and the phase content was identified by XRD.

Fig. 5.17 shows a comparison of the thermal analysis results in air and N_2 for powder dried from a methanol-based $BaTiO_3$ solution. The total weight loss of 40% is the same for both air and N_2 flow. However, clearly the TGA curves measured in air and N_2 show complete decomposition at different temperatures (~750^oC for air flow and ~1000^oC for N_2 flow). In addition, the rate and amount of weight loss varies significantly at temperatures between ~400-600^oC. Accordingly, the DSC curves reveal a sharp exothermic peak at ~ 450-500^oC in air while a smaller and broader peak is shown in N_2. In addition, for measurements in N_2 flow, it is clear that the decomposition is completed at lower temperatures when slower heating rates (5^oC/min) are used.

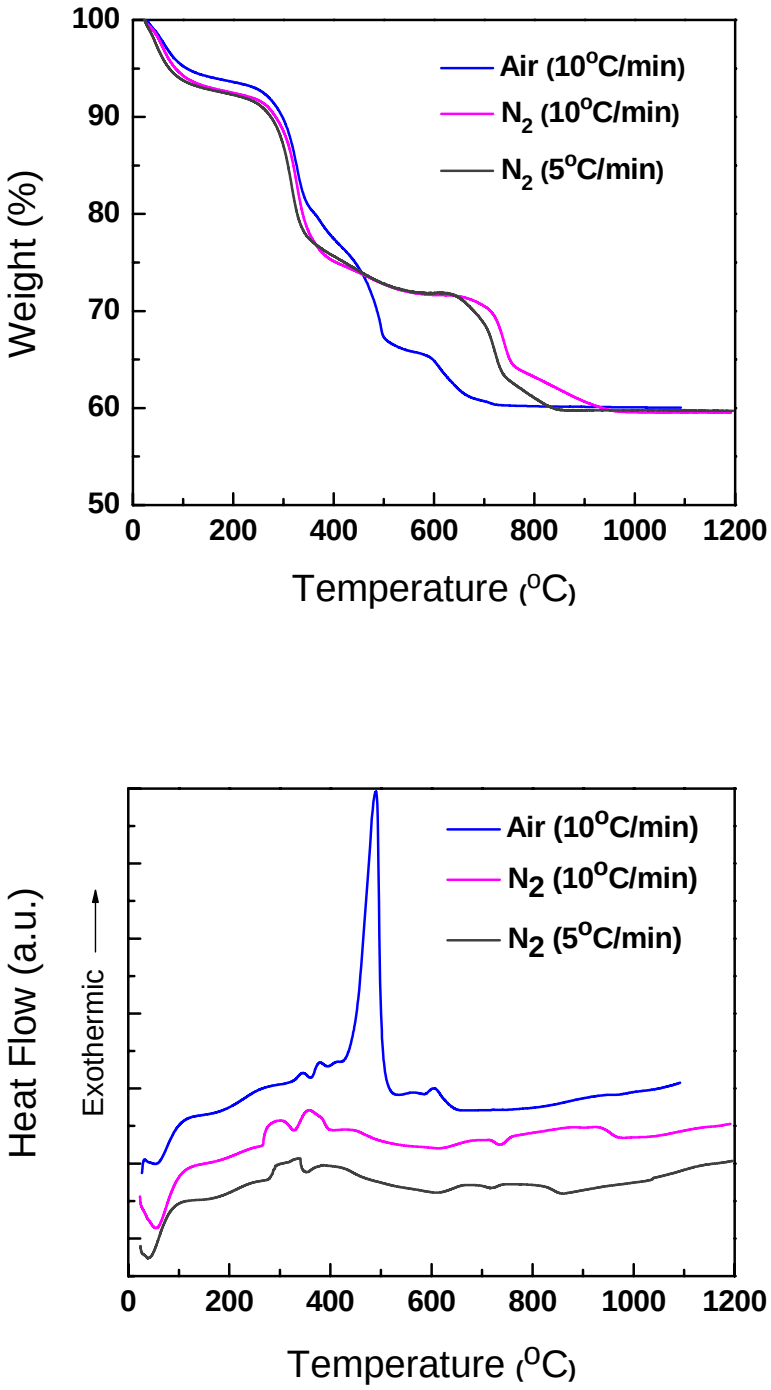

Fig. 5.17 TGA and DSC curves of dried powder from methanol-based $BaTiO_3$ solution

The data for the sample measured in flowing air will be described first. The weight loss (5.8%) from 25^{o}C to 200^{o}C is due to evaporation of the solvent and absorbed moisture, which agrees well with the endothermic peak shown at 55^{o}C in the DSC curve. At 200-400^{o}C, the weight loss (14.7%) and the associated DSC peaks can be attributed to pyrolysis of organics. At ~400-550^{o}C, the powder heated in flowing air shows weight loss (12.6%) due to further removal of organics and a sharp exothermic peak at 490^{o}C. **Fig. 5.18** shows that powder calcined at 500^{o}C for 1 h in air consists of amorphous material along with $BaCO_3$ and either $Ba_2Ti_2O_5CO_3$ or the calcite-like $BaCO_3$. These phases have previously been reported as intermediate phases in $BaTiO_3$ crystallization **[6, 8, 9, 12-15]**. The result suggested that the strong exothermic peak is due to formation of the intermediate phases. The exothermic peak at 605^{o}C is indicative of crystallization of $BaTiO_3$, which is confirmed in **Fig. 5.17**. Upon heating, crystallization continues (as witnessed by the higher intensity of the $BaTiO_3$ peaks) and the amount of the second phases gradually decreases. The oxycarbonate phase and $BaCO_3$ completely disappeared when the powder was calcined at 700^{o}C and 900^{o}C, respectively. It is believed that the last weight loss (5.9%) is due to decomposition of the carbonate phase.

Similar TGA and DSC curves are observed when the $BaTiO_3$ powder was heated in flowing N_2 from room temperature to ~400^{o}C at the same heating rate (10^{o}C/min). Above 400^{o}C, the TGA curve clearly shows a delay in the weight loss and the complete thermal decomposition is extended (from 750^{o}C in air) to 1000^{o}C. In contrast to DSC in air flow, the DSC in N_2 shows a small and broad exothermic peak at 450^{o}C, suggesting carbonate phases are gradually formed in flowing N_2. The DSC curve in N_2 shows extra peaks at 740^{o}C and 935^{o}C, compared to that in air. Thus, it is believed that the delay in

weight loss is accompanied by slowing down other reactions, including carbonate decomposition and thus $BaTiO_3$ crystallization. As expected, the extra reaction peaks in DSC are shifted to lower temperature as heating rate decreases.

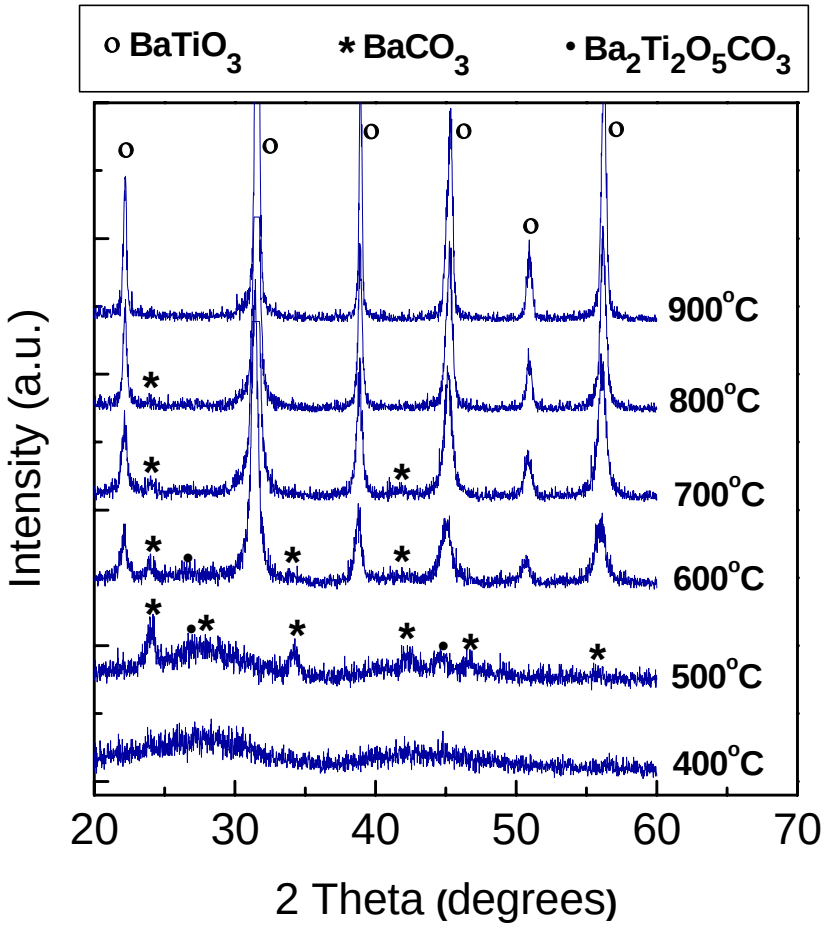

Fig. 5.18 XRD patterns of powders calcined in air at different temperatures

The results above show that organic burn-out is delayed when there is insufficient oxygen available at elevated temperatures. Therefore, it is possible that $BaTiO_3$ films RTA'd at $\leq 750^oC$ in N_2 might have remaining organics that are ultimately the origin of the film porosity on subsequent furnace annealing at 1000^oC (see **Fig. 5.16**), especially as the heating rate in RTA ($10^oC/s$) is much faster than this thermal analysis experiment (5 and $10^oC/min$). It would be important to further quanitify, in future work, the amount of any residual carbon in the furnace annealed samples as well. Although a heating rate of $5^oC/min$ in the furnace annealing will assist organic removal, the low pO_2 might retard the process. These results also suggest that it will be important to further optimize the pyrolysis steps to minimize the amount of carbon retained in the films.

Thermal analysis in air of dried powder from $BaTiO_3$ solutions has shown that the crystallization pathway from amorphous to perovskite $BaTiO_3$ occurred via a $BaCO_3$ intermediate. In contrast, 600^oC RTA'd $BaTiO_3$ thin film on Ni foil shows only a small amount oxycarbonate as an intermediate phase (**Fig. 5.11** in section 5.3.1). Future work should be done to determine whether this difference is a result of the fast heating rate and low pO_2 during the RTA step in flowing N_2.

2-Methoxyethanol-based $BaTiO_3$ solution

Thermal analysis was also performed on dried $BaTiO_3$ powders (with 1% Ca) from a 2-methoxyethanol-based solution to compare to the result of methanol-based powders. (The experiment was done by Dr. Song Won Ko.) A 2-methoxyethanol-based solution was prepared as described in section 3.1.1. The dried powders were analyzed in the TGA at a heating rate of $10^oC/min$.

Fig. 5.19 shows the TGA results of the 2-methoxyethanol-based powders compared to those from methanol-based solutions. It can be seen that, in air, the weight losses from both powders were completed at approximately the same temperature (700-750^{o}C for 2-methoxyethanol and 800^{o}C for methanol). In N_2, the completed decomposition of the 2-methoxyethanol-based powders is delayed to 800^{o}C, which is much lower than that of the methanol-based powders. Therefore, 2-methoxyethanol-based solutions may be more suitable for processing in low pO_2 conditions.

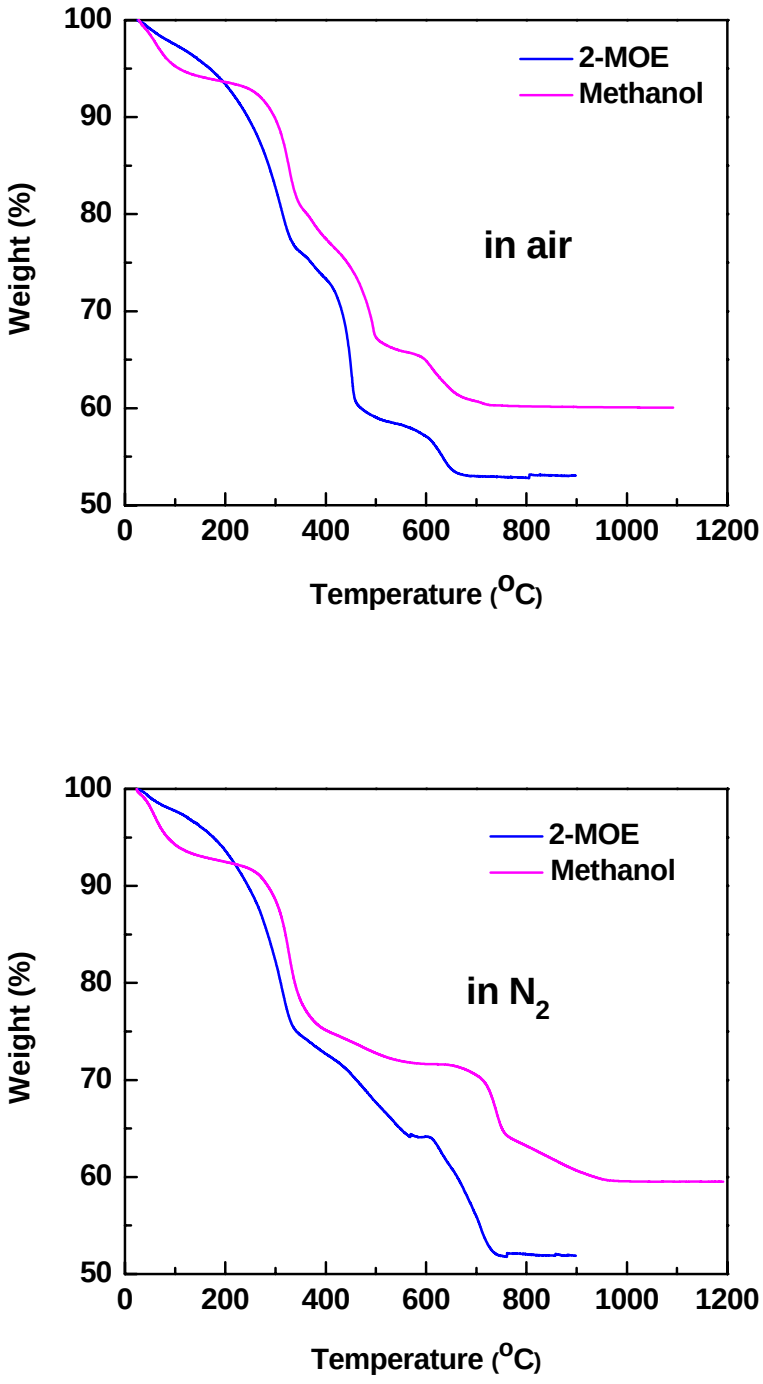

Fig. 5.19 TGA curves of dried powders from 2-methoxyethanol (2-MOE) and methanol based $BaTiO_3$ solutions (2-methoxyethanol data courtesy of Dr. Song Won Ko)

The organic removal from 2-methoxyethanol-based $BaTiO_3$ films was also investigated by a Nexus 670 (Thermo Nicolet) Fourier transform infrared spectroscopy (FTIR) technique. The experiment was performed by Dr. David Lu. A 0.3 M solution was spin coated onto SiO_2/Si substrates. Four layer films were dried at different temperatures (125^{o}C, 390^{o}C and 500^{o}C) in air for 5 min, where the drying temperatures were chosen as points above some weight loss event.

Fig. 5.19 shows the FTIR spectra and thickness of the 2-methoxyethanol-based $BaTiO_3$ films dried at different temperatures. The as-deposited film shows peaks characteristic of carboxylate (at 1560 cm^{-1}) and carbonate groups (at 1425 cm^{-1}), OH (3300-3500 cm^{-1}) and C-H bonds (2880-3020 cm^{-1}) **[16, 17]**. The OH and C-H stretching vibrations are due to the presence of hydroxyls and organic molecules, respectively, in the film. These bands disappear after drying the film at 390^{o}C. The carboxylate group, which significantly decreases after 390^{o}C, almost disappears after 500^{o}C. Although the carbonate peak (which could arise, at least in part, from $BaCO_3$) intensity decreases as the drying temperature increases, some carbonate is clearly retained in the 500^{o}C dried film. The thicknesses of the films, measured by a profilometer, collapse to around 40% of the initial thickness after drying at 500^{o}C, as shown in **Fig. 5.20**.

Fig. 5.21 shows FTIR spectra of 2-methoxyethanol-based $BaTiO_3$ films RTA'd at 750^{o}C in air or N_2 for 10 minutes. The films were previously dried at different temperatures (125^{o}C, 390^{o}C or 500^{o}C). The Ti-O and $BaTiO_3$ features confirm the crystallization of some $BaTiO_3$ after an RTA step in either air or N_2. However, in both cases (and for all drying conditions investigated), there are still features in the FTIR data characteristic of carboxylate and carbonate groups.

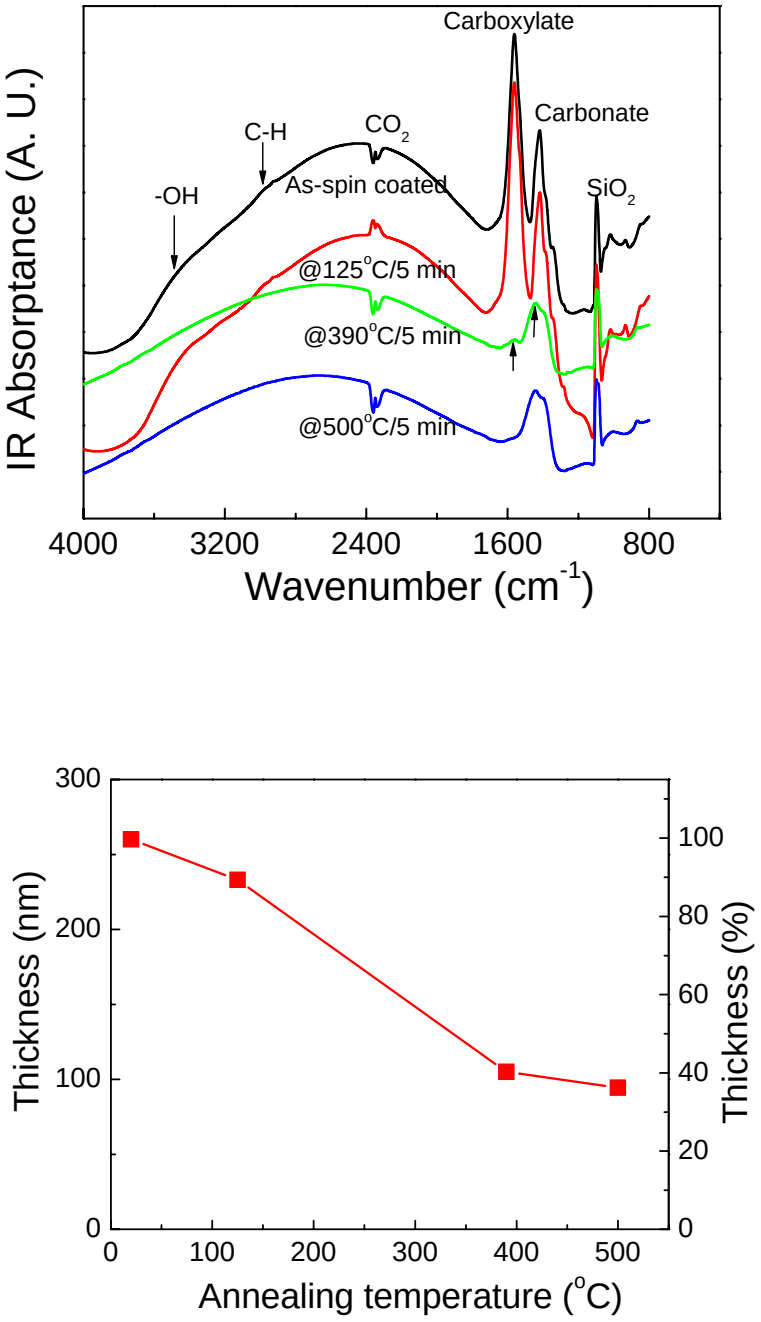

Fig. 5.20 FTIR spectra and thickness of deposited 2-methoxyethanol-based $BaTiO_3$ films dried at different temperature (Data courtesy of Dr. David Lu)

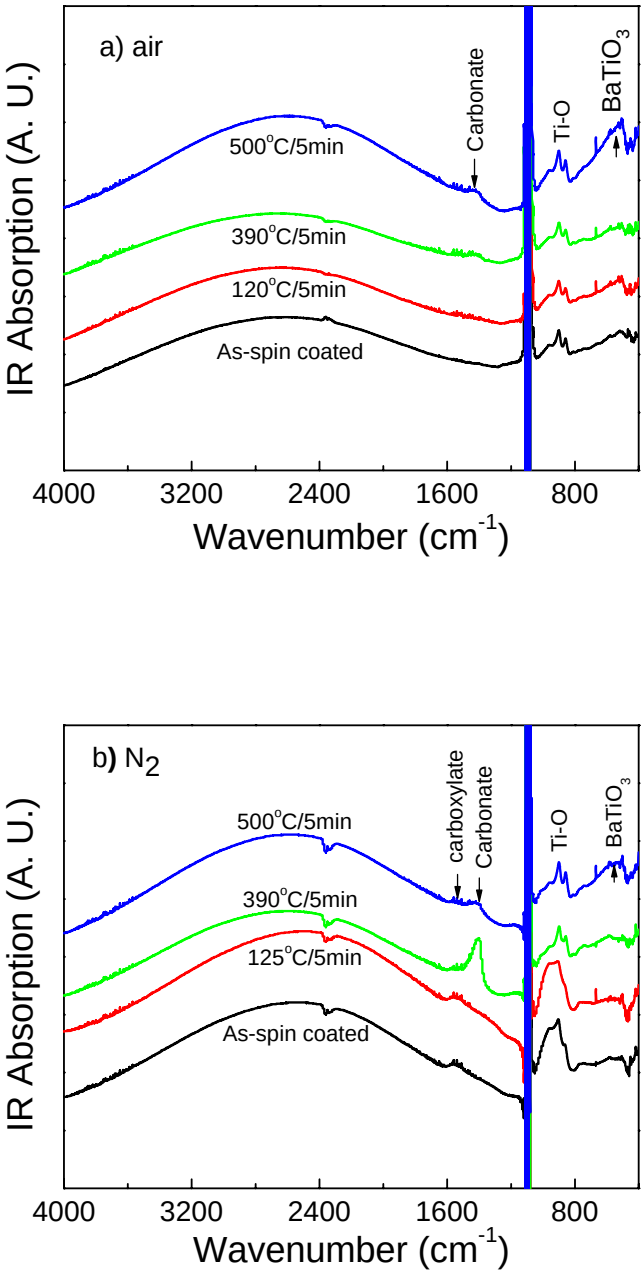

Fig. 5.21 FTIR spectra of 2-methoxyethanol-based $BaTiO_3$ films RTA'd at 750°C a) in air and b) in flowing N_2. The films were dried at different temperatures (125°C, 390°C or 500°C) (Data courtesy of Dr. David Lu)

5.4 Spectroscopic ellipsometry studies

5.4.1 Amorphous dried $BaTiO_3$ films

Spectroscopic ellipsometry has previously been used to characterize the relative density, oxidation state and surface roughness of $BaTiO_3$ films and ceramics **[18-24]**. These results suggest that it is possible to use SE to follow changes in the $BaTiO_3$ films throughout the film processing. Thus, the optical properties and thickness of amorphous dried $BaTiO_3$ films were also studied by SE. In this experiment, eight layers of 2-methoxyethanol based $BaTiO_3$ solution (0.2M) were deposited on a freshly etched Si wafer. Si was chosen for this study due to its excellent surface smoothness and its stability over this temperature range. The SiO_2 was removed from the wafer surface by dipping the Si wafer in a small Teflon beaker with HF acid for 10 min. Then, the wafer was rinsed with deionized water and blown dry with N_2. The films were deposited on the wafer right after etching. After each layer deposition, the film was dried at different temperatures (200, 250, 300, 350^{o}C) for 5 min.

SE data from 350 to 700 nm were used in modeling. The best fit model structure of these films consisted of a bulk film with a thin layer of surface roughness. The sigma value decreased from 0.089 to 0.038 with increasing drying temperature. It is also noted that the 350^{o}C dried film shows no surface roughness. **Fig. 5.22** shows the best fit to the experimental data for the amorphous $BaTiO_3$ film on Si dried at 200^{o}C.

Fig. 5.23 shows the measured refractive index of each of the dried films. It can be seen that refractive index increases as the films are densified at higher drying temperatures. Accordingly, **Fig. 5.24** shows that the film thickness collapses from 5332.0±64.1 Å to 3642.0±8.1 Å after drying at 200^{o}C to 350^{o}C, respectively. This is

consistent with the observed decrease in thickness with increasing drying temperature, as measured by profilometry (See **Fig. 5.20**). In section 5.3.2, it was shown that weight loss due to large amount of organics occurs at this temperature range.

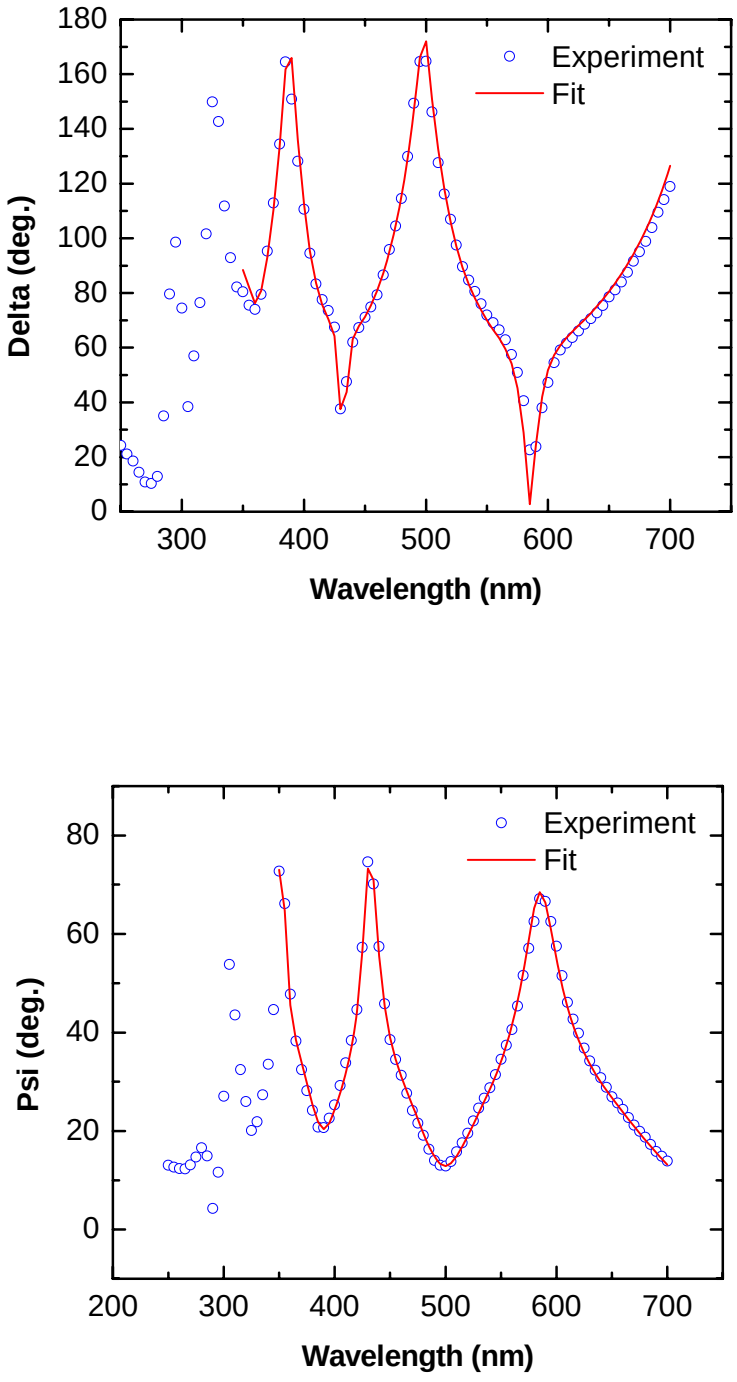

Fig. 5.22 Model fits compared to measured SE data for an amorphous $BaTiO_3$ film dried at 200°C on a silicon wafer (prepared from 0.2 M 2-methoxyethanol solution)

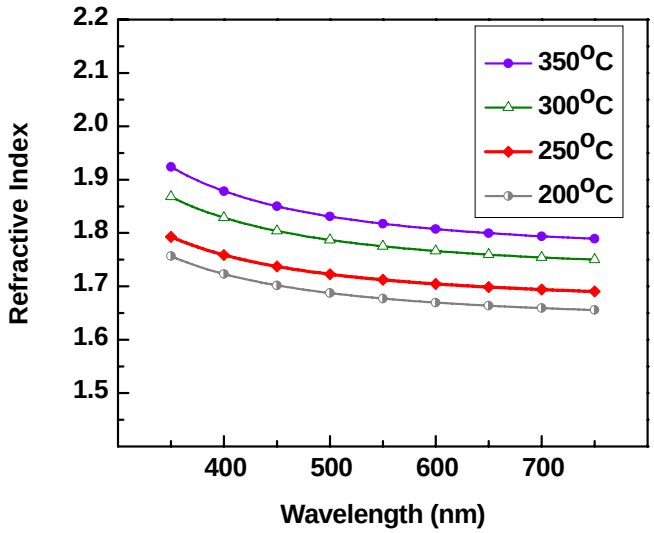

Fig. 5.23 Refractive index of dried amorphous $BaTiO_3$ films (prepared from a 0.2 M 2-methoxyethanol solution)

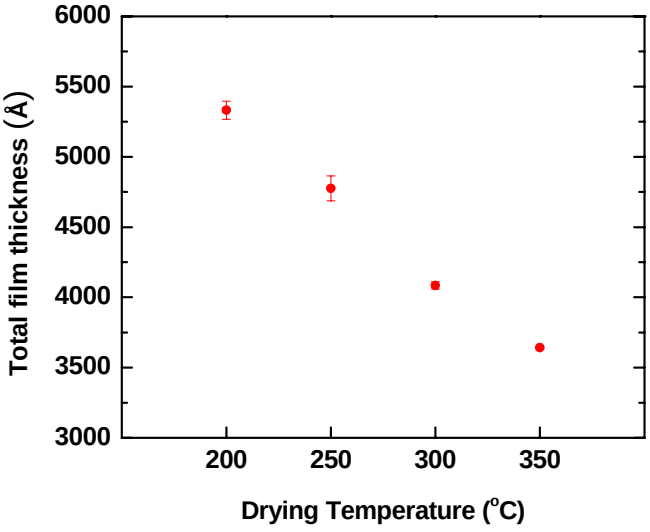

Fig. 5.24 Total thickness of amorphous $BaTiO_3$ films as a function of drying temperature (prepared from 0.2 M 2-methoxyethanol solutions)

5.4.2 $BaTiO_3$ films on sapphire substrates

To study the crystallization step, optical measurements were carried out on $BaTiO_3$ films on sapphire substrates. An Al_2O_3 (0001) single crystal was used as the substrate because it provides a stable surface which will not complicate SE modeling. In addition, the Al_2O_3 substrate has a small thermal expansion mismatch with $BaTiO_3$ up to at least 1000°C, giving crack-free films ($7.5x10^{-6}$/°C for Al_2O_3 and $9.8x10^{-6}$/°C **[25]** for $BaTiO_3$).

Thin films of ~2000 Å were prepared as described in section 3.1.1. The film was RTA'd at 750°C in N_2 flow. A SE measurement was performed after the RTA annealing step (750°C in N_2 flow). Then, SE data from the same film area were measured after the high temperature step (1000°C, 10^{-15} atm pO_2) and again after re-oxidation (600°, 10^{-6} atm pO_2). As shown in **Fig. 5.25**, there are clear changes in the interference fringes after the 1000°C step; however, no significant change was observed after re-oxidation. In all cases, the data were collected using an achromatic compensator to minimize instrumental errors.

Modeling of the SE data was done using reference data for (0001) Al_2O_3 and a Sellmeier oscillator for the optical properties of the $BaTiO_3$ film. In all cases, good results were obtained from data modeled between 375 and 750 nm with the absorption part of the oscillator fixed to zero. Because this is an all-transparent system, the SE data were modeled using Δ and Ψ, rather than $\tan\Psi$, $\cos\Delta$ for σ. This typically enables better fitting of the depth profiles, as discussed by Chindaudom **[26]**.

Initially, modeling was performed with a 2 layer structure consisting of a bulk film with some surface roughness. The 2 layer model resulted in σ values that are unacceptably large (2.24°-3.44°). Much lower sigma (0.69°-0.81°) and improved fits

were achieved when a low density layer was added at the film/substrate interface (See. **Fig. 5.26** and **Fig. 5.27)**.

EELS analysis (section 4.3) showed retained C distributed in a furnace annealed film (on Ni foil). Thus, attempts were made to model with the optical property data using a mixture of $BaTiO_3$ and graphitic carbon. The resulting fit did not provide a reasonable volume fraction of C, and was discarded.

The optical properties and depth profiles of the films at the three different stages in the processing are shown in **Fig. 5.28** and **Fig. 5.29**, respectively. Obviously, the results after 1000 °C and after re-oxidation show comparable refractive indices and film structures, suggesting that the re-oxidation step does not change the film substantially. The optical properties agree well with data for a ceramic sample with 95% density **[27]**, meaning the film annealed at 1000^{o}C is fully-crystallized and of reasonably high density. The RTA'd sample (750°C) shows a lower refractive index. **Fig. 5.30** shows a plot of the film thickness after each annealing step. It can be seen that there is some densification after the furnace annealing, although the change in thickness is within the 90% confidence limits. This suggests that the major increase in refractive index after furnace annealing may be due to further crystallization, rather than densification.

There is also a slight change in the film structure between RTA'd and 1000°C annealed films (see **Fig. 5.29**). It was necessary to fix the volume fraction of air at 50% in the surface roughness layer to obtain a reasonable best fit model for the RTA'd film. In contrast, varying the % air in the layer improves the fit for the furnace annealed film. The thickness of the surface roughness layer increases from 83.3±1.8 Å (with fixed 50% air) for the RTA'd film to 206 ± 16 Å (with 32±3% air) for the 1000^{o}C annealed film.

The larger surface roughness of furnace annealed films could be due to grain growth at high temperature. The result is consistent with the rough surface observed in the cross-sectional TEM sample in **Fig. 4.5** (section 4.2.2).

These results suggest that $BaTiO_3$ films with good densities can be achieved by CSD processing, and that SE can be used to depth profile them. Thus, work was subsequently undertaken to study $BaTiO_3$ films on Ni foils.

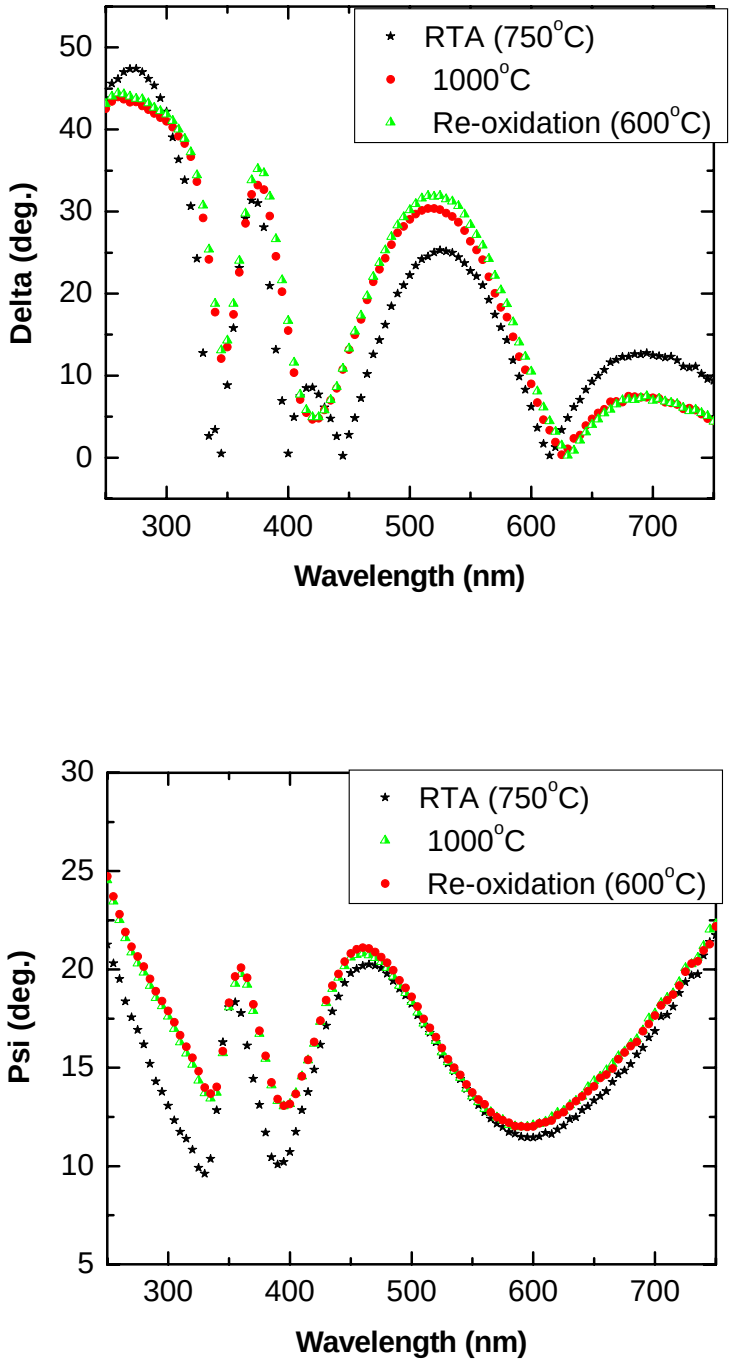

Fig. 5.25 Delta and psi as a function of wavelength at various points in the processing of a $BaTiO_3$ film on a (0001) Al_2O_3 substrate

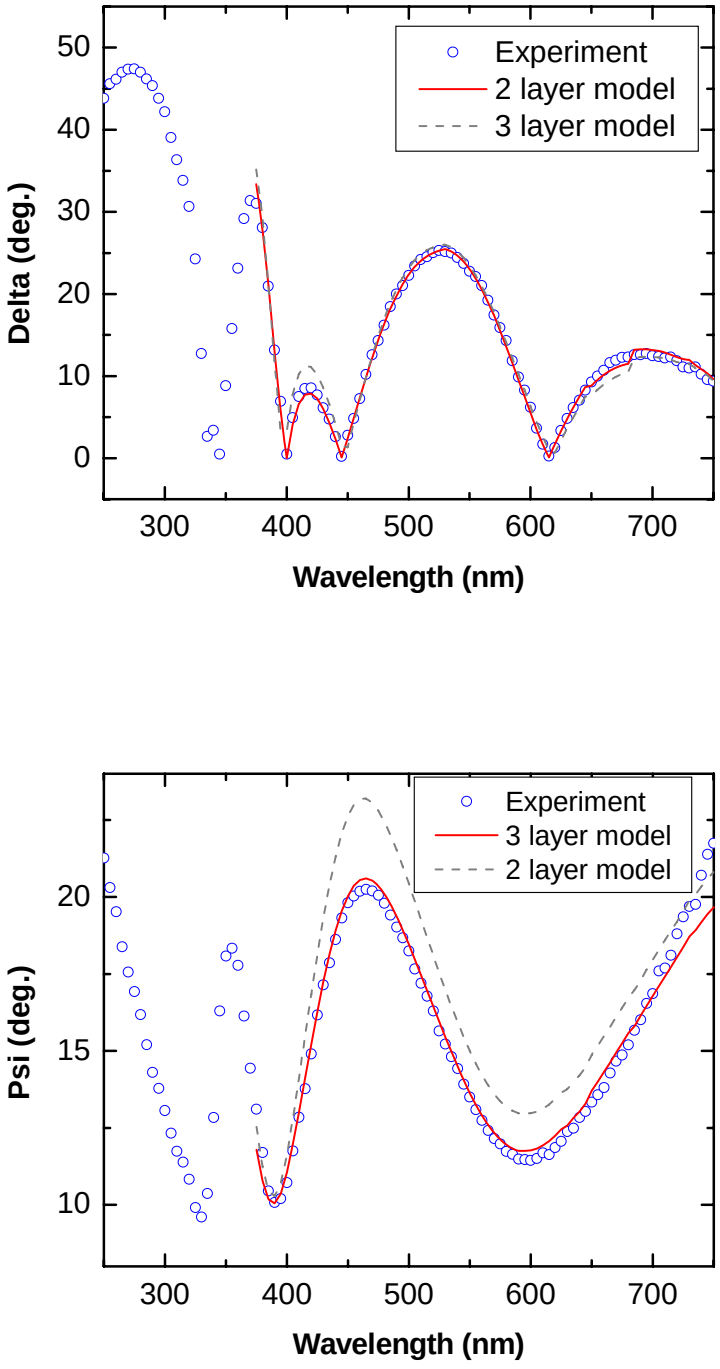

Fig. 5.26 Model fits with 2 layer (Al_2O_3/Osc/Osc+air) and 3 layer (Al_2O_3/Osc+air/Osc/Osc+air) model of 750^{o}C RTA'd $BaTiO_3$ film on (0001) Al_2O_3

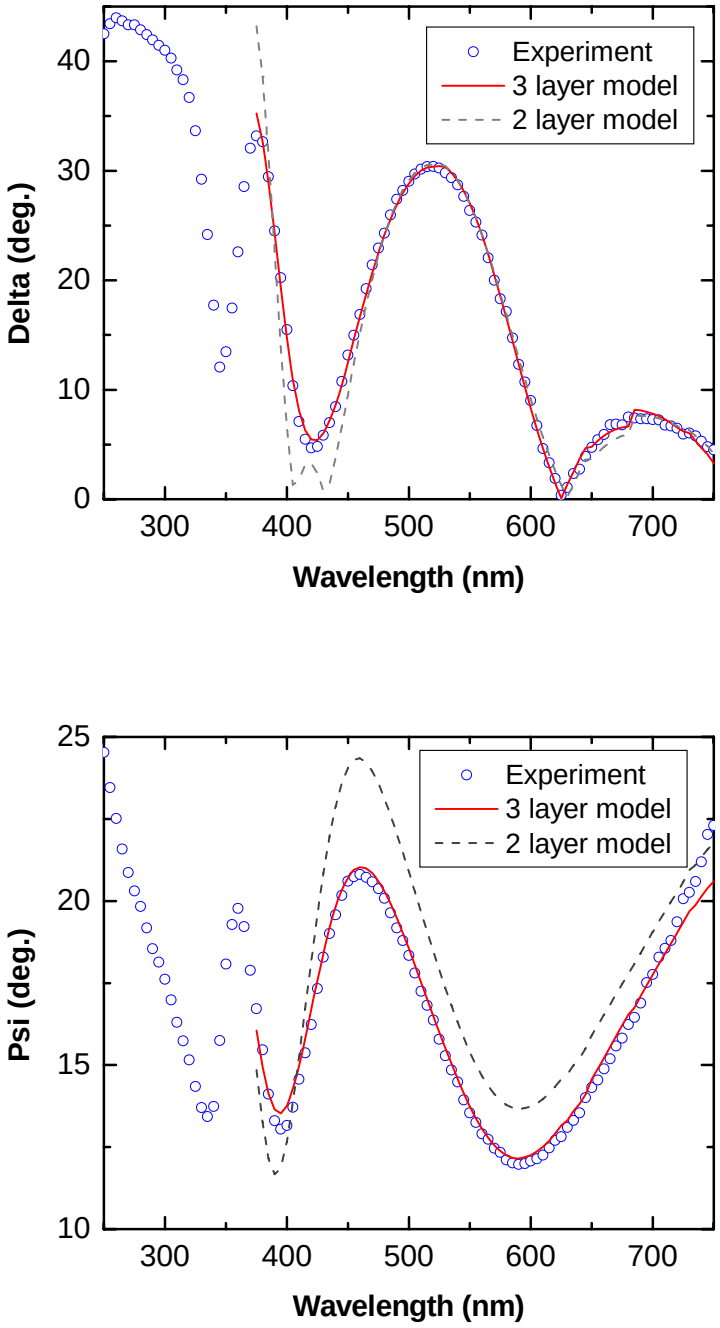

Fig. 5.27 Model fits with 2 layer (Al_2O_3/Osc/Osc+air) and 3 layer (Al_2O_3/Osc+air/Osc/Osc+air) model of 1000^{o}C furnace annealed $BaTiO_3$ film on (0001) Al_2O_3 (Note: Osc means Oscillator.)

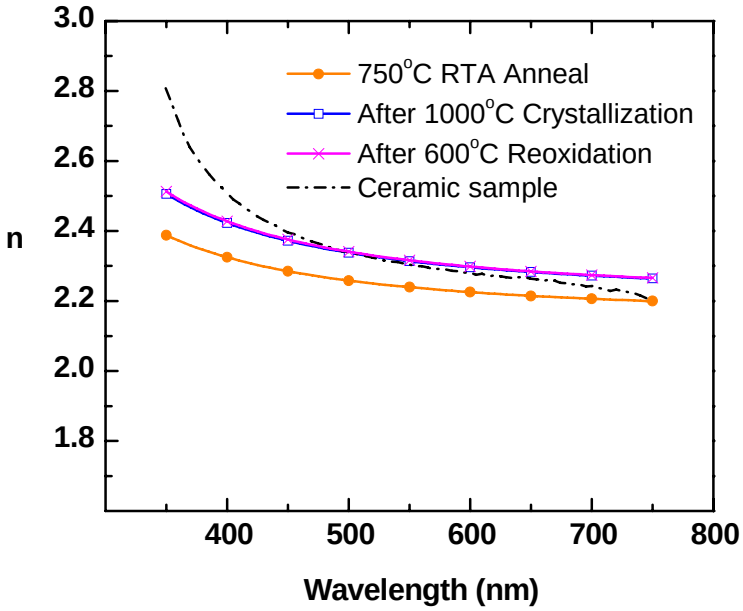

Fig. 5.28 Refractive index of RTA'd annealed, crystallized and re-oxidized $BaTiO_3$ films

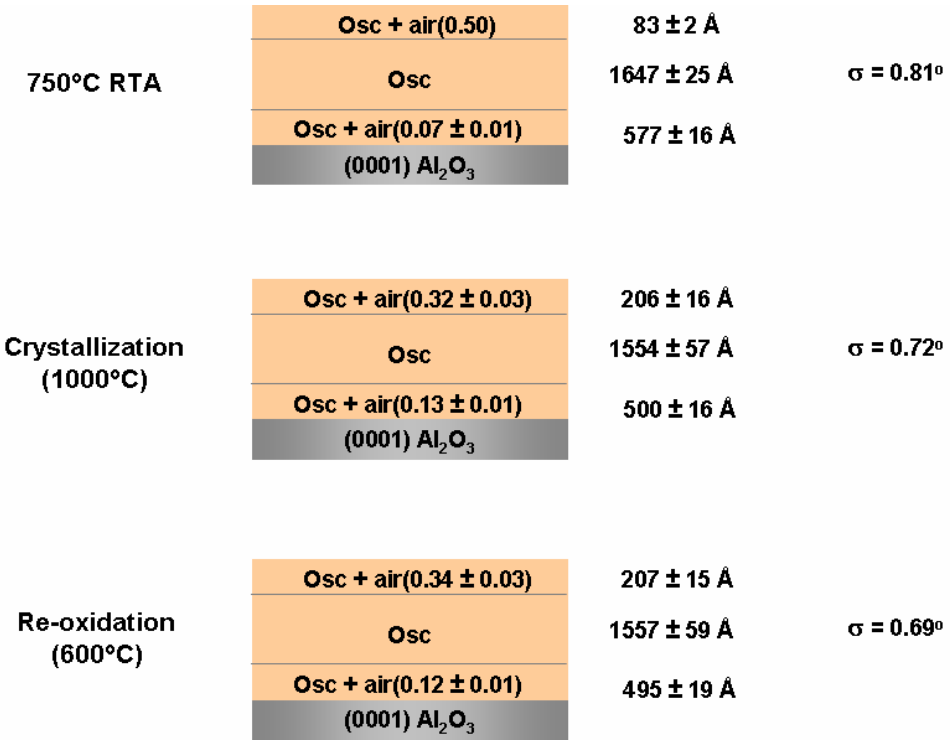

Fig. 5.29 Depth profiles of $BaTiO_3$ films on (0001) Al_2O_3 after each annealing.

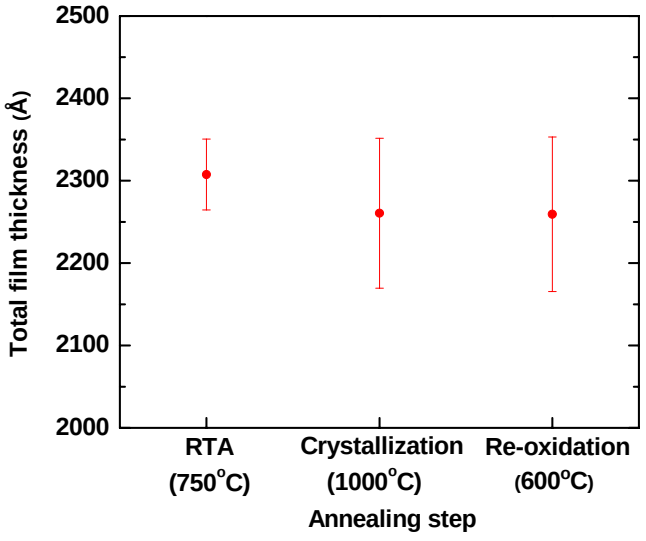

Fig. 5.30 Total thickness of $BaTiO_3$ films on (0001) Al_2O_3 after each annealing.

5.4.3 Optical properties of nickel oxide

In order to model the $BaTiO_3$/Ni interface, reference optical properties for the NiO must first be known. There have been many studies on the optical properties of nickel oxide **[1, 2, 28-33]**. The reported data in the visible range differ in both the refractive index and especially the extinction coefficient (k), as shown in **Fig. 5.31.** Powell et al. **[28]** showed that a flame fusion grown NiO single crystal (SC) is transparent for wavelengths above 400 nm. Later work by Franta et al. **[33]** for pulse laser deposited NiO films is in good agreement for the extinction coefficient, although a slightly lower refractive index was obtained (possibly because of a lower density). The near-zero extinction coefficient of both samples suggests they are stoichiometric NiO (which is normally green in color). Lopez et al. **[2]** studied the optical properties of thermally oxidized NiO films by spectroscopic ellipsometry. In their work, sputtered Ni films were oxidized in air at temperatures ranging from 389-580^{o}C. The optical properties of the films were grouped according to grain size, as shown in **Fig. 5.31**. The difference in extinction coefficient of the films may also be due to a variation in the amount of O in the NiO film. Lu et al. showed a strong dependence of the transmittance on the O_2/Ar ratio used during RF reactive magnetron sputtering of NiO films **[31]**.

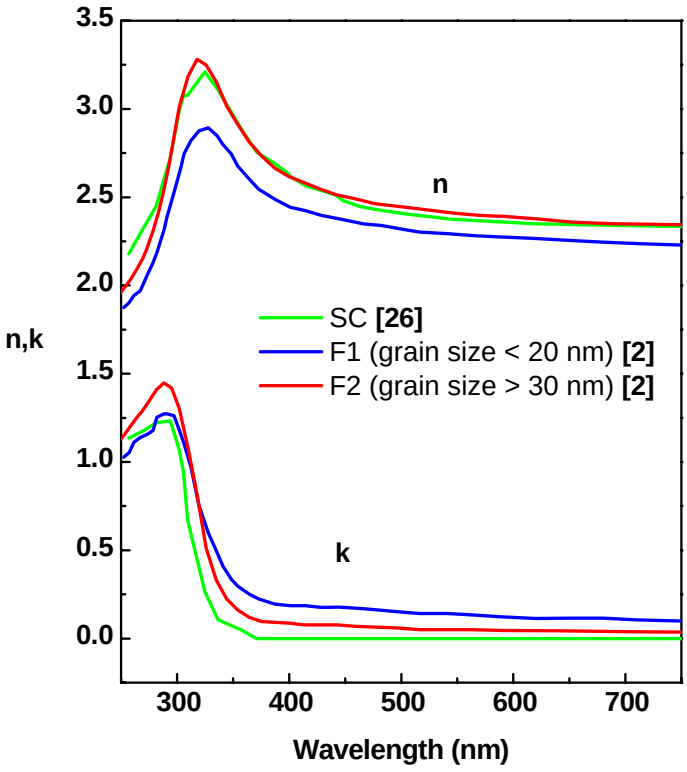

Fig. 5.31 Optical properties of a NiO single crystal (SC) and NiO films of different grain size (F1 and F2)

In section 5.1, initial results on the oxidation of Ni foils were presented. To further clarify the optical properties of the NiO (to enable a more quantitative optical evaluation of the Ni/$BaTiO_3$ interface) additional work was performed. In this experiment, the optical properties of thermally grown NiO on high purity Ni foils were studied by spectroscopic ellipsometry. To obtain more accurate optical constants, films at least 800 Å thick were used. For this purpose, a NiO film was prepared by annealing

the Ni foil at 600^{o}C in 10^{-6} atm pO_2 for 1 hr. A Sellmeier oscillator (Osc) was used to describe the optical properties of any NiO present.

The SE data were modeled using two structures 1) Ni/Osc/Osc+air) and 2) Ni/Osc+Ni/Osc+air. **Fig. 5.32** shows that model with Ni/Osc+Ni/Osc+air gave a better fit in psi values. Room temperature Ni optical properties (See section 5.1) were used for the Ni foil as they provided a better fit and a lower sigma value. The ~7% Ni mixed in the bulk of the NiO layer implied two possibilities. The "Ni" either represents the surface roughness of the Ni foil or it is simply a means of describing the absorption of the NiO film. Given that the mixed layer is quite thick (717.6±26.2 Å) compared to the total film thickness (850.6±43.4 Å), the latter possibility is more likely. Single term Sellmeier oscillators do not always describe absorption well across a wide wavelength range. Thus, the "Ni" in the layer does not necessarily imply the existence of metallic Ni in the film.

The net optical properties of the NiO film were calculated using Bruggeman effective medium theory (Eq. 3.15) and are shown in **Fig. 5.33**. It can be seen that the optical properties determined here agree well with data for thermally oxidized NiO films from Lopez et al.'s work **[2]**. Consequently, the optical properties of the thermally grown NiO film (Osc+Ni) was used to described any NiO in $BaTiO_3$ films on high purity Ni foils. **Fig. 5.34** shows a comparison of the optical properties of the thermally grown NiO film on Ni foil from this experiment and a 95% dense $BaTiO_3$ ceramic. The primary difference between the two is in the imaginary part of the dielectric function.

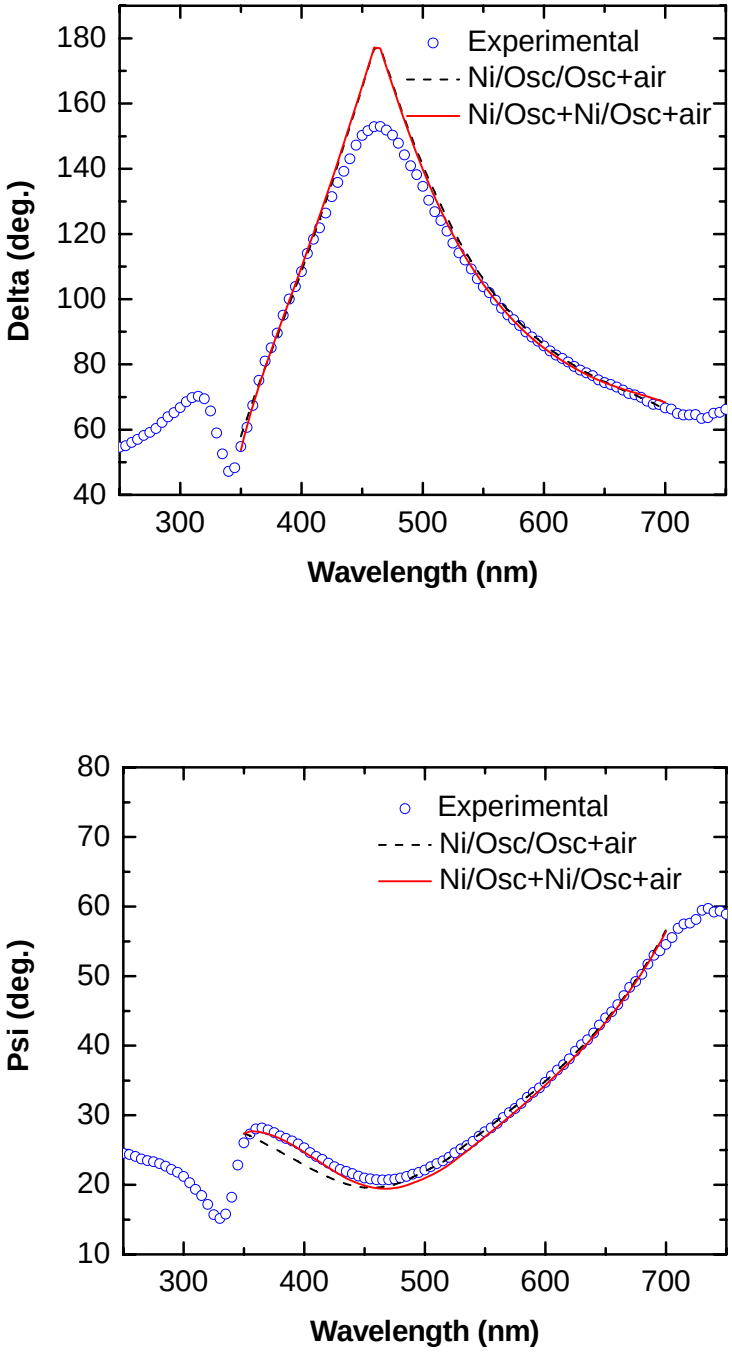

Fig. 5.32 Model fits of NiO thermally grown on high purity Ni foil at 600^{o}C

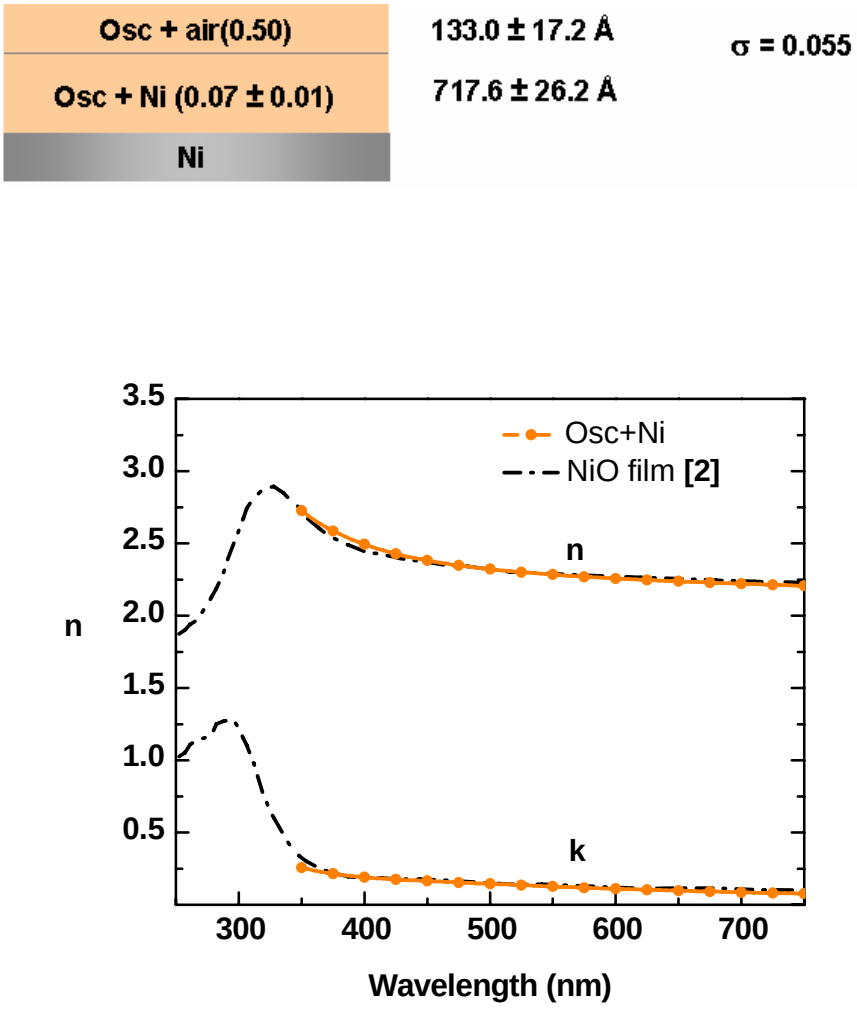

Fig. 5.33 Depth profile and refractive index of NiO thermally grown at 600^{o}C

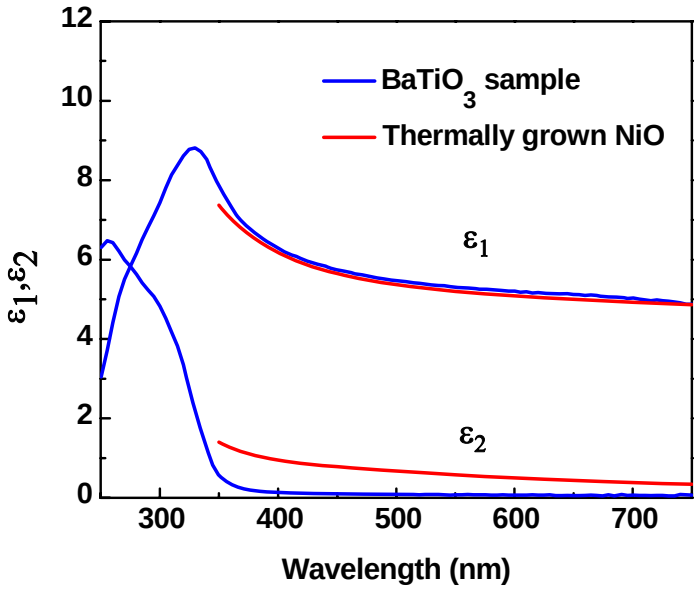

Fig. 5.34 Dielectric function of the thermally grown NiO and a $BaTiO_3$ ceramic sample

5.4.4 $BaTiO_3$ films on Ni foil

The depth profiles and optical properties of $BaTiO_3$ films (on Ni foil) RTA'd at different temperatures (600-750^{o}C) were studied by spectroscopic ellipsometry (SE). Modeling of SE data was performed using reference data for the thermally grown NiO (i.e. the data measured in this work for NiO on Ni foil, see section 5.4.3) and a Sellmeier oscillator to describe the optical properties of NiO and $BaTiO_3$, respectively. In most cases, the best fit was obtained when the absorption in the oscillator was zero. Room temperature Ni reference data (see section 5.1) were chosen to describe the optical properties of the Ni foil because it improves the fit overall. SE data were truncated to 350-650 nm to obtain reasonable models.

SE data of a $BaTiO_3$ film on Ni foil RTA'd at 750^oC was first modeled with various possible film structures, which at least consist of a bulk layer and surface roughness. It was found that an interface layer of either (oscillator+Ni) or pure NiO near the substrate results in good fits to the experimental data (see **Fig. 5.35**) and similar sigma values were obtained (i.e. 0.081 for mix of oscillator and Ni and 0.078 for pure NiO). It is noted that the $BaTiO_3$ film refractive index extracted from both models is the same and comparable to that of a $BaTiO_3$ ceramic sample. The large sigma is again mainly due to error in the experimental data when delta is close to 0 and 180°.

Although the model with a NiO interface shows a slightly better fit for this specific film, the resulting depth profile is not realistic (See **Fig. 5.36)**. The thickness of the $BaTiO_3$ film is 1026.6±65.3 Å, which is approximately half of the total thickness of the film with the same number of spin-coated layers (8 layer) on (0001) Al_2O_3. In addition, the NiO layer is quite thick (902.9±49 Å), which is in disagreement with the fact that XRD did not detect NiO peak on this same film (see **Fig. 5.13**). As was described in section 5.4.3, the refractive indices of $BaTiO_3$ and NiO are quite similar. Thus, it is believed that the "NiO" is simply an artifact created by the model's attempts to create a slightly more optically lossy $BaTiO_3$ film. A similar situation also occurred on modeling other RTA'd films. Thus, it is believed that the model without NiO at the interface is correct for all RTA'd films. It might be useful in the future to conduct a comparable set of measurements on either an ellipsometer with a rotating compensator or a photoelastic modulator to remove the errors where Δ is near 0 or 180° to see if that enabled a clearer distinction on the presence of interfacial NiO.

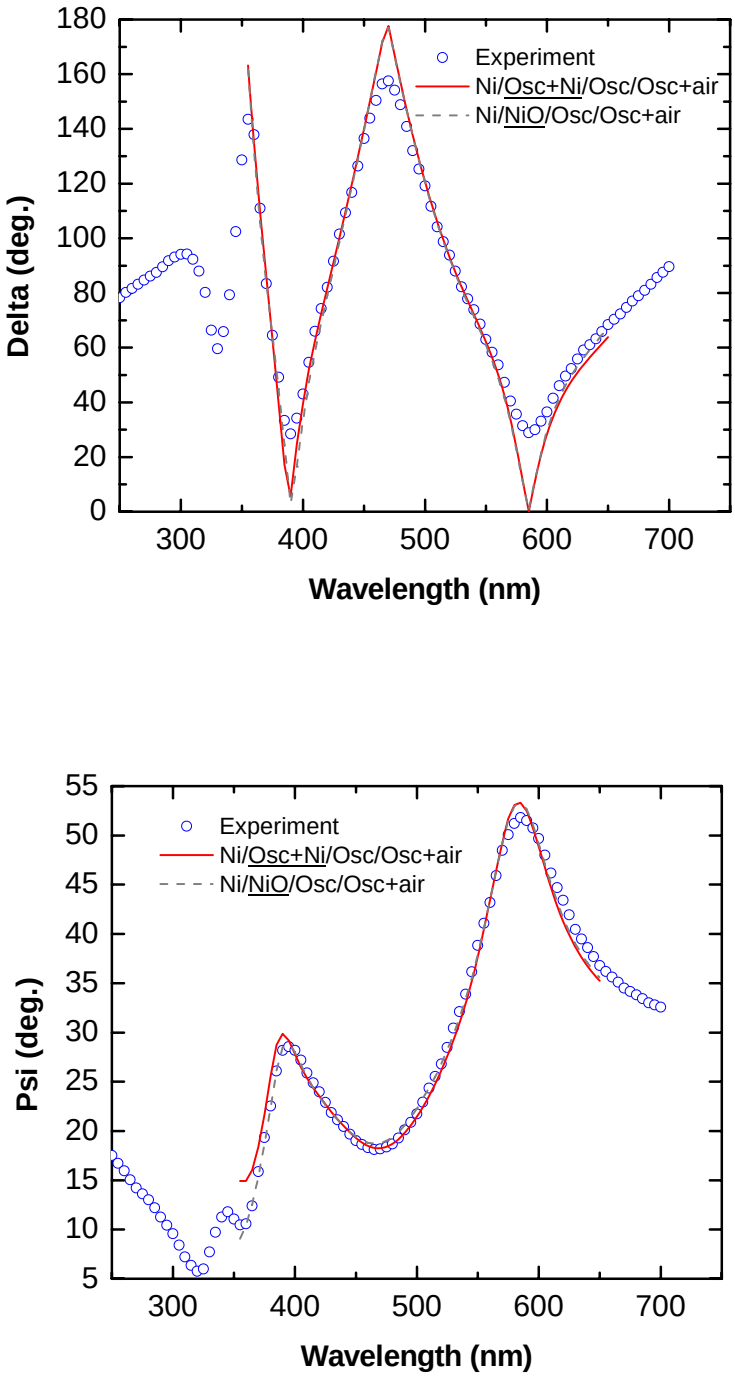

Fig. 5.35 Model fits of 750°C RTA'd $BaTiO_3$ film on high purity Ni foil

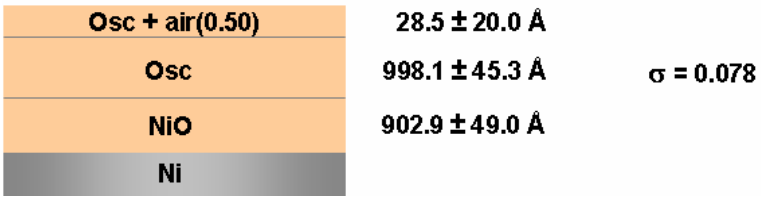

Fig. 5.36 Unreasonable film structure of RTA'd $BaTiO_3$ film on high purity Ni foil when modeled with NiO

It was found that modeling without NiO results in a more sensible film structure. **Fig. 5.37** shows that the total thickness of the 750°C RTA'd $BaTiO_3$ is 1984 ±242 Å. At the film substrate/interface film there is a 343.±106 Å thick layer with 9±5 volume % of Ni mixed in the $BaTiO_3$ film. The thickness of this layer agrees well with the rms roughness (37 nm) of the pre-annealed Ni foil, suggesting that this layer is due, at least in part, to the surface roughness of the Ni foil. In contrast to bare Ni, SE is able to detect the surface roughness of the Ni foil better with a transparent (insulating) film on the surface. The best fit without a NiO interface agrees well with the XRD results and cross-sectional TEM studies on RTA'd annealed films, which showed no detectable NiO.

Depth profiles for the best fit models of $BaTiO_3$ films RTA'd at other temperatures modeled without NiO are shown in **Fig. 5.37**. All show a reasonable volume fraction of Ni and thickness of the mixed layer near the substrate. It is noted that the 600°C RTA'd film does not show surface roughness on the $BaTiO_3$, suggesting that the majority of the surface roughness develops at higher temperatures. **Fig. 5.38** and **Fig. 5.39** show the refractive index and total thickness of $BaTiO_3$ films RTA'd at different temperatures. It can be seen that as the RTA temperature increases, further densification

and film crystallization occur, resulting in a higher refractive index for the $BaTiO_3$ film. The film thickness decreases after annealing at 600°C or 650°C and becomes stable above 700°C.

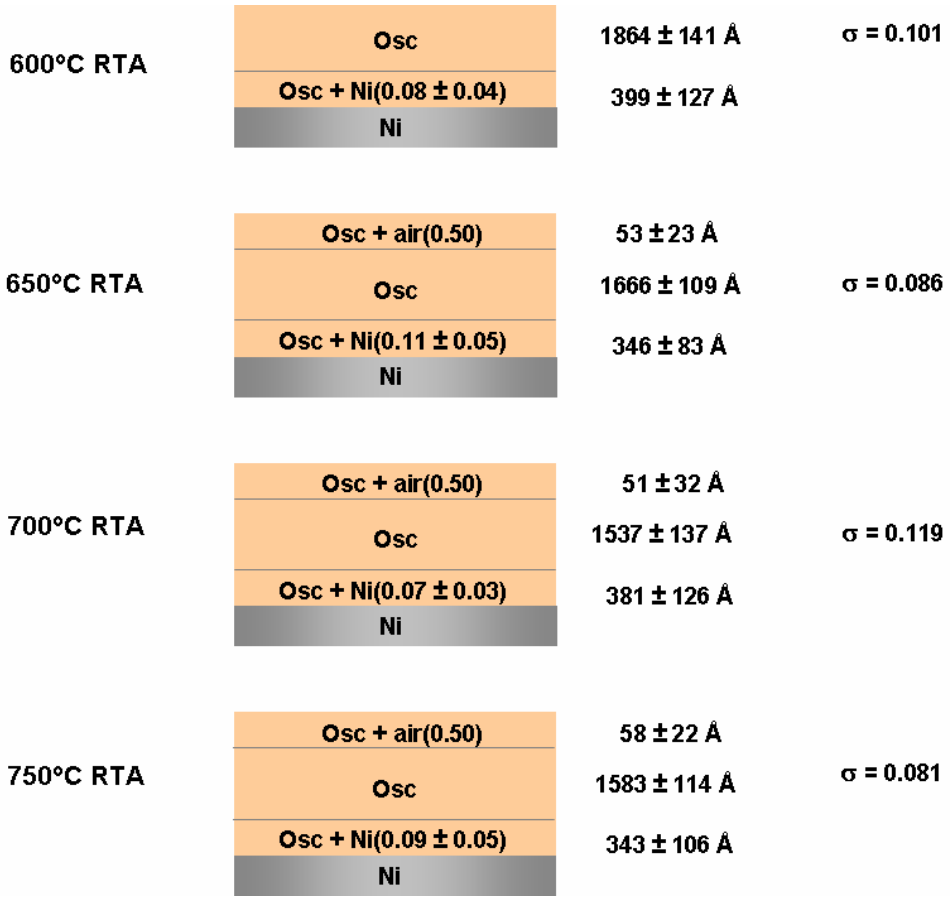

Fig. 5.37 SE model details of $BaTiO_3$ films on Ni foil RTA'd at temperature from 600-750°C

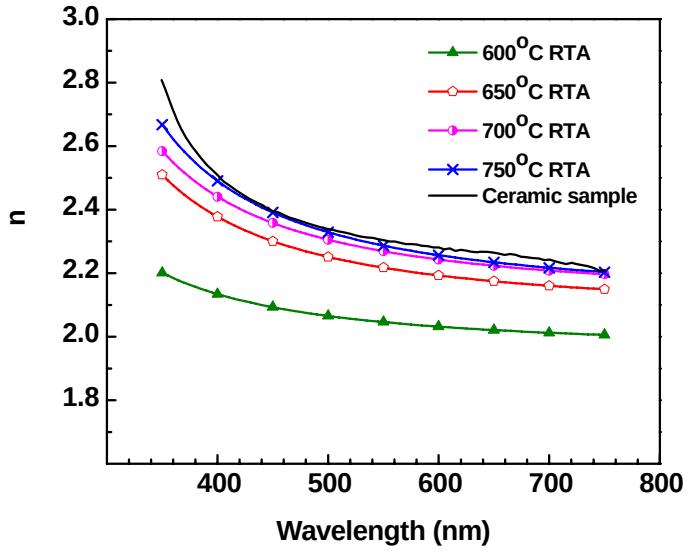

Fig. 5.38 Refractive index of RTA'd $BaTiO_3$ films on high purity Ni foil

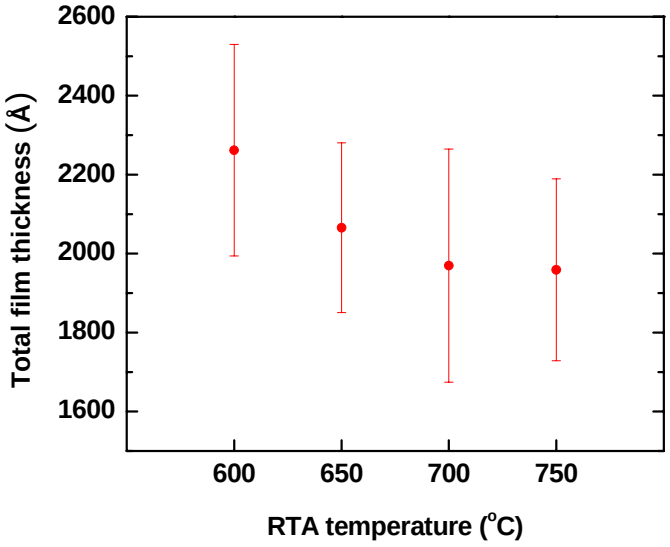

Fig. 5.39 Total thickness determined by SE for $BaTiO_3$ films on high purity Ni foil as a function of RTA temperature

5.5 Electrical properties of $BaTiO_3$ films on Ni foil

Dielectric property measurements as a function of frequency and temperature were performed on $BaTiO_3$ films on Ni foils. The dielectric properties and its relationship to structure and microstructure are also discussed.

Fig. 5.40 shows the room temperature dielectric constant as a function of frequency for furnace annealed $BaTiO_3$ films on Ni foils. The films were RTA'd at different temperatures (600-750^oC) before crystallization (1000^oC, 10^{-16} atm pO_2) and re-oxidation (600^oC, 10^{-6} atm pO_2). The dielectric constants of each film were measured from 30 spots because there was some variation. It is suspected that the variation could be due to film thickness, variable surface roughness of the foil, porosity and grain size.

The films show very high loss at low frequency (<1 kHz) due to space charge polarization and DC conduction. The average dielectric constants at 10 kHz of 750 and 650C'd RTA film are similar and approximately 1100 and 1160, respectively. The films RTA'd at 600^oC and 700^oC show relatively lower dielectric constants (880 and 950), respectively. This could be a result of differences in the grain size, porosity, and solution aging as discussed in section 5.3.1. The films RTA'd at 600^oC and 650^oC have similar grain size but the 600^oC RTA film contains more porosity. Thus, it has a lower dielectric constant. The film RTA'd at 700^oC shows a slightly higher porosity and smaller grain size, compared to the 750^oC RTA film. The loss tangent at 10 kHz of all film is less than 2%. The apparent increase in the loss tangent at high frequencies is due to an RC resonance and is not characteristic of the film.

Overall, the dielectric constant of these films is somewhat lower than those reported previously for $BaTiO_3$ films on metal foil ($\varepsilon_r \sim 2500$ **[34]** and $\varepsilon_r \sim 1300$ **[3]**) and

highly oriented (Ba,Sr)TiO_3 film on Ni foil (ε_r ~ 1500 **[35]**). The lower dielectric constant could be due to microstructure. It was shown that these films contain some porosity due to incomplete organic removal in the RTA under low pO_2.

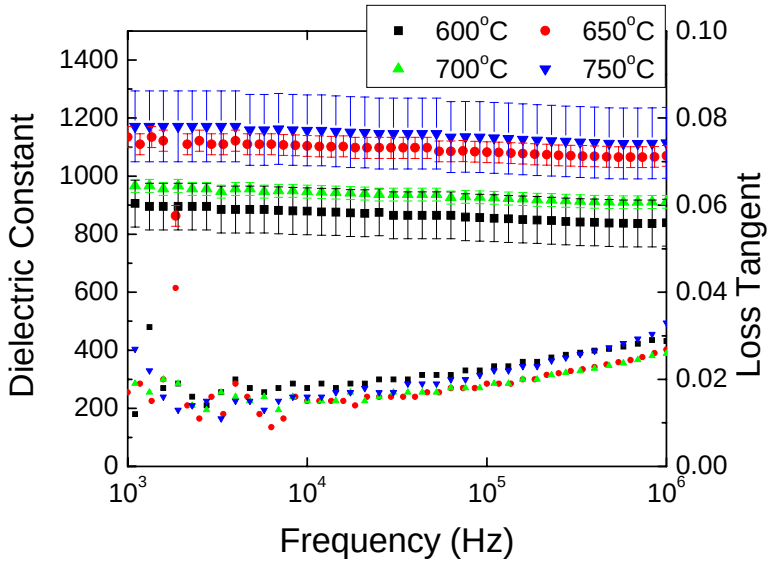

Fig. 5.40 Frequency dependence of dielectric constant and loss tangent furnace annealed $BaTiO_3$ films on Ni foil

The temperature dependence of dielectric constant was measured for $BaTiO_3$ films on a smoother Kodak Ni foil that became available at the very end of this work. After an RTA at 750°C in N_2, the film was crystallized at 1000°C for 1 h in 10^{-12} atm pO_2 and then re-oxidized at 600°C for 30 min in 10^{-6} atm pO_2. The RTA'd film show a room temperature dielectric constant (at 10 kHz) of 375 with a loss tangent of 4%. The furnace annealed and reoxidized film shows a dielectric constant of 1300 with <2% loss tangent.

The temperature dependence of the permittivity for the RTA'd film in **Fig. 5.41** is highly dispersive. This could be due to incomplete densification of residual organics in the film after the RTA step, as was discussed in section 5.3.2. The furnace annealed film is less dispersive. There is a shallow maximum in the permittivity above 100°C which suggests that tetragonal-cubic phase transition in the films.

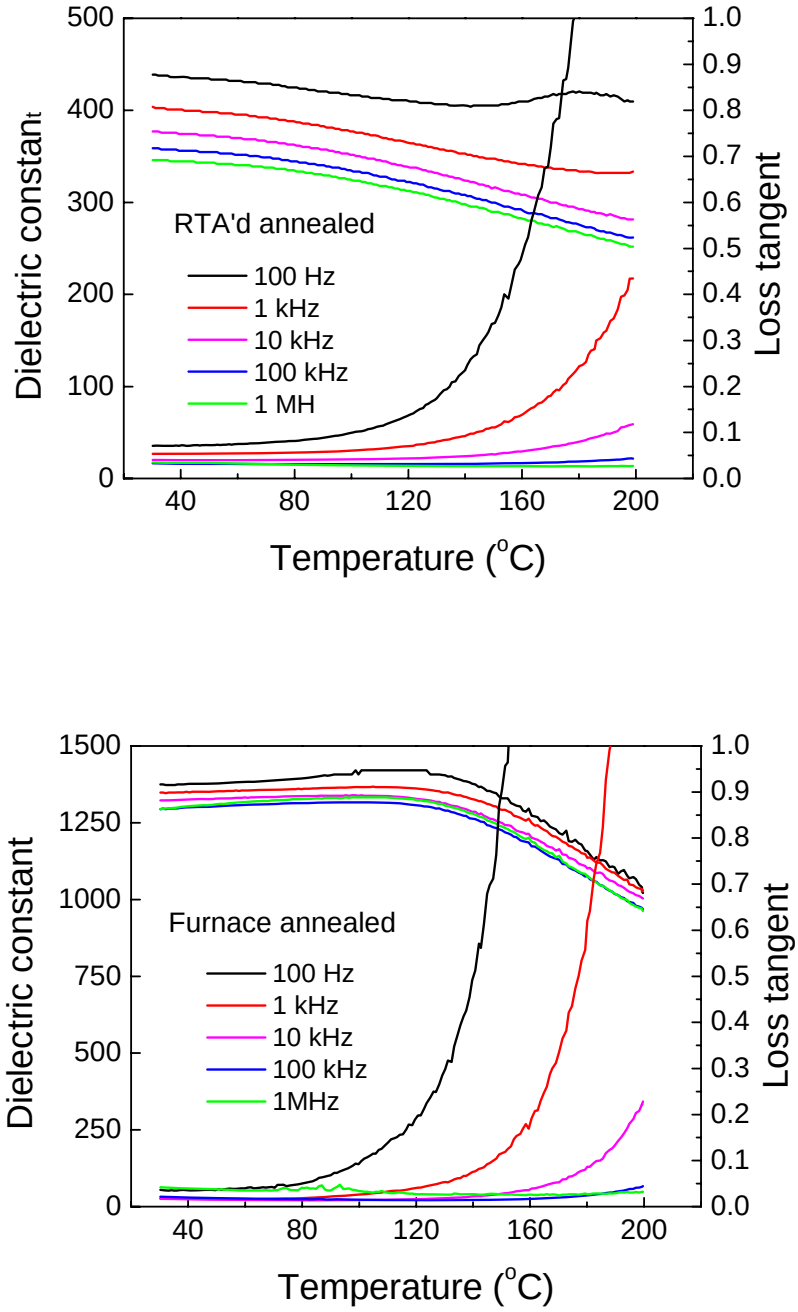

Fig. 5.41 Temperature dependence of dielectric constant and loss tangent of 750°C RTA'd and furnace annealed $BaTiO_3$ films on (Kodak) Ni foil

References

[1] J. A. Lafemina. "Optical Properties of Nickel Oxide," M.S. Thesis, The Pennsylvania State University, 1979.

[2] A. M. Lopez-Beltran and A. Mendoza-Galvan, "The Oxidation Kinetics of Nickel Thin Films Studied by Spectroscopic Ellipsometry," *Thin Solid Films*, **503** [1-2], 40-44 (2006).

[3] H. Nagata, S. W. Ko, E. Hong, C. A. Randall and S. Trolier-McKinstry, "Microcontact Printed $BaTiO_3$ and $LaNiO_3$ Thin Films for Capacitors," *Journal of the American Ceramic Society*, **89** [9], 2816-2821 (2006).

[4] W. W. Mullins, "Theory of Thermal Grooving," *Journal of Applied Physics*, **28** [3], 333-339 (1957).

[5] Srinivas Sr and R. Trivedi, "Theory of Grain-Boundary Grooving under Combined Action of Surface and Volume Diffusion Mechanisms," *Acta Metallurgica*, **21** [5], 611-620 (1973).

[6] M. H. Frey and D. A. Payne, "Synthesis and Processing of Barium-Titanate Ceramics from Alkoxide Solutions and Monolithic Gels," *Chemistry of Materials*, **7** [1], 123-129 (1995).

[7] P. Duran, D. Gutierrez, J. Tartaj, M. A. Banares and C. Moure, "On the Formation of an Oxycarbonate Intermediate Phase in the Synthesis of $BaTiO_3$ from (Ba,Ti)-Polymeric Organic Precursors," *Journal of the European Ceramic Society*, **22** [6], 797-807 (2002).

[8] S. Kumar, G. L. Messing and W. B. White, "Metal-Organic Resin Derived Barium-Titanate.1. Formation of Barium Titanium Oxycarbonate Intermediate," *Journal Of the American Ceramic Society*, **76** [3], 617-624 (1993).

[9] S. Hoffmann and R. Waser, "Control of the Morphology of CSD-Prepared (Ba,Sr)TiO_3 Thin Films," *Journal of the European Ceramic Society*, **19** [6-7], 1339-1343 (1999).

[10] V. Ischenko, E. Pippel, R. Koferstein, H. P. Abicht and J. Woltersdorf, "Barium Titanate via Thermal Decomposition of Ba,Ti-Precursor Complexes: The Nature of the Intermediate Phases," *Solid State Sciences*, **9** [1], 21-26 (2007).

[11] G. W. Scherer, "Sintering of Sol-gel Films," *Journal of Sol-gel Science and Technology*, **8** [1-3], 353-363 (1997).

[12] B. Lee and J. P. Zhang, "Preparation, Structure Evolution and Dielectric Properties of $BaTiO_3$ Thin Films and Powders by an Aqueous Sol-gel Process," *Thin Solid Films*, **388** [1-2], 107-113 (2001).

[13] C. L. Mao, X. F. Dong and T. Zeng, "Synthesis and Characterization of Nanocrystalline Barium Strontium Titanate Powders Prepared by Citrate Precursor Method," *Materials Letters*, **61** [8-9], 1633-1636 (2007).

[14] M. Veith, S. Mathur, N. Lecerf, V. Huch, T. Decker, H. P. Beck, W. Eiser and R. Haberkorn, "Sol-gel Synthesis of Nano-scaled $BaTiO_3$, $BaZrO_3$ and $BaTi_{0.5}Zr_{0.5}O_3$ Oxides via Single-source Alkoxide Precursors and Semi-alkoxide Routes," *Journal of Sol-gel Science and Technology*, **17** [2], 145-158 (2000).

[15] D. E. McCauley, M. S. H. Chu and M. H. Megherhi, "PO_2 Dependence of the Diffuse-phase Transition in Base Metal Capacitor Dielectrics," *Journal of the American Ceramic Society*, **89** [1], 193-201 (2006).

[16] A. Manso-Silvan, L. Fuentes-Cobas, R. J. Martin-Palma, M. Hernandez-Velez and J. M. Martinez-Duart, "$BaTiO_3$ Thin Films Obtained by Sol-gel Spin Coating," *Surface & Coatings Technology*, **151**, 118-121 (2002).

[17] Y. Badr, A. Salah and I. K. Battisha, "Effect of Europium Ion Concentrations on the Photoluminescence Emission of Nano-crystalline $BaTiO_3$ Prepared by Sol-gel Technique," *Journal of Sol-Gel Science and Technology*, **34** [3], 219-226 (2005).

[18] G. E. Jellison, L. A. Boatner, D. H. Lowndes, R. A. McKee and M. Godbole, "Optical Functions And Transparent Thin-Films Of $SrTiO_3$, $BaTiO_3$, and SiO_x Determined by Spectroscopic Ellipsometry," *Applied Optics*, **33** [25], 6053-6058 (1994).

[19] A. Ianculescu, M. Gartner, B. Despax, V. Bley, T. Lebey, R. Gavrila and M. Modreanu, "Optical Characterization and Microstructure of $BaTiO_3$ Thin Films Obtained by RF-magnetron Sputtering," *Applied Surface Science*, **253** [1], 344-348 (2006).

[20] Z. M. Huang, J. Q. Xue, Y. J. Ge, J. H. Qin, Y. Hou, J. H. Chu and D. H. Zhang, "Temperature Dependence of $BaTiO_3$ Infrared Dielectric Properties," *Applied Physics Letters*, **88** [21], (2006).

[21] T. Tsurumi, T. Harigai, D. Tanaka, H. Kakemoto and S. Wada, "Anomalous Dielectric and Optical Properties in Perovskite-type Artificial Superlattices," *Science and Technology of Advanced Materials*, **5** [4], 425-429 (2004).

[22] Z. G. Hu, G. S. Wang, Z. M. Huang and J. H. Chu, "Structure-related Infrared Optical Properties of $BaTiO_3$ Thin Films Grown on Pt/Ti/SiO_2/Si Substrates," *Journal of Physics and Chemistry of Solids*, **64** [12], 2445-2450 (2003).

[23] K. Pita, S. D. Cheng, C. H. Kam, Y. Zhou, Y. L. Lam and Y. C. Chan, "The Crystallinity, the Surface Morphology and the Optical Constant of Sol-gel Derived Thin Films of $BaTiO_3$ on SiO_2/Si and Si Substrates," *Ferroelectrics*, **231** [1-4], 655-660 (1999).

[24] M. Nenkov and T. Pencheva, "Investigation of Inhomogeneity of $BaTiO_3$ Thin Films using Transmittance Spectra Measurements," *Thin Solid Films*, **324** [1-2], 305-310 (1998).

[25] B. Jaffe, W. R. Cook Jr. and H. Jaffe, *Piezoelectric Ceramics*. Academic Press: 1971.

[26] P. Chindaudom. "Characterization of Inhomogeneous Transparent Thin Films on Transparent Substrates by Spectroscopic Ellipsometry," Ph.D. Thesis, The Pennsylvania State University, University Park, 1991.

[27] M. Biegalski and S. Trolier-McKinstry, "Modeling Optical Changes in Perovskite Capacitor Materials Due to DC-Field Degradation," *Journal of the American Ceramic Society*, **88** [1], 71-78 (2005).

[28] R. J. Powell and W. E. Spicer, "Optical Properties of NiO and CoO," *Physical Review B*, **2** [6], 2182-& (1970).

[29] K. M. E. Miedzinska, B. R. Hollebone and J. G. Cook, "Optical-properties and Assignment of the Absorption-spectra of Sputtered Mixed-valence Nickel-oxide Films," *Journal of Physics and Chemistry of Solids*, **49** [11], 1355-1362 (1988).

[30] M. G. Krishna and A. K. Bhattacharya, "Quantum Confinement Effects on the Optical Properties of Ion Beam Sputtered Nickel Oxide Thin Films," *International Journal of Modern Physics B*, **15** [2], 191-200 (2001).

[31] Y. M. Lu, W. S. Hwang, J. S. Yang and H. C. Chuang, "Properties of Nickel Oxide Thin Films Deposited by RF Reactive Magnetron Sputtering," *Thin Solid Films*, **420**, 54-61 (2002).

[32] R. Newman and R. M. Chrenko, "Optical Properties of Nickel Oxide," *Physical Review*, **114** [6], 1507-1513 (1959).

[33] D. Franta, B. Negulescu, L. Thomas, P. R. Dahoo, M. Guyot, I. Ohlidal, J. Mistrik and T. Yamaguchi, "Optical Properties of NiO Thin Films Prepared by Pulsed Laser Deposition Technique," *Applied Surface Science*, **244** [1-4], 426-430 (2005).

[34] J. Ihlefeld, B. Laughlin, A. Hunt-Lowery, W. Borland, A. Kingon and J. P. Maria, "Copper Compatible Barium Titanate Thin Films for Embedded Passives," *Journal of Electroceramics*, **14** [2], 95-102 (2005).

[35] J. T. Dawley and P. G. Clem, "Dielectric Properties of Random and < 100 > Oriented $SrTiO_3$ and $(Ba,Sr)TiO_3$ Thin Films Fabricated on < 100 > Nickel Tapes," *Applied Physics Letters*, **81** [16], 3028-3030 (2002).

Chapter 6

Conclusions and Future Work

This thesis has shown the use of different characterization techniques, i.e. X-ray diffraction, transmission electron microscopy, and spectroscopic ellipsometry to characterize the phase purity, microstructure, and interface quality of barium titanate thin films on Ni foil. In addition, organic decomposition during low oxygen pressure processing was also investigated. The conclusions of this work are described in section 6.1. The recommended future work is included in section 6.2.

6.1 Conclusions

Barium titanate thin films were deposited on Ni foils by chemical solution deposition. Drying and pyrolysis of the deposited films were performed on a hot plate in air. The deposited films were pre-annealed in a RTA at 600-750^{o}C with an intermediate pyrolysis at 350^{o}C in flowing N_2. Then, a high temperature heat-treatment (at 1000^{o}C) and re-oxidation (600^{o}C) were done in a reducing furnace. The resulting films have dielectric constants of 1000-1300 which are stable as a function of temperature, with loss tangents less than 2%. The average grain size of furnace annealed (1000^{o}C) films is 42 nm. The low oxygen partial pressure during the heat treatment was suspected to be the reason for such a small grain size. There are 5-6 grains across the thickness of a 200 nm thick film, which will provide grain boundaries to help block the migration of oxygen vacancies through the barium titanate.

NiO was not found in the films until the re-oxidation step. While NiO was detected in X-ray diffraction scans, it was not observed in cross-sectional TEM. Thus, it is believed that the NiO is not uniform and is spatially distributed in the films. It was found that there is a 5-8 nm thick Ni-Ba alloy interfacial layer on the Ni foil surface in the furnace annealed films.

Since high temperature annealing of the films was performed at low oxygen partial pressures, organic decomposition for both powders dried from barium titanate solutions and barium titanate films was studied. It was shown that complete decomposition of organics in N_2 flow is extended to higher temperatures, compared to that in air. Thus, when fast heating rates are used, as in an RTA ($10^oC/s$), residual carbon is expected. The retained organics can cause porosity development during the high temperature annealing. The presence of residual organics was confirmed in the cross-sectional TEM study.

Spectroscopic ellipsometry was used to track the evolution of film thickness, optical properties and film density as a function of the processing conditions. The decrease in thickness as a function of drying temperature is consistent with the weight loss observed in TGA results. The refractive index of the films increases as the RTA temperature increases, suggesting further crystallization of barium titanate and organic decomposition. The furnace annealed (1000^oC) film show a refractive index comparable to that of a 95% dense ceramic.

Investigation of NiO in barium titanate films on Ni foils was attempted by spectroscopic ellipsometry. To facilitate studies of the dielectric/electrode interface, the optical properties of thermally grown NiO on a Ni foil were extracted. It was found that

the Ni foil begins to oxidize at 300^{o}C in air. The real part of the high frequency dielectric constant of NiO is similar to that of barium titanate, which complicated modeling of NiO in barium titanate films on Ni foil.

6.2 Future work

6.2.1 Organic removal and decomposition

As shown in this work, organic removal and decomposition become a very signifcant issue in processing chemical solution deposited films in low oxygen partial pressures. The delay in decomposition results in remaining of organics especially C in the films. Different approaches are suggested to minimize the organics and C in the films in future work.

One approach for this would be to insure that the concentration of organics in the film is reduced as much as possible in air at temperature up to 500^{o}C without Ni oxidation. It has been reported by Losego **[1]** that if more reducing conditions are employed during the pyrolysis of the first layer of PZT films on copper, then the perovskite layer acts as a kinetic barrier to future oxidation. Thus, it was possible to use more aggressive pyrolysis conditions when subsequent layers were added. It would be useful to find out if a comparable procedure can be employed for $BaTiO_3$ on Ni. This would require that the minimum thickness of barium titanate film that can protect against subsequent Ni oxidation at low temperatures should be determined.

Alternatively, investigations could be performed using organic removal and RTA steps in an air ambient, accepting the existence of Ni oxidation. The NiO could subsequently be removed in reducing atmospheres at high temperature. It will be

important in this case to minimize the amount of oxidation of the Ni because the volume change on reduction from NiO to Ni.

Another related issue is the intermediate phase. $BaCO_3$ and a small amount of oxycarbonate were found as intermediate phases in crystallization of barium titanate powders and films, respectively. In this experiment, the powders were calcined in air while the films were RTA annealed in N_2 flow. The origin of the difference in crystallization pathways should be explored. Thus, the processing might be adjusted to avoid or minimize the intermediate phase, especially in low pO_2. This, in turn would, enable a decrease in the crystallization temperature of the barium titanate films.

6.2.2 Interface of barium titanate film and Ni foil

This work showed the presence of C in the barium titanate film as well as the existence of a Ni-Ba alloy interface between barium titanate film and Ni foil. However, it is not clear whether, in thin films, the occurrence of the alloy layer (or reduced Ti) are associated with this local C or not. This point should be clarified. Towards this end, it may be useful to determine the oxygen nonstoichiometry and C in a crystallized film (without re-oxidation) to compare to the current results. In addition, the composition of the alloy phase should be measured quantitatively. This may enable the height of the Schottky barrier between the electrode and the film to be estimated. A lower barrier height is expected to be problematic for the insulation resistance of the thin film capacitors. Finally, it is interesting to quantitatively determine whether there is a composition change or gradient in the barium titanate near the interface due to the loss of some Ba to form the alloy phase.

6.2.3 Spectroscopic ellipsometry for NiO on Ni foil investigation

This work has shown that the Ni foil surface roughness and the similarity of optical properties between NiO and barium titanate complicated the spectroscopic ellipsometry study. In particular, the changes in delta and psi (especially near 0 or 180 °) due to surface roughness and to an interfacial layer are in many ways comparable. The differences between them, however, were masked by the degraded accuracy of these values in a rotating analyzer ellipsometry measurement. To improve the sensitivity of ellipsometry for this characterization, a much smoother Ni foil is required for a rotating analyzer instrument. Alternatively, it may be possible to remove the errors in Δ by using a rotating compensator ellipsometer.

References

[1] M. Losego. "The Chemical Solution Deposition of Lead Zirconate Titanate (PZT) Thin Films Directly on Copper Surfaces," M.S. Thesis, North Carolina State University, 2005.

VITA

Tanawadee Dechakupt was born in 1976 in Yala, Thailand. She received her B. Sc. degree in Materials Science at Chulalongkorn University, Bangkok, Thailand in 1997. After working in Minebea Thai Co. Ltd., Ayutthaya, Thailand, she continued her graduate study and obtained a M. Sc. in Materials Science at Chulalongkorn University in 2000. She is now working toward her Ph.D. degree in Materials Science and Engineering at the Pennsylvania State University.